

The University of Maine

DigitalCommons@UMaine

---

Electronic Theses and Dissertations

Fogler Library

---

Spring 5-6-2022

## Development and Characterization of Bound Metal Deposition Including Laser Ablation

Alexander J. Watson

University of Maine, [alexander.watson@maine.edu](mailto:alexander.watson@maine.edu)

Follow this and additional works at: <https://digitalcommons.library.umaine.edu/etd>



Part of the [Mechanical Engineering Commons](#), and the [Metallurgy Commons](#)

---

### Recommended Citation

Watson, Alexander J., "Development and Characterization of Bound Metal Deposition Including Laser Ablation" (2022). *Electronic Theses and Dissertations*. 3576.

<https://digitalcommons.library.umaine.edu/etd/3576>

This Open-Access Thesis is brought to you for free and open access by DigitalCommons@UMaine. It has been accepted for inclusion in Electronic Theses and Dissertations by an authorized administrator of DigitalCommons@UMaine. For more information, please contact [um.library.technical.services@maine.edu](mailto:um.library.technical.services@maine.edu).

**DEVELOPMENT AND CHARACTERIZATION OF BOUND METAL DEPOSITION INCLUDING LASER  
ABLATION**

By

Alexander Watson

B.S. University of Maine, 2020

A THESIS

Submitted in Partial Fulfillment of the

Requirements for the Degree of

Master of Science

(in Mechanical Engineering)

The Graduate School

The University of Maine

May 2022

Advisory Committee:

Dr. Brett Ellis, Associate Professor, Mechanical Engineering Technology, Advisor

Dr. Masoud Rais-Rohani, Richard C. Hill Professor and Chair, Mechanical Engineering, Advisor

Dr. Bashir Khoda, Assistant Professor, Mechanical Engineering

# **DEVELOPMENT AND CHARACTERIZATION OF BOUND METAL DEPOSITION INCLUDING LASER ABLATION**

By Alexander Watson

Thesis Advisors: Dr. Brett Ellis & Dr. Masoud Rais-Rohani

An Abstract of the Thesis Presented  
in Partial Fulfillment of the Requirements for the  
Degree of Master of Science  
(in Mechanical Engineering)  
May 2022

Bound Metal Deposition (BMD) is a novel metal additive manufacturing technology in which a metal powder-binder composite paste is layer-wise extruded to form a part, which is then debound and sintered into a solid metal part. Although promising, BMD suffers from shrinkage-induced warpage and an inability to produce fine length scale features. This research addresses these problems by: (1) characterizing warpage of planar parts, and (2) developing a novel laser ablated process to create fine length scale features. First, a 12-factor resolution IV fractional-factorial design of experiments (DOE) was conducted to determine the warpage of planar parts as a function of part geometry, infill density, and process conditions. Results indicate part height and length were most influential for as-sintered warpage. Second, a novel laser ablation BMD (laBMD) process was developed and characterized via a full-factorial DOE. Factors included pattern geometry and process parameters. Results show the as-sintered ablation depth, ablated surface roughness, and angle between ablated and non-ablated regions were tailorable via processing parameters. The results from the laBMD DOE were applied to the design of a microfluidics mold for roll-to-roll forming.

## **DEDICATION**

I would like to thank my friends and family, especially my parents, for their support and encouragement to strive for my best.

Special thanks to my advisors Dr. Brett Ellis and Dr. Masoud Rais-Rohani, and AMC Director John Belding, whose combined wisdom was imperative to the success of this research.

## **ACKNOWLEDGEMENTS**

Financial support was provided by Maine Technology Institute (MTI) grant #CIP209, the University of Maine's Advanced Manufacturing Center (AMC), and the University of Maine's Center for Additive Manufacturing of Metals (CAMM).

## TABLE OF CONTENTS

DEDICATION .....	iii
ACKNOWLEDGEMENTS .....	iv
LIST OF TABLES .....	ix
LIST OF FIGURES .....	x
LIST OF EQUATIONS .....	xvii
LIST OF NOMENCLATURE .....	xviii
LIST OF ABBREVIATIONS .....	xix
CHAPTER 1: INTRODUCTION .....	1
1.1: Additive Metal Manufacturing .....	1
1.1.1: Direct Additive Manufacturing of Metals .....	3
1.1.2: Sinter-Based Additive Manufacturing of Metals .....	4
1.1.2.1: Material Extrusion .....	4
1.1.2.1.1: Bound Metal Deposition .....	4
1.2: BMD Process .....	8
1.2.1: Printing .....	8
1.2.1.1: Interface Material .....	11
1.2.2: Debinding .....	12
1.2.2.1: Solvent Debinding .....	12
1.2.2.2: Thermal Debinding .....	13
1.2.3: Sintering .....	13
1.2.3.1 Sintering Mechanics .....	15
1.3: Research Motivations .....	19
1.3.1: Previous Works .....	22
1.3.2: Challenges and Considerations in AMM .....	25
1.3.2.1: Geometric Conformance .....	25
1.3.2.2: Production Volume and Time .....	26
1.4: Thesis Scope .....	26
CHAPTER 2: WARPAGE STUDY .....	28
2.1: Introduction .....	28
2.2: Conceptualizing the DOE .....	29
2.3: Printing and Scanning Procedure .....	31

2.3.1: Part Design in SolidWorks .....	32
2.3.2: Part Design in Fabricate .....	33
2.3.3: Other Factors .....	35
2.4: Part Processing for Warpage DOE.....	37
2.5: Qualitative Warpage Results.....	38
2.6: Warpage DOE Analysis and Results .....	39
2.6.1: Regression Equations.....	39
2.6.1.1: Green, On-Sheet Warpage Regression Equation in Coded Units .....	40
2.6.1.2: Green, Off-Sheet Warpage Regression Equation in Coded Units.....	40
2.6.1.3: Brown Warpage Regression Equation in Coded Units.....	41
2.6.1.4: Sintered Warpage Regression Equation in Uncoded Units .....	41
2.6.2: Pareto Charts .....	41
2.6.3: Main Effects Plots .....	44
2.7: Warpage DOE Discussion .....	47
CHAPTER 3: DILATOMETRY .....	49
3.1: Preparation of Dilatometry Specimens.....	49
3.2: Dilatometry Specimen Micrographs .....	52
3.3: Dilatometry Testing.....	53
3.4: Dilatometry Results.....	55
CHAPTER 4: LASER ABLATED BOUND METAL DEPOSITION STUDY .....	58
4.1: Introduction .....	58
4.1.1: Laser Ablation .....	58
4.1.2: Research Objective .....	59
4.2: Methods.....	59
4.2.1: Manufacturing .....	59
4.2.2: Design of Experiments .....	64
4.2.3: Measurement System.....	66
4.2.3.1: Average Ablation Depth, D .....	66
4.2.3.2: Surface Roughness of Ablated Regions, Sq.....	67
4.2.3.3: Angle Between Ablated and Non-Ablated Surfaces, $\theta$ .....	68
4.2.3.4: Ablated Width, W .....	70
4.3: Results.....	70

4.3.1: Ablated Depth, $D$ .....	72
4.3.2: Surface Roughness, $S_q$ .....	74
4.3.3: Average Angle Between Ablated and Non-Ablated Surfaces, $\theta$ .....	75
4.3.4: Ablated Width at Bottom of Rectangle, $W_b$ .....	76
4.3.5: $D$ – $S_q$ – $\theta$ Response Space .....	78
4.4: Discussion.....	79
CHAPTER 5: MICROFLUIDICS APPLICATION OF LASER ABLATED BMD .....	81
5.1: Microfluidics Mold Design Parameters.....	83
5.2: Direct Laser Ablation of the Channel Pattern .....	85
5.3: Study A, Thick Printed Parts.....	86
5.4: Study B, Thin Printed Parts .....	91
5.5: Roll-to-Roll Casting Tests with BMD Molds .....	95
5.6: Measurement of Profiles .....	98
5.7: Results.....	99
5.7.1: Color Deviation Maps .....	99
5.7.2: A001 Profiles .....	102
5.7.3: A003 Profiles .....	103
5.7.4: A004 Profiles .....	105
5.7.5: Comparing Profiles.....	106
5.8: Discussion and Conclusions .....	108
5.8.1: Pattern Features .....	108
5.8.2: Surface Grinding Considerations .....	108
CHAPTER 6: SUMMARY AND CONCLUSIONS .....	110
6.1: Warpage Summary and Conclusions .....	110
6.2: Laser Ablated BMD Summary and Conclusions .....	111
BIBLIOGRAPHY .....	113
APPENDIX A: PRINT FOOTPRINTS FOR WARPAGE DOE .....	119
APPENDIX B: FABRICATE AND STUDIO SYSTEM UPDATES.....	120
APPENDIX C: WARPAGE DOE GROUPING .....	121
APPENDIX D: WARPAGE DOE DATA .....	122
APPENDIX E: WARPAGE DOE ANOVA TABLES.....	124
APPENDIX F: FACTOR LEVELS & RESULTS DATA FOR LABMD STUDY.....	127



APPENDIX G: WARPAGE EXPERIMENT INFORMATION ..... 128  
BIOGRAPHY OF THE AUTHOR..... 130

## LIST OF TABLES

Table 1. List of available materials for BMD .....	7
Table 2. Results from Gabilondo et al. [44] .....	23
Table 3. Material Properties of 17-4PH found in Watson et al. [23] .....	24
Table 4. Dimensions of each possible part geometry from the combinations of the rectangular prism major dimensions .....	33
Table 5. Laser ablation factors and levels.....	64
Table 6. Laser ablation treatment number, processing parameters, and as-sintered depth, roughness, and ablation angles. ....	72
Table 7. Profile angles for A001, A003, and A004 and treatment 1 .....	107
Table 8. Warpage DOE Factors and Responses .....	122
Table 9. ANOVA table for On-sheet Warpage.....	124
Table 10. ANOVA Table for Off-sheet Warpage.....	125
Table 11. ANOVA for Brown Warpage.....	125
Table 12. ANOVA for Sintered Warpage.....	126
Table 13. Factor levels and response quantities for laBMD study .....	127
Table 14. Table of factors in warpage DOE.....	128

## LIST OF FIGURES

Figure 1. GE Aviation's AMM fuel nozzle, and its placement on a cross-section of the LEAP engine [3], [4].....	1
Figure 2. Schematic showing use distribution of AMM technologies via AMPOWER [5] .....	2
Figure 3. Maturity Index for Metal AM via AMPOWER [6] .....	3
Figure 4. Two cubes sliced for BMD. Left cube sliced with 100% infill, right cube sliced with 44.8% infill. ....	6
Figure 5. Overview of the BMD process, adapted from [23] .....	8
Figure 6. A 17-4PH media rod (top) and an interface media rod (bottom) used in BMD. ....	9
Figure 7. Print bed being loaded; (a) print bed without a print sheet, (b) with a sheet partially slid on, (c) with sheet fully slid on, and (d) with front latch in place .....	10
Figure 8. Green state part after peeling from print sheet .....	11
Figure 9. (a) A green-state part showing the white interface material (orange arrows). (b) The sintered state shows the final part after sintering and removal of support material. ....	11
Figure 10. Exploded view of the graphite retort used in the sintering process .....	14
Figure 11. Furnace tray with 4 setter plates .....	14
Figure 12. Gas flow in the graphite retort .....	15
Figure 13. visual representation of R1 & R2 for Laplace equation .....	16
Figure 14. Neck formation when two particles come in contact; from German [36] .....	17
Figure 15. Generic furnace temperature plot cartoon (adapted from Desktop Metal [37]).....	18
Figure 16. Densification as a function of particle size and temperature [36] .....	19
Figure 17. Minimum feature sizes for standard and 250 $\mu\text{m}$ printheads from Desktop Metal Design Guide [43] .....	21

Figure 18. Build time for 50 × 50 × 50 mm <sup>3</sup> cube for Standard+ and Ultra Fine+ printing profiles .....	21
Figure 19. Horizontal and vertical part setups [44] .....	22
Figure 20. XYZ oriented tensile bar used in Watson et al [23].....	23
Figure 21. Mechanisms accounted for by DM Live Sinter™ to adjust for non-isotropic shrinkages during sintering of binder-jetted parts [48].....	25
Figure 22. Live Sinter™ predictive capabilities for sinter-based AMM [48].....	25
Figure 23. An example part that is flat and long that experiences warpage during BMD manufacturing.....	28
Figure 24. Available factorial designs dialog box in Minitab [52] .....	30
Figure 25. Create Factorial Design: Designs dialog box in Minitab [52] .....	31
Figure 26. Visual overview of methods employed for the warpage study .....	32
Figure 27. Different printing orientations shown in Fabricate .....	34
Figure 28. X-oriented warpage specimen .....	34
Figure 29. Y-oriented warpage specimen .....	35
Figure 30. Cartoon (left) showing 2D slice of as-printed cross-section and a representative part (right) the top surface milled away to show infill.....	35
Figure 31. Installation of a print sheet onto the vacuum platform .....	36
Figure 32. Layout of two warpage specimens on furnace tray.....	37
Figure 33. Layout of parts on setters in a retort layer .....	38
Figure 34. Treatment 1 and treatment 13 warpage comparison .....	39
Figure 35. Pareto chart showing warpage of the part on the sheet.....	43
Figure 36. Pareto chart showing warpage of the part after removal from the print sheet .....	43
Figure 37. Pareto chart showing warpage of the part in the brown state, after removal from the solvent debinding.....	44

Figure 38. Pareto chart showing warpage of the sintered part, after removal from the furnace .....	44
Figure 39. Main effects plot showing first level effects of each factor on the warpage on-sheet.....	45
Figure 40. Main effects plot showing first level effects of each factor on the warpage off-sheet.....	46
Figure 41. Main effects plot showing first level effects of each factor on the warpage after debinding. ....	46
Figure 42. Main effects plot showing first level effects of each factor on the warpage after sintering. ....	47
Figure 43. Print jobs that were halted during printing that allowed for an abnormally high cooling rate.....	48
Figure 44. Geometry for XYZ dilatometry specimen showing major dimensions .....	50
Figure 45. Green-state X-, Y-, and Z-oriented dilatometry specimens Printing layout for dilatometry specimens, colored arrows denote direction of length orientation.....	50
Figure 46. Cressington Sputter Coater 108 auto during coating process .....	51
Figure 47. SEM machines: Nvision 40 (left) and AMRAY 1820 (right). ....	52
Figure 48. SEM image of a brown state ceramic interface material (larger, more spherical particles) and 17-4PH stainless steel material (smaller, more irregular particles).....	52
Figure 49. Temperature profiles used in HJEco dilatometry test .....	54
Figure 50. Dilatometry setup .....	55
Figure 51. Comparison of dilatometry results for X, Y, and Z printed specimens .....	56
Figure 52. Dilatometry curves of HJEco test compared to Kwon et al. [62]. ....	57
Figure 53. Manufacturing workflow showing BMD process steps (gray backgrounds) and the introduced laser ablation step (red background). ....	60
Figure 54. Composite ablation pattern for Specimen 1 showing the eight ablation patterns for Treatments 1-8. Ablation patterns for Specimens 2, 3, and 4 are similar except that the ablated	

numbers at the top of the pattern are 9 through 16, 17 through 24, and 25 through 32, respectively. Each composite ablation pattern has overall dimensions of 59.54 mm × 59.54 mm. .... 62

Figure 55. Schematic showing ablation pattern relative to the laser rastering direction for (a) perpendicular and (b) parallel orientations. .... 63

Figure 56. Optical image showing the top view of the ablated rectangle (top) and a side view showing depth along the ablated rectangle’s major axis (bottom) for Treatment 1. The yellow line indicates the measured non-ablated height, and the cyan line indicates the measured ablated height. .... 67

Figure 57. Positioning of the 4.0-mm-diameter surface roughness measurement region (red circle) within the 5.0-mm-diameter circular ablated region for Treatment 10. .... 68

Figure 58. Cross section profile of the rectangular ablated region for Treatment 1, averaged over an 11.00-mm region in the channel middle for treatment 1 in the sintered state. The gray-colored region was added to indicate non-ablated material; hence, the gray coloring fails to show actual non-ablated microstructure, such as intra- and inter-bead porosity. .... 69

Figure 59. As-sintered Specimens 1 through 4 showing Treatments 1 through 32. .... 70

Figure 60. Optical (top) and topological (bottom) images showing a 20-mm-long region of channels for Treatments 1-8 (*i.e.*, Specimen 1). The approximate location of the imaged region is indicated by the blue-colored rectangle overlaid on Specimen 1 (cf. top right corner). .... 71

Figure 61. Regressed average as-sintered depth as a function of measured average as-sintered depth. Perfect correlation is indicated by the dotted line. The dashed line above and below the dotted line indicate +50 and -50 offsets, respectively. .... 74

Figure 62. Regressed as-sintered roughness as a function of measured as-sintered roughness. Perfect correlation is indicated by the dotted line. The dashed line above and below the dotted line indicate +12 and -12 offsets, respectively. .... 75

Figure 63. Regressed as-sintered angle as a function of measured as-sintered angle. Perfect correlation is indicated by the dotted line. The dashed line above and below the dotted line indicate +15 and -15 offsets, respectively. .... 76

Figure 64. Regressed as-sintered width as a function of measured as-sintered width. Perfect correlation is indicated by the dotted line. The dashed line above and below the dotted line indicate +150 and -150  $\mu\text{m}$  offsets, respectively. .... 77

Figure 65.  $D-S_q-\theta$  response space showing the (a)  $\theta-S_q$ , (b)  $\theta-D$ , (c) and  $S_q-D$  planes. Treatment number is indicated via a number adjacent to each point. .... 78

Figure 66. Major processing steps in a roll-to-roll forming process utilizing a polymer mold (Boutiette et al. [79]) ..... 81

Figure 67. Half of the mold for the first design idea..... 82

Figure 68. Schematic showing stamp forming process, with stamp parts in grey and the shim stock in blue, starting with the flat shim stock (a), then pressure is applied to the stamp halves, deforming the shim material (b), the stamp pressure is relieved (c), and the part is deformed (d)..... 83

Figure 69. A sketch of the microfluidics pattern (gray with black outline) and dimensions (blue) in mm of the designed geometry (sintered geometry). .... 84

Figure 70. Desired microfluidics mold ..... 85

Figure 71. Fabricate rendering of Study A blank..... 86

Figure 72. Angle  $\theta$  – surface roughness  $S_q$  response space highlighting  $\theta-S_q$  response for Treatment 1. .... 87

Figure 73. Study A laser pattern dimensions, all length units are in mm ..... 87

Figure 74. Photo of A003 On surface grinding machine ..... 88

Figure 75. side view of A003 after surface grinding ..... 89

Figure 76. Deviation from flatness of A003 after surface grinding..... 89

Figure 77. Vernier micrometers with a cone tip placed on the ablated surface (shown) and a flat anvil on the non-ablated surface (not shown) measuring the thickness of A003.....	90
Figure 78. Thickness measurements of A003 using dial micrometers, units in inches .....	90
Figure 79. Fabricate rendering of Study B part.....	91
Figure 80. Ablation Pattern for B001, units of mm.....	92
Figure 81. B001 as-sintered .....	93
Figure 82. Thickness of B001 measured using dial micrometers, units of inches. ....	93
Figure 83. Deviation from flatness of ablated B001 as-sintered .....	94
Figure 84. Deviation from flatness of unablated B002 as-sintered .....	95
Figure 85. A003 on the left, deformed after being mounted on the roller, and on the right, mounted on the roller.....	96
Figure 86. Close-up photos taken after mold use showing stuck coating at the top region of the pattern, while lower down, the pattern was free of stuck coating .....	96
Figure 87. Device produced from roll-to-roll casting of A003 .....	97
Figure 88. film produced from roll-to-roll casting of B001 .....	97
Figure 89. Two different profile measurement regions shown on specimen A001 .....	98
Figure 90. Regions of profile extractions for parts from study A.....	99
Figure 91. A001 color deviation of the ablated region after sintering .....	100
Figure 92. A002 color deviation of the ablated region after sintering .....	101
Figure 93. A003 color deviation of the ablated region after sintering .....	101
Figure 94. A004 color deviation of the ablated region after sintering .....	102
Figure 95. A001 perpendicular to gantry movement profile.....	102
Figure 96. A001 left side, parallel to gantry movement profile.....	103
Figure 97. A001 right side, parallel to gantry movement profile .....	103



Figure 98. A003 perpendicular to gantry movement profile .....	104
Figure 99. A003 left, parallel to gantry movement profile .....	104
Figure 100. A003 right, parallel to gantry movement profile .....	105
Figure 101. A004 perpendicular to gantry movement profile .....	105
Figure 102. A004 left, parallel to gantry movement profile .....	106
Figure 103. A004 right, parallel to gantry movement profile .....	106
Figure 104. Location of measurement for profiles in Table 7.....	107
Figure 105. Comparison of (a) profile from treatment 1 channel to (b) profile from A003 .....	108

## LIST OF EQUATIONS

Equation 1. The Laplace equation.....	16
Equation 2. The Arrhenius temperature relation .....	17
Equation 3. General form of regression equation for 12-factor DOE.....	40
Equation 4. green on-sheet warpage regression.....	40
Equation 5. green, off-sheet warpage regression.....	40
Equation 6. brown warpage regression.....	41
Equation 7. sintered warpage regression .....	41
Equation 8. Response surface for IaBMD study.....	65
Equation 9. Surface roughness .....	68
Equation 10. regression equation for as-sintered ablated depth.....	73
Equation 11. Regression equation for as-sintered surface roughness .....	74
Equation 12. Regression equation for angle between ablated and non-ablated surface .....	75
Equation 13. Regression equation for width at the bottom of the rectangular ablated region .....	76
Equation 14. Sintering scale factor .....	85

## LIST OF NOMENCLATURE

$c_p$	specific heat at constant pressure
$d_b$	average ablation depth at the bottom of the rectangular region
$d_c$	average ablation depth in center of the rectangular region
$d_t$	average ablation depth at the top of the rectangular region
$D$	average ablation depth
$D_h$	heat penetration depth
$e$	Euler's number
$k$	thermal conductivity
$F$	laser fluence
$F_{th}$	fluence ablation threshold
$n$	number of laser passes
$p$	laser power in percent
$r$	laser resolution in dots per inch
$s$	laser speed in %
$S_q$	surface roughness
$t$	time
$W$	Average ablated width
$\alpha$	characteristic optical penetration depth
$\kappa$	heat diffusion coefficient
$\rho$	density
$\theta$	angle between ablated and non-ablated surfaces

## LIST OF ABBREVIATIONS

AM	additive manufacturing
AMM	additive manufacturing of metals
BMD	bound metal deposition
CAMM	Center for Additive Manufacturing of Metals
dpi	dots per inch
DM	Desktop Metal
FFF	fused filament fabrication
FM	formative manufacturing
laBMD	laser ablated Bound Metal Deposition
MIM	metal injection molding
SM	subtractive manufacturing
STL	standard tessellation language

## CHAPTER 1: INTRODUCTION

Capable of producing geometrically complex structural members with reduced lead times, the additive manufacturing of metal (AMM) market is anticipated to grow by 7.2 billion USD from 2021 to 2025 [1, p. 2]. This can be attributed to the flexibility of AMM compared to other traditional types of metal manufacturing. Compared to subtractive manufacturing processes, where material is removed from a bulk material, additive manufacturing sees benefits such as reduced material waste, increased geometric freedom, lower cost, and efficiency. One example of AMM success is the GE Aviation 3D printed fuel nozzle tip (Figure 1). The AMM process powder bed fusion (PBF), was used to make this part and was able to consolidate a previously 20-part assembly into a single piece [2]. In this reduction, the weight was also reduced by about 25%. In a testament to its longevity, the additive manufacturing facility that produces these nozzles celebrated its 100,000<sup>th</sup> shipped nozzle in August 19, 2021, six years after it began production there in 2015 [1].

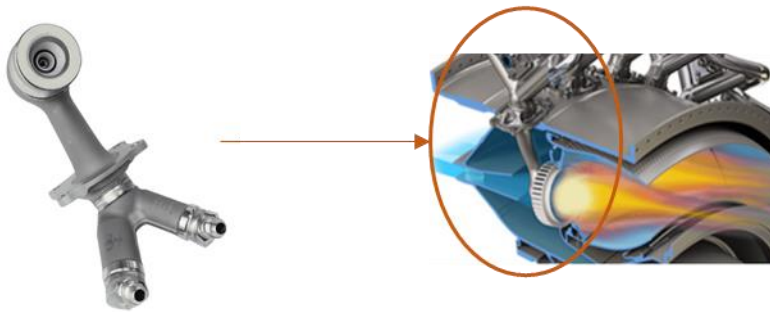


Figure 1. GE Aviation's AMM fuel nozzle, and its placement on a cross-section of the LEAP engine [3], [4]

### 1.1: Additive Metal Manufacturing

Additive metal manufacturing, or AMM, describes any process that uses 3D-printing to produce a metal part. Within AMM, there are as many as 18 identifiable processes [5] as shown in Figure 2.

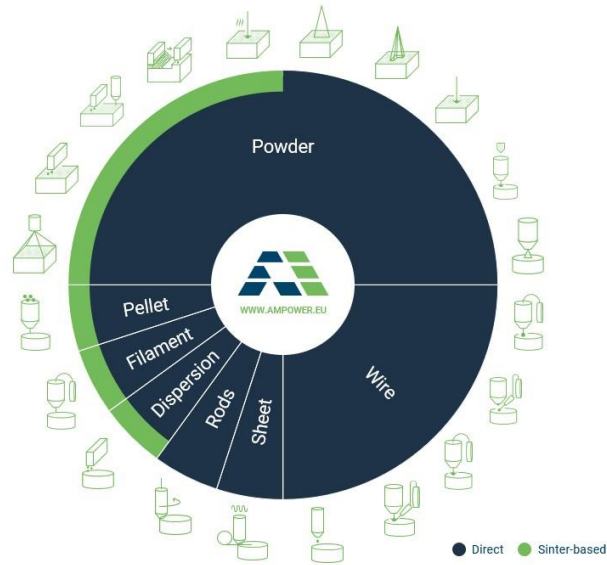


Figure 2. Schematic showing use distribution of AMM technologies via AMPOWER [5]

The Metal additive manufacturing (AM) Maturity Index (Figure 3) is a useful way to determine the industry readiness of Metal AM technologies [6]. The x-axis “Technology maturity index” corresponds to the current process capability of the process, considering things such as reliability, part performance, and machine concept. On the y-axis, the “Industrialization Index” is a metric of industry adoption that considers the knowledge base and market availability of a process.

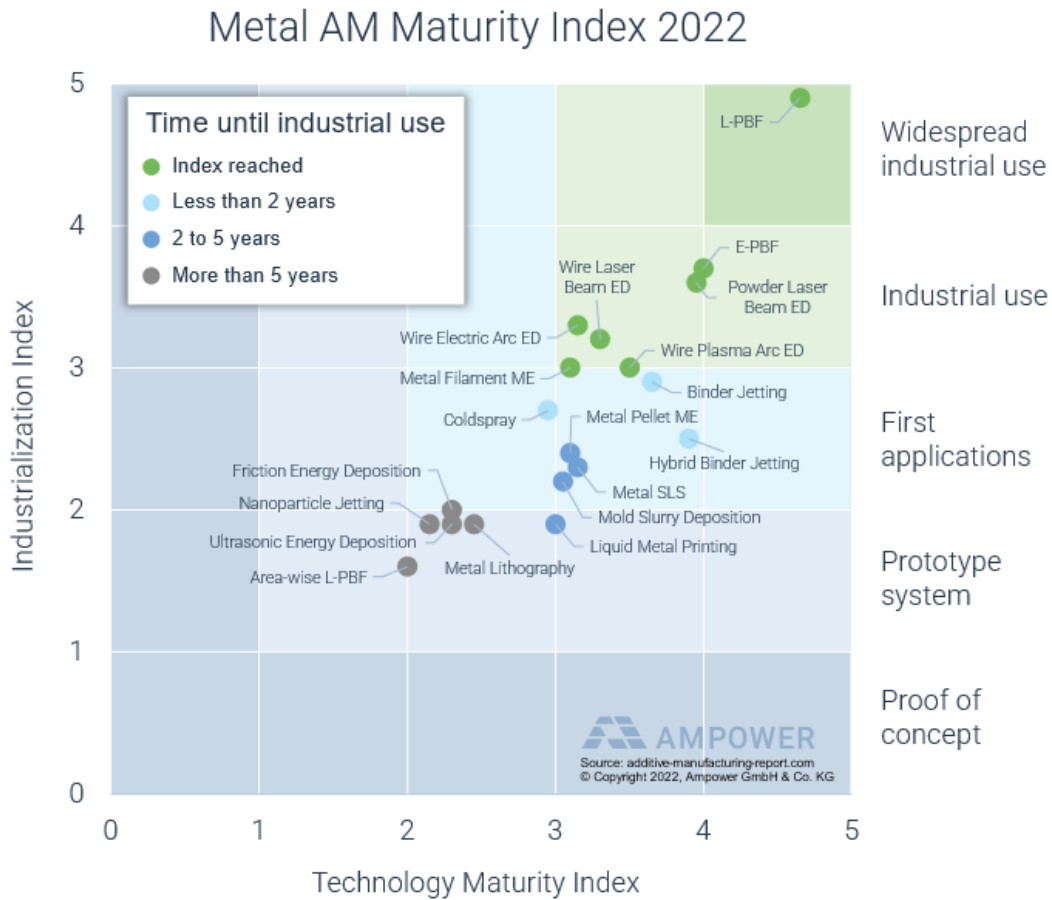


Figure 3. Maturity Index for Metal AM via AMPOWER [6]

#### 1.1.1: Direct Additive Manufacturing of Metals

Direct-type AMM includes electron beam powder bed fusion (EB-PBF), selective laser melting (SLM), laser metal deposition (LMD), coldspray, wire arc deposition, and more. These are direct processes because the finished metal part is available immediately after the additive process step. In other words, the feedstock is processed directly into a metal part in a single step, usually involving large amounts of energy to sinter together metal powder or melt the metal.

### **1.1.2: Sinter-Based Additive Manufacturing of Metals**

Sinter-based AMM includes material extrusion, binder jetting, and other lesser-known technologies.

They are characterized by their similarity to metal injection molding (MIM) because they require debinding and sintering that takes place in a separate step from the additive manufacturing step.

#### **1.1.2.1: Material Extrusion**

Material extrusion AM is one of the most widely used forms of AM today, found in various commercial industries such as biomedical, aerospace, automotive, and many more [7]. Although material extrusion is widely used, the dominant material systems in material extrusion are polymers and thermoplastics such as PLA, ABS, PETG [7]. Bound Metal Deposition (BMD) is a material extrusion process, and is the focus of this thesis.

##### **1.1.2.1.1: Bound Metal Deposition**

From Desktop Metal (DM) [8], “Bound Metal Deposition™ (BMD) is an extrusion-based metal additive manufacturing (AM) process where metal components are constructed by extrusion of a powder-filled thermoplastic media. Bound metal rods—metal powder held together by wax and polymer binder—are heated and extruded onto the build plate, shaping a part layer-by-layer. Once printed, the binder is removed via the debind process, and then sintered—causing the metal particles to densify.” BMD can be viewed as a combination of two manufacturing processes into one, additive manufacturing and metal injection molding [9]. The additive part of the manufacturing process comes when the part is printing. BMD utilizes an extrusion-based process first to build the part. This layer by layer building up of material from a nozzle that is facing a build plate is a very common 3D printing approach that is seen in the most common desktop 3D printers for consumer use. At completion of the material deposition process, the part is in what is known as the green state. The expected powder loading for metal material extrusion feedstock is 60-80%, with the remainder of the part being binder material [10]. The binder material is made of a wax-polymer mix. This wax and polymer binder has a low melting point relative to the metal



powder, so the feedstock can flow and be extruded to make parts at temperatures of 175°C for v1 materials and 165°C for v2 materials (as seen in the Fabricate slicer parameters [11]).

The similarities to metal injection molding (MIM) are many, as the process revolves around many of the same processing technologies to go from metal feedstock to a nearly fully dense metal part.

BMD is a very attractive manufacturing option for many reasons. Compared to more traditional subtractive metal manufacturing techniques (e.g., turning, drilling, milling, grinding, etc.) extrusion based additive manufacturing has increased geometric freedom. Some geometries cannot possibly be manufactured by subtractive methods but are easily achieved additively. One prominent and often used example is infill. Infill describes an internal geometry consisting of a repeating geometric shape to provide strength to a part but with purposefully designed voids that reduce material usage and decrease part weight relative to the same part without infill.

Shown below in Figure 4, a  $50 \times 50 \times 50 \text{ mm}^3$  cube was sliced with identical parameters except for the infill. The left cube was sliced with 100% infill, and the right cube was sliced with 44.8% infill (standard+ default infill parameter). This single change represents a mass savings of 41.5%, which could be significant in parts designed for applications, such as aerospace, where weight reduction could translate to significant cost-savings and performance gains [12]–[14].

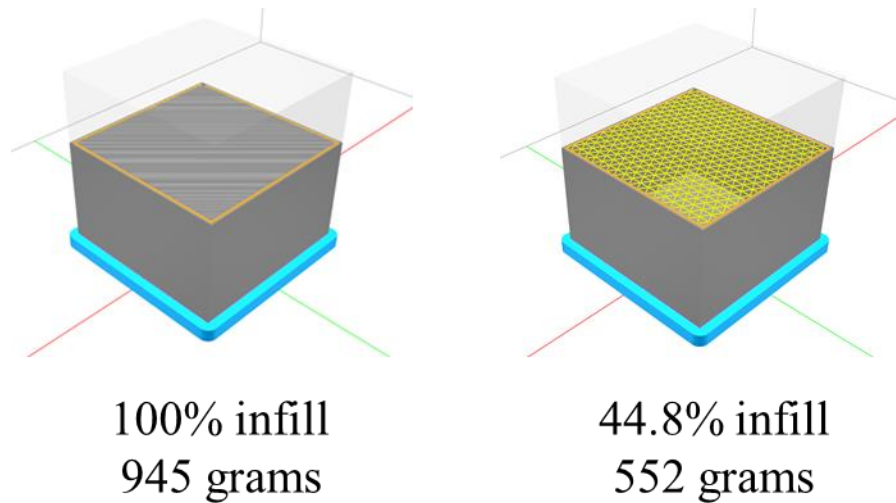


Figure 4. Two cubes sliced for BMD. Left cube sliced with 100% infill, right cube sliced with 44.8% infill.

Compared to other types of AMM, BMD uses less power, is safer, is cheaper, and has support separation built into the process so that additional machining is not required to have a finished part [8]. Some commonly used types of metal additive manufacturing include powder based AM like Directed Energy Deposition (DED) which used some form of focused thermal energy to melt and sinter metal instantly from powder [15]. DED is restricted to open-cell geometries to allow for the expulsion of unsintered metal powder, whereas BMD can produce fully enclosed lattice structure. The risks involved with AMM technologies that use loose metal powders are also greater than those encountered in BMD. Fine metal powder can pose respiratory risk to equipment operators, requiring PPE to breathe when exposed to the powder [16]–[19]. BMD avoids this risk by sintering the metal powder in a sintering furnace, which, when used properly, completely envelopes the material as it transitions from the brown state to an as-sintered metal. This is important because that point in processing is when the material poses similar respiratory risk if it were allowed to be exposed to an operator.

Compared to MIM, BMD does not require molds to be manufactured, and BMD can achieve infill while MIM is typically fully dense throughout the part. Geometric freedom is also increased in BMD, with

some geometries being impossible to demold in MIM, but are easily printed in a layer-by-layer fashion. Another design challenge that must be considered in MIM is the friction of the material during molding. This friction induces density gradients into the green-state parts that need to be accounted for during the sintering process to avoid part deformation and cracking [20]–[22]. The outer surface, or skin, of a BMD part is mostly friction free everywhere except for surfaces that contact support surfaces. Therefore, the density gradients of BMD parts are less and don't require the same design considerations as with MIM.

As of March 2022, materials that are available for the BMD process are shown in Table 1. This table shows v1 and v2 materials. The difference between v1 and v2 is the debinding step. Whereas v1 materials require solvent debinding to prepare them for the furnace step, v2 materials do not. While v2 materials eliminate the need for solvent debinding, more thermal debinding is required for v2 materials since all the debinding is occurring thermally. The v1 material also has thermal debinding, but it does not require as much thermal debinding because it first undergoes solvent debinding to remove a portion of the binder material.

Table 1. List of available materials for BMD

<b>Material Type</b>	<b>Available in v1 (requires solvent debinding)</b>	<b>Available in v2 (does not require solvent debinding)</b>
17-4PH stainless steel	Yes	Yes
316L stainless steel	Yes	Yes
4140 chromoly steel	Yes	Yes
H13 tool steel	Yes	No
Copper	Yes	No
Ti64 titanium	Yes	No
D2 tool steel	No	Yes

## 1.2: BMD Process

The BMD process for v1 materials consists of five steps: printing, solvent debinding, thermal debinding, sintering, and cooling (Figure 5). First, the part is handled digitally with CAD or an equivalent software being used to generate a part geometry. That geometry is then sent to Desktop Metal’s cloud slicing software, Fabricate™. Settings that effect printing parameters are applied in the slicer and stored in a gcode file that is sent to the printer. The printing, debinding, and sintering processes are initiated by an operator and carried out according to information generated in Fabricate. The printing, debinding, and sintering processes are discussed in greater detail in the following sections.

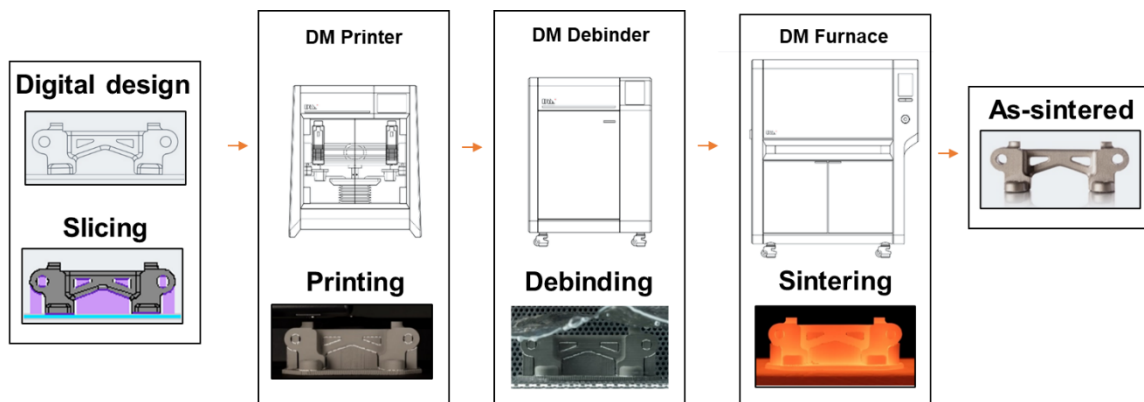


Figure 5. Overview of the BMD process, adapted from [23]

### 1.2.1: Printing

After the part is designed and sliced, it is submitted to a queue for printing. During this process step, material extrusion additive manufacturing is used to build a part layer-by-layer. The key defining feature of BMD is its use of material in rod form (see Figure 6). Other material extrusion processes may use filament or pelletized material. The Desktop Metal (DM) Knowledge Base outlines 3 major areas in which bound metal rods are superior to bound metal filament: reduction in part cracking, higher part density, and a more robust printing process [24]. Bound metal rods do not need to be compliant like

bound metal filament, so the material can be stored with a lower binder to metal powder ratio. Because of this difference, the amount of shrinkage experienced by the part is less than if it had a higher binder to metal ratio. Minimizing the part shrinkage is critical because it decreases the likelihood of part cracking and warping. Higher media density also correlates to higher final part density. If the metal particles are farther apart in the media, they must travel farther to sinter together, requiring more energy to bring the particles together, and if they fail to come together, the microporosity of the part can be increased, which is detrimental to the bulk material properties. Lastly, the extrusion process is more robust because the material is extruded by a plunger pushing the rod down a straight nozzle, which allows for greater force of the material exiting the nozzle than with a filament fed system. Filament feeding involves the use of gears to put shear force along the filament strand.

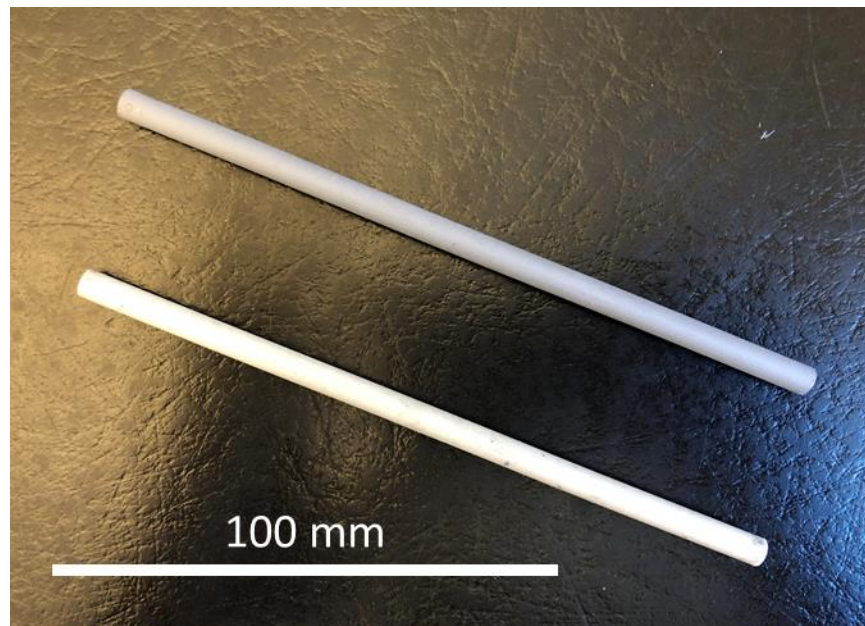


Figure 6. A 17-4PH media rod (top) and an interface media rod (bottom) used in BMD.

After printing, the part is separated from the print sheet. Print sheet dimensions are 320 mm × 221 mm × 0.4 mm with a small radius on the corners and is made from a flexible plastic material. During the

printing process, the sheet is held in place and kept from flexing by a vacuum bed, shown in Figure 7. The vacuum is held on the print sheet until the print is done, in which case the part is released by an operator or it is automatically released 12 hours after print completion.

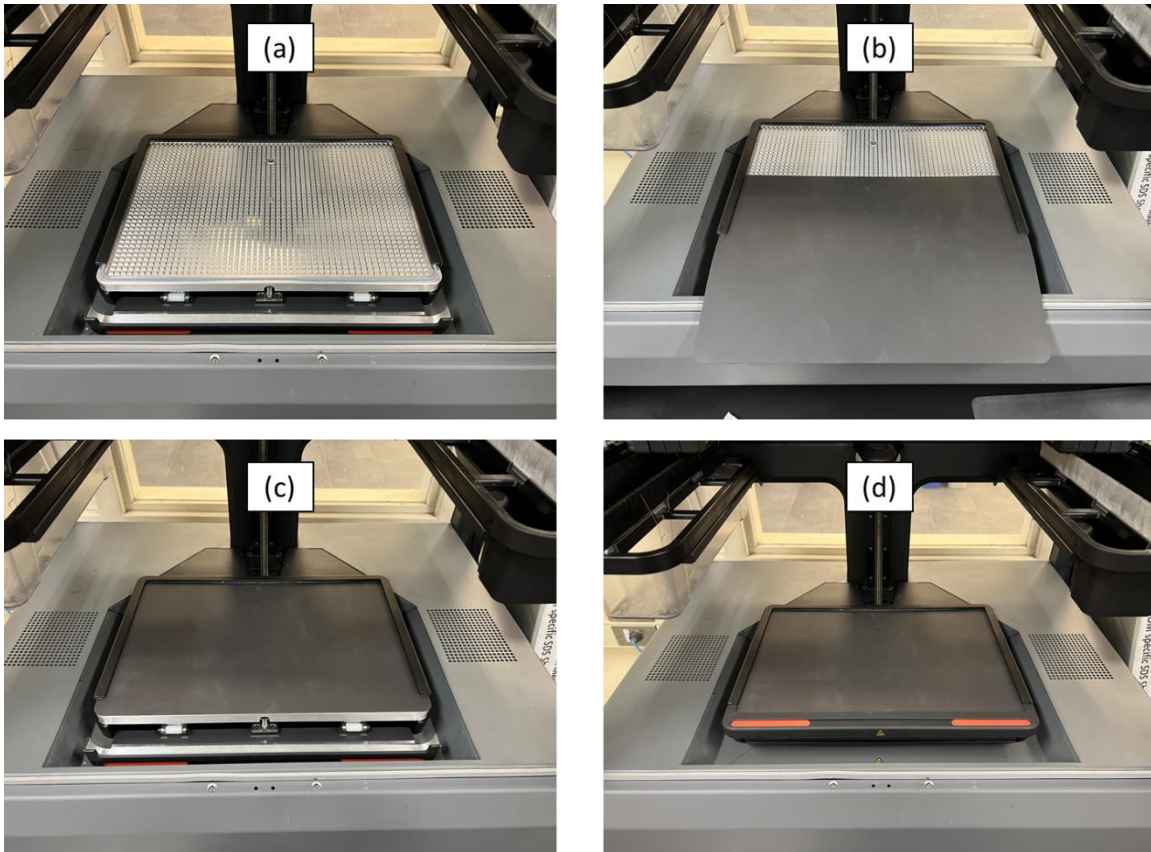


Figure 7. Print bed being loaded; (a) print bed without a print sheet, (b) with a sheet partially slid on, (c) with sheet fully slid on, and (d) with front latch in place

Peeling the part from the print sheet must be done with care to ensure that the layer lines from the material contacting the print sheet remain intact. To do this, peeling the part and sheet apart is done along the width of the print sheet to follow the direction of the first layer lines as seen in Figure 8.

Peeling perpendicular to the layer lines may cause breaking of the material.

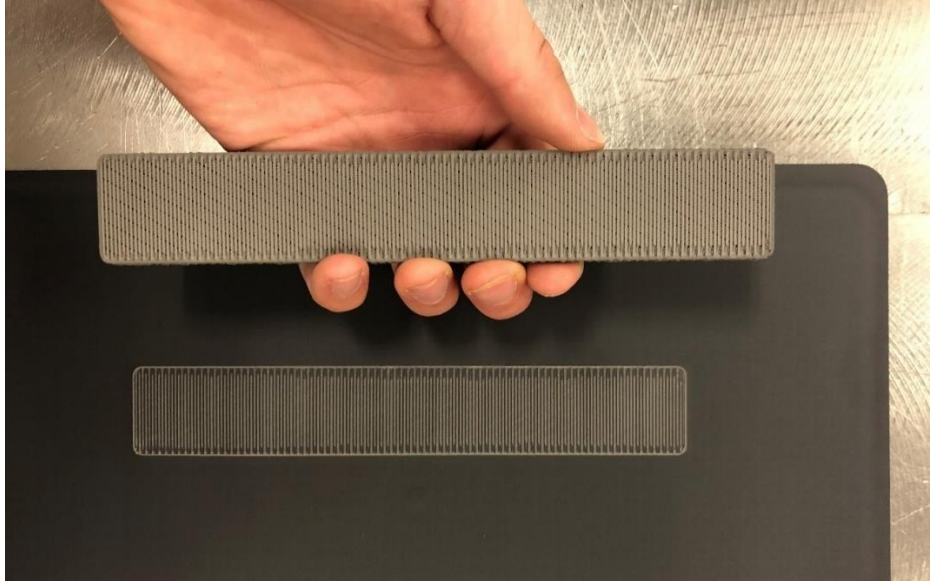


Figure 8. Green state part after peeling from print sheet

#### 1.2.1.1: Interface Material

BMD utilizes a dual-extruder printer, with one extruder for bound metal media, and the second extruder for interface media. The interface material is printed between metal regions and any supporting structures that the part may need (Figure 9). The resulting interface material structure is known as the Ceramic Release Layer™ [25]. During sintering, the ceramic interface material does not fuse to metal and prevents metal from opposite sides of the interface from sintering. Thus, the interface material prevents the part from fusing to its supports during sintering.

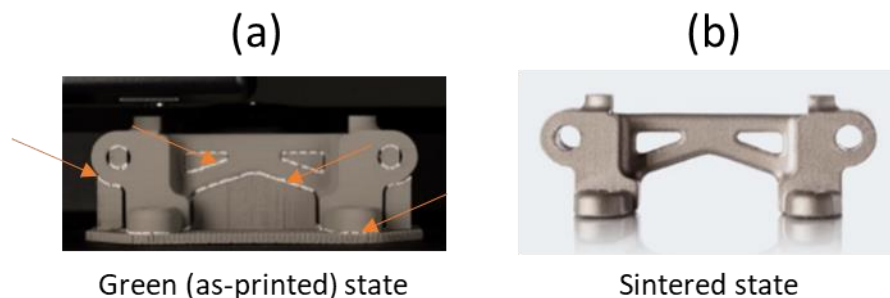


Figure 9. (a) A green-state part showing the white interface material (orange arrows). (b) The sintered state shows the final part after sintering and removal of support material.

### **1.2.2: Debinding**

After the green part is in a satisfactory state, debinding must occur. Currently, there are two different paths that debinding can take depending on the material type. The first Studio System materials, now known as v1 materials, require solvent debinding then a subsequent thermal debinding. Second generation v2 materials require only a thermal debind, eliminating the need for the solvent debinding step.

#### **1.2.2.1: Solvent Debinding**

The solvent debinding process takes place in the debinder unit. This process involves the use of a proprietary organic solvent mixture (90-98% trans-1,2-Dichloroethylene, remaining mixture proprietary chemicals) to remove one part of the two part binder system [26]. The two-part binder system, commonly used in Metal Injection Molding (MIM) processes, describes a binder made up of a mixture of a wax and polymer constituents. The wax part of the binder is removed during the solvent debinding phase. This can be deduced by the Knowledge Base revealing that the debinder waste container contains the wax part of the binder [27]. In addition to flowing the organic solvent, the debinder also heats the part to 44°C during the solvent debind phase. After the fluid is drained from the tank, the part drying phase initiates, where the temperature of the parts reach 70°C [28].

Batch processing is possible with the debinding unit, and it can hold up to 3 trays of parts, with shelves 200 mm x 300 mm that can be spaced 37 mm apart [29].

The amount of time it takes for a part to solvent debind is dependent on the part's maximum cross-sectional thickness, which is the debind fluid must travel to from the outer surface of the part to the part center [30]. Fabricate automatically determines the cross-sectional area from the part's slice and uses that to determine the debinding time required for a part. Because solvent debinding is a batch



process, the amount of time it takes for any given debind process is dependent on the part that has the longest debind time in the debinder for that job. For example, if there are three parts in a debind job with debind times of 2 hours, 10 hours, and 40 hours, the debinder will run for 40 hours and ignores the debinding times of the parts having lesser debind times. It is possible for a part to be under-debound, where an insufficient amount of the binder material was removed during the solvent debind step. Binder concentration that is higher than intended due to under-debinding can lead to part deformation and cracking.

#### **1.2.2.2: Thermal Debinding**

Thermal debinding happens during the beginning of the furnace cycle. This process evaporates the remaining binder material from the part before beginning the sintering process. The remaining binder material is the polymer constituent of the two-part wax-polymer binder.

#### **1.2.3: Sintering**

The sintering process occurs after the debinding is complete. This process is responsible for taking the powder metal part and transforming it into a mostly solid metal object. The sintering step takes place in the Studio System furnace. The parts are placed on a graphite retort that holds 6 shelves, also made of graphite (Figure 10).

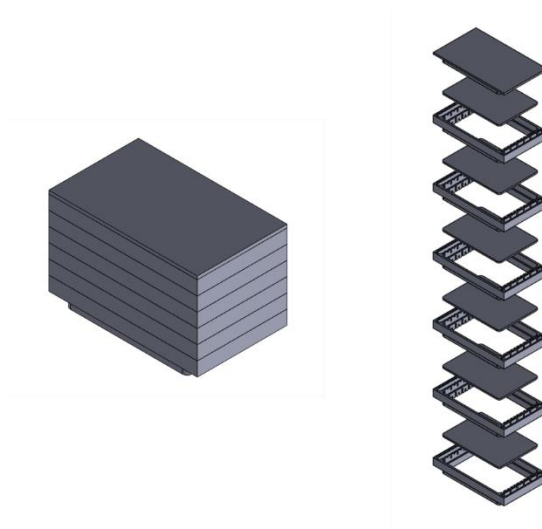


Figure 10. Exploded view of the graphite retort used in the sintering process

Within the graphite retort, four setter plates can fit on a single tray (Figure 11), so the maximum number of setter plates that the furnace can hold is 24. A setter plate is used as the surface in which BMD parts lay on during the furnace part of the process. The setter plate is  $152.4 \times 101.6 \times 1 \text{ mm}^3$  with a small radius on the corner. The setter plate material is high-purity (>99.6%) alumina which can resist high temperatures, remain non-reactive to the material placed on them, and last for many sintering cycles [31].



Figure 11. Furnace tray with 4 setter plates

Another feature of the retort is that it contains pathways that allow a flow of gas over the parts contained within the furnace (Figure 12). The gas used in processing 17-4PHv1 and 316Lv1 materials is gas number 1, which consists of 3% hydrogen with argon balance [32].



Figure 12. Gas flow in the graphite retort

In addition to the gas specifications, the sintering atmosphere is further controlled by creating a partial vacuum for the sintering process. The combination of the gas flow and the partial vacuum provide an inert environment to prevent defects from occurring in the part during the sintering process and promote the best possible density and microstructure [33].

### 1.2.3.1 Sintering Mechanics

The driving force in sintering is the reduction in surface energy due to neck formation between particles and densification of the material. Surface energy quantifies the potential bonding energy of unbalanced atoms at the surface of a bulk form of material [34]. Particle shape and size also contribute to sintering success and speed. The geometry with the least surface energy is a sphere, which minimizes surface area per mass, therefore minimizing the number of atoms in the bulk material that are unbonded. Energy is required for atomic movement, so particles are not likely to come together at low (room) temperature. The rate of bonding is dependent on the surface energy (causing a stress at the edge of the contact) and the atomic mobility (diffusion rate) of the contacting materials. [35].

The Laplace equation gives the stress  $\sigma$  associated with a curved surface as

$$\sigma = \gamma \left( \frac{1}{R_1} + \frac{1}{R_2} \right) \quad (1)$$

where  $\gamma$  is the free surface energy, and  $R_1$  and  $R_2$  are the principal radii of curvature for the surface.  $R_1$  and  $R_2$  are equal for a spherical surface.

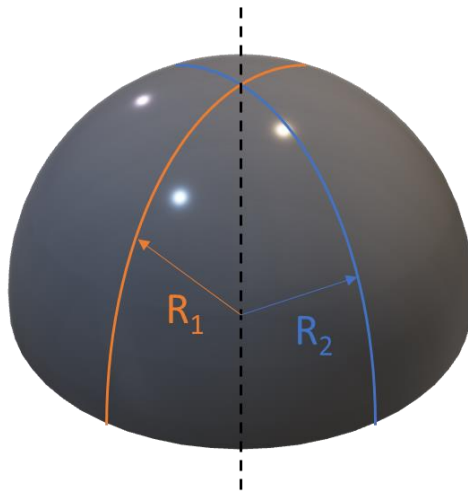


Figure 13. visual representation of  $R_1$  &  $R_2$  for Laplace equation

A flat surface ( $R_1, R_2 \rightarrow \infty$ ) is stress free. Atomic motion tends to move to reduce stress, so convex surfaces in tension and concave surfaces in compression try to minimize the potential energy between two necked particles. Minimization of the sintering stress is what drives sintering, as there is compression at an atomic level that occurs without external pressure.

When two spherical particles of diameter  $D$  come into contact, a circular neck having diameter  $X$  forms, making a peanut-like shape, shown in Figure 14. This results in tensile surface stresses on the concave surfaces and compressive stresses on the convex surfaces.

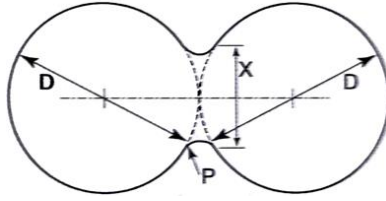


Figure 14. Neck formation when two particles come in contact; from German [36]

The likelihood of an atom moving positions within a crystal lattice follows an Arrhenius temperature relation.

$$\frac{N}{N_0} = \exp\left(-\frac{Q}{RT}\right) \quad (2)$$

where  $N/N_0$  is fraction of moving atoms,  $Q$  is the activation energy,  $R$  is the gas constant, and  $T$  is the absolute temperature. Some energy input is required to displace the atoms at the edges of the particles and promote surface energy reduction, and that energy is mostly due to holding a part at a high temperature just below melting temperature for a time period long enough to destroy the majority of the porosity (for stainless steel produced via BMD, it's about an hour).

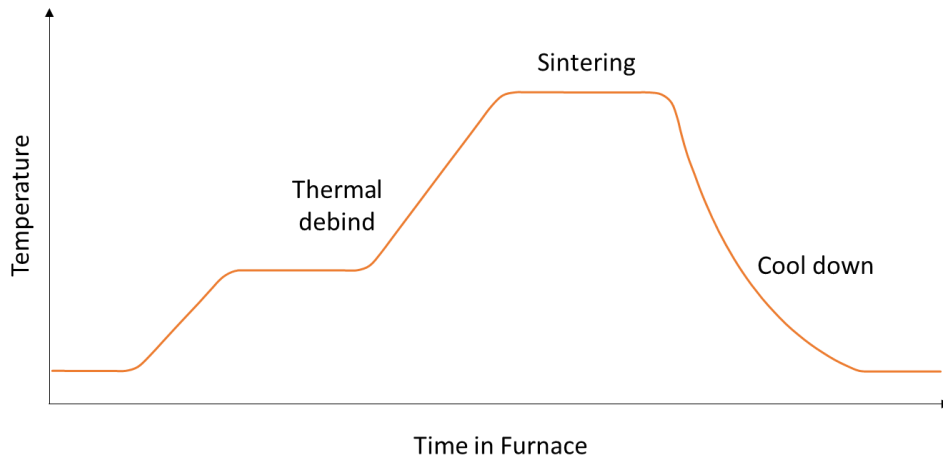


Figure 15. Generic furnace temperature plot cartoon (adapted from Desktop Metal [37])

Particle size also influences sintering, as a smaller particle has a greater stress at the surface. This translates to a lower amount of heat being required to achieve a higher density if the particle size is initially small, as shown in Figure 16 for a nickel metal injection molded compact.

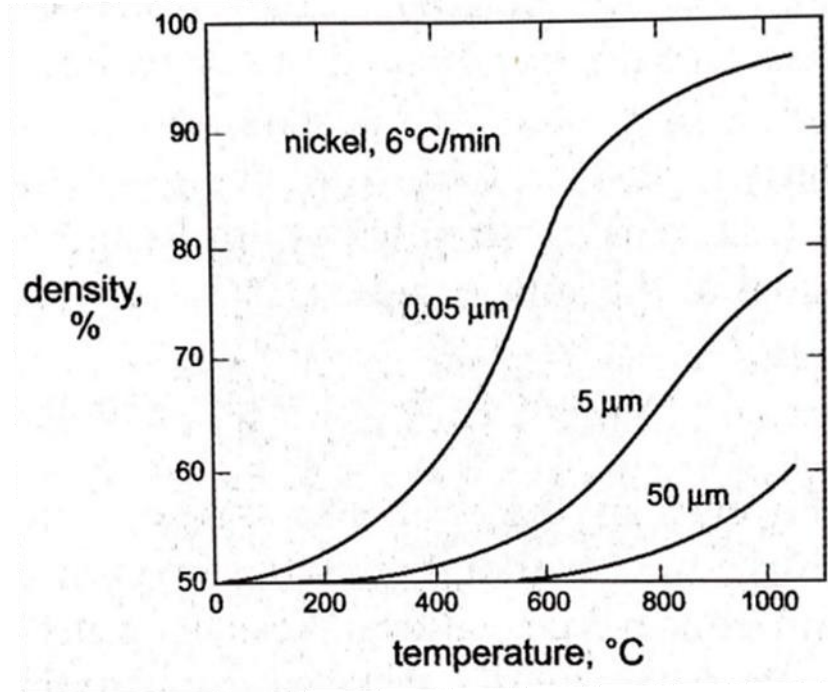


Figure 16. Densification as a function of particle size and temperature [36]

### 1.3: Research Motivations

Despite its promise, BMD requires study to achieve desired geometric and mechanical properties with consistency. The DM Studio System was launched in 2017, making the commercially available product only 5 years old [38]. Studio System v2 was launched in early 2021 [39]. This new process describes a streamlined part making process in which the solvent debinding step is skipped and the part is 100% thermally debound. This process is beneficial because an end-user can spend less time handling parts by only having to load and unload parts into the furnace.

Parts manufactured via BMD can be prone to unexpected defects, and at the time of writing, not every cause of those defects is well understood. Some defects, like some warping phenomena (after printing and debinding), slumping, and blistering are addressed in the Desktop Metal™ Knowledge Base [40]–

[42]. Further less understood defects that do not have dedicated troubleshooting pages in the Knowledge Base include cracking and warping during sintering. Flaws like those can be detrimental to the part's intended use. Geometric inaccuracy can prevent parts from fitting correctly into an assembly. Cracking can render a part completely unusable. Keeping these problems in mind, the objective of part of this research is to identify process parameters that may contribute to warpage in BMD parts.

BMD has limitations, such as production of fine-length-scale features. In general, geometries less than 0.5 mm require extra care to produce via BMD. To produce features in the 0.15 mm to 0.5 mm range, a 250  $\mu\text{m}$  printhead can be used as shown in Figure 17. The printed bead is narrower than the standard 400  $\mu\text{m}$  to accommodate finer detail. However, a significant drawback to this is the build time. Because less material can be deposited per unit time, the total build time increases depending on the part geometry. For example, Figure 18 compares the build time for two  $50 \times 50 \times 50 \text{ mm}^3$  cubes, one using a 400  $\mu\text{m}$  nozzle with a standard+ profile and the other using a 250  $\mu\text{m}$  nozzle with the Ultra Fine+ profile. The build time for the standard+ print is 23.15 hours. Compare that to the build time of the same part with the Ultra Fine+ printing profile, which takes 78.93 hours, an increase in build time of 241%. The infill density does not change between the parts, but the line distance (distance between lines in the infill pattern) does change as the line width decreases. This time increase vs print resolution tradeoff prompts a question: can the minimum resolution of a BMD part be improved without a dramatic increase in processing time?



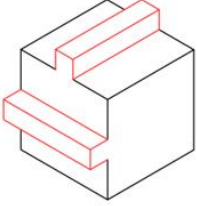
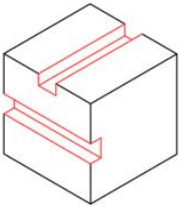
		Standard Printhead	Hi-Res Printhead
		400 $\mu\text{m}$	250 $\mu\text{m}$
	<b>Minimum Embossed Feature</b>	X/Y	W <b>0.45mm</b> 0.018in H <b>0.50mm</b> 0.020in
		Z	W <b>0.25mm</b> 0.010in H <b>0.50mm</b> 0.020in
			W <b>0.30mm</b> 0.012in H <b>0.30mm</b> 0.012in
<p>Embossed features are proud of the surface of the model. If an embossed feature is too thin, it likely will not print.</p>			
	<b>Minimum Debossed Feature</b>	X/Y	W <b>0.45mm</b> 0.018in H <b>0.50mm</b> 0.020in
		Z	W <b>0.25mm</b> 0.010in H <b>0.50mm</b> 0.020in
			W <b>0.30mm</b> 0.012in H <b>0.30mm</b> 0.012in
<p>Debossed features are typically used for surface detailing and text on the surface of the model. If a debossed feature is too thin, it risks over-extrusions that fill in the engraved feature.</p>			

Figure 17. Minimum feature sizes for standard and 250  $\mu\text{m}$  printheads from Desktop Metal Design Guide [43]

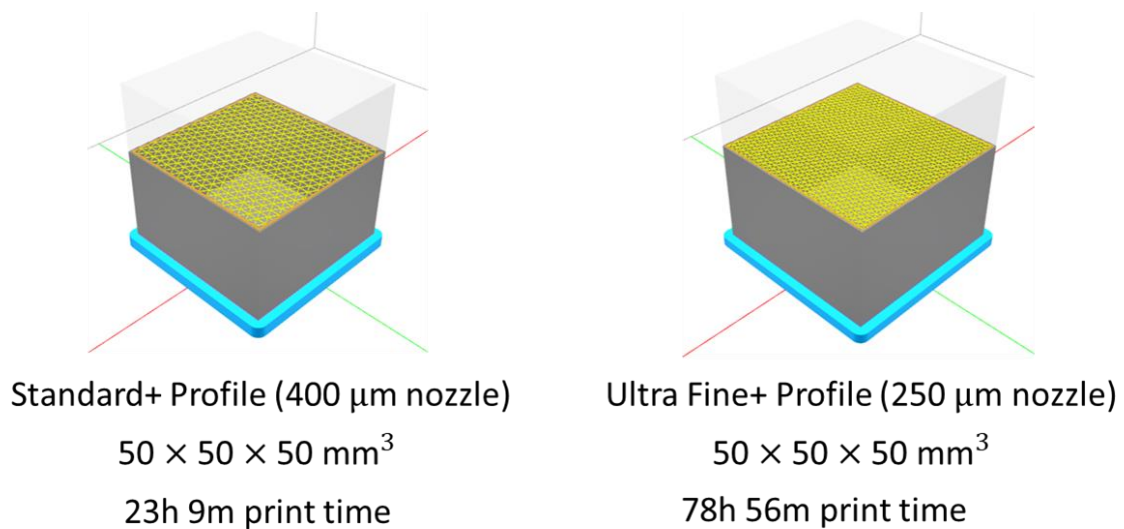


Figure 18. Build time for  $50 \times 50 \times 50 \text{ mm}^3$  cube for Standard+ and Ultra Fine+ printing profiles

### 1.3.1: Previous Works

In Gabilondo et al. [44], the tensile strength of BMD 316L stainless steel was characterized with microstructural analysis, porosity measurements, and mechanical testing of tensile and hardness properties. The build orientation, infill pattern, and chamber temperature were varied, and the results of that variation was investigated. In the five experiments, Experiments 1 and 3 had horizontal parts with a concentric pattern, Experiments 2 and 4 had vertical parts, and Experiment 5 was a horizontal specimen with lines infill pattern.

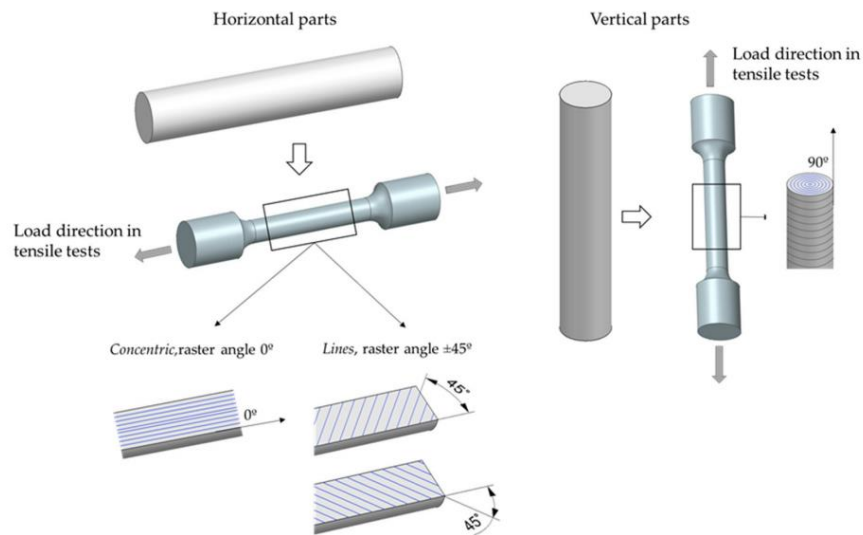


Figure 19. Horizontal and vertical part setups [44]

Gabilondo et al determined the yield strength ( $\sigma_{0.2}$ ), ultimate tensile strength (UTS), elongation at break, and area reduction in the cylindrical specimens and those results are shown in Table 2. Additionally, those results were compared to PBF and casting of 316L stainless steel. They concluded that the concentric infill pattern used negatively impacted the porosity of the part, resulting in >5% porosity, whereas the lines infill pattern had <5% porosity, which lead to an improvement to the UTS of about 20 MPa.

Table 2. Results from Gabilondo et al. [44]

Experiment/Condition	$\sigma_{0.2}$ (MPa)	UTS (MPa)	Elongation at Break (%)	Area Reduction (%)	Reference
1 (X-room-concentric)	189	530	74	41	Gabilondo et al.
2 (Z-room-concentric)	182	384	23	12	Gabilondo et al.
3 (X-50-concentric)	199	530	67	39	Gabilondo et al.
4 (Z-50-concentric)	182	363	15	12	Gabilondo et al.
5 (X-50-lines)	197	552	80	43	Gabilondo et al.
316L-PBF	X	~640-750	X	X	X
316L-casting	X	~450-485	X	X	X

In Watson et al. [23], mechanical properties of as-printed 17-4PH stainless steel BMD was measured and reported as a function of build direction (XYZ & YXZ orientations).

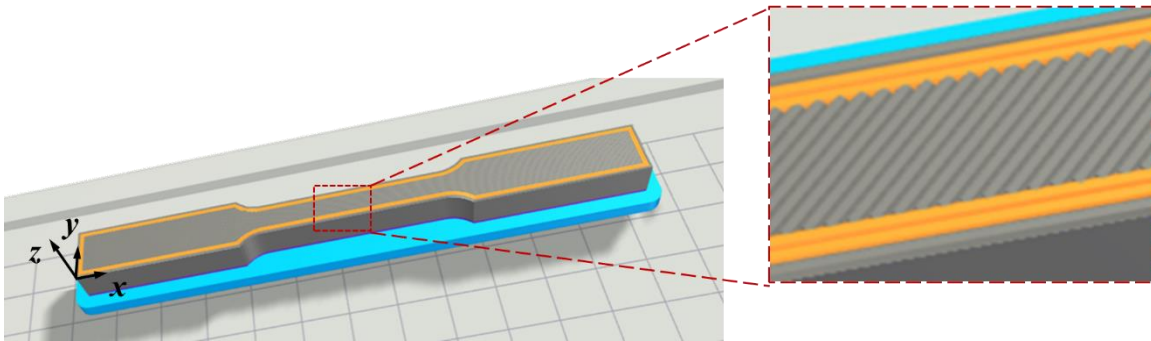


Figure 20. XYZ oriented tensile bar used in Watson et al [23]

The modulus of elasticity, yield strength, ultimate strength, and percent elongation were found following the ASTM E8/E8M-16 standard using subsize rectangular tension test specimens [45]. The results from Watson et al. [23] are reported in Table 3. In Table 3,  $E$  is Modulus of elasticity,  $S_y$  is yield

strength,  $S_u$  is ultimate strength, and % elongation is a measure of the elongation of the part during the tensile test before breaking.

Table 3. Material Properties of 17-4PH found in Watson et al. [23]

Specimens	$N$	$E$ (GPa)		$S_y$ (MPa)		$S_u$ (MPa)		% elongation	
		Mean	St. Dev.	Mean	St. Dev.	Mean	St. Dev.	Mean	St. Dev.
XYZ	8	176	12.2	604	12.5	776	2.6	7.7	0.9
YZZ	11	176	17.5	605	36.6	776	29.0	5.9	1.4
All	19	176	15.13	604	28.4	776	21.7	6.7	1.5

Desktop Metal addresses gravity- and process-induced warpages for binder-jetted AMM via the release of Live Sinter™ Software [46]–[48]. Live Sinter™ is a multi-physics engine that predicts the forces that a part will undergo during sintering, with some of the sintering mechanisms shown in Figure 21. Live Sinter™ compensates for it by generating a “negative offset” geometry, shown in Figure 22. Factors during sintering that Live Sinter™ considers include shrinkage pull, gravity drop, density warp, friction trip-up, and centroid rotation. As of September 2020, Live Sinter™ is only available for Desktop Metal’s Binder Jetting systems, and it is not yet optimized for use with other sinter-based AMM technologies such as BMD. Characterization work, like the work done in Chapter 2 for the warpage study, may be useful for creating similar software solutions to predict offset due to sintering.

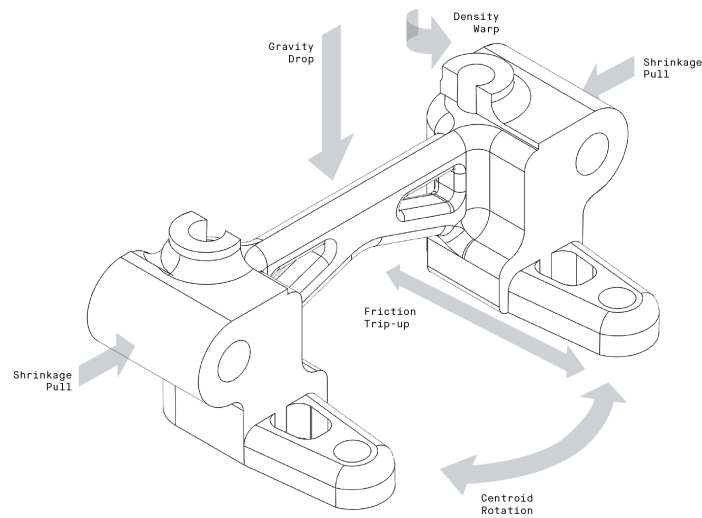


Figure 21. Mechanisms accounted for by DM Live Sinter™ to adjust for non-isotropic shrinkages during sintering of binder-jetted parts [48].

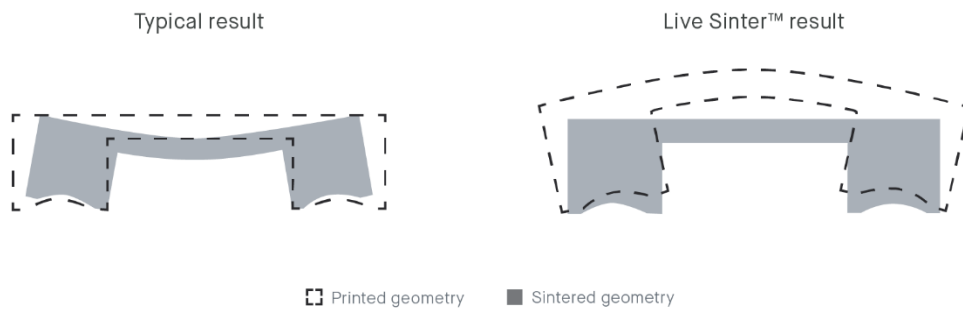


Figure 22. Live Sinter™ predictive capabilities for sinter-based AMM [48].

### 1.3.2: Challenges and Considerations in AMM

#### 1.3.2.1: Geometric Conformance

Geometric imperfections stem mostly from the sintering step of BMD, as reported previously. Live sinter was an answer to the undesired geometric deviations from the formed green-state part to the sintered metal part. Software that can model and predict the deviations during sintering are incredibly valuable,

as the total BMD processing time is typically on the order of 5 to 7 days from start of the print to the finished sintered part. If process simulations could be done prior to printing, valuable material and time would be saved.

### **1.3.2.2: Production Volume and Time**

Additive manufacturing has evolved from small batch sizes to higher volume processes [2]. The Studio system can print up to 6.5 kg of parts at a time [49] and increasing the resolution of a part usually means increasing the processing time to accommodate changes such as smaller nozzle diameter, slower deposition rates, and lower layer thickness (which increases the total number of layers). However, the studio system utilizes batch processing to process many parts at once in the debind and sinter steps. To further increase the resolution to time ratio possible with BMD, fine-length scale features could be manufactured with additional intermediate processes, such as laser ablation.

### **1.4: Thesis Scope**

Review articles highlight the importance of understanding the relationship between process, structure, and property of AMM, and it is noted as an area that requires further research [50]. Here are some of the questions that this research aims to answer to help characterize the BMD process: Which process parameters may be influential in preventing warpage of thin prismatic bar parts? Can fine-length-scale features be produced using a laser-ablation step after printing to improve manufacturing time and resolution of said features?

The thesis is structured as follows: Chapter 2 details a study that used a fractional factorial DOE to empirically determine factors that contribute to warpage of 17-4PH stainless steel parts. Next, the findings from dilatometry testing of 17-4PH are presented. Following that chapter, a study on the laser ablated BMD (laBMD) is presented, and that transitions into an overview of a laBMD application for a microfluidics device manufacturing mold. Between all these studies, progress has been made in

characterizing BMD that can be applied to modeling and predicting the behavior the process through simulation to influence better design for more efficient design and manufacturing workflows.

## CHAPTER 2: WARPAGE STUDY

### 2.1: Introduction

In BMD, warpage is a prevalent problem, particularly so with parts that are thin. Thin parts are prone to failure in the form of cracking and warping. Thin and long parts are commonly seen attempted for geometries desired to 3D print, so we wanted to study long and thin parts so that the design space investigated would match parts that were being manufactured, such as the long, thin part shown in Figure 23. For this part, the aspect ratio of the length to the thickness of the part was 40 to 1. As a result, warpage concave up along the length of the part was observed. This warpage was undesirable and prevented the part from use in its original function. This prompted the question: what process parameters can be changed to reduce the warpage of long and thin parts?

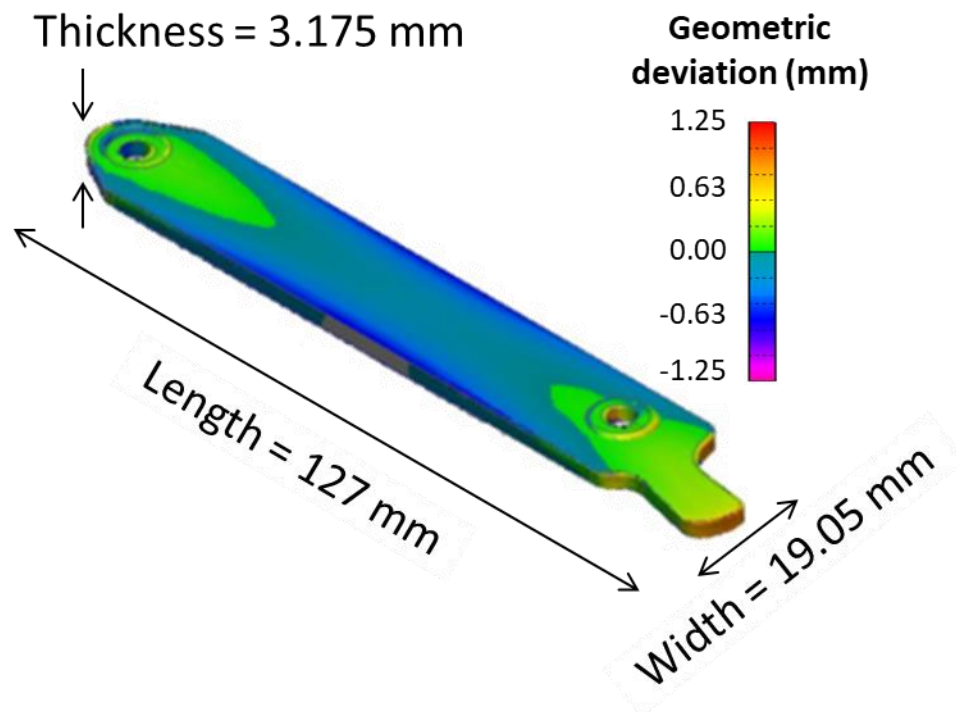


Figure 23. An example part that is flat and long that experiences warpage during BMD manufacturing.



## 2.2: Conceptualizing the DOE

Factors were chosen that could be easily controlled by a user to affect the outcome of a part. The factors were controlled either via CAD (SolidWorks), in the slicing software (Fabricate), or by operator interaction with the machines. The following sections describe in greater detail those factors, how they were controlled, and how they affected the part.

A 12-factor resolution IV fractional factorial DOE was conducted to determine the effect of factors on the warpage of flat rectangular BMD parts. Experimental factors included (a) part geometry (height [2.25-4.50 mm], width [20-30 mm], length [100-150 mm], print bed placement orientation [X, Y], thickness of top and bottom shell [0.6-1.2 mm], triangular infill density [34-64%]), (b) interface (density [67-100%] and thickness [0.15-0.45 mm]), (c) raft geometry (thickness [1.65-4.35 mm]), and (d) process conditions (cooling fan speed [0-80%], hold time after printing [1-12 hours], and furnace position [left side, right side]). The warpages on a total of 36 parts were measured via a Faro HD scanner at four processing points: before removal from print sheet, after removal from print sheet, after solvent debinding, and after sintering.

The large number of factors chosen prohibited the use of a full factorial design. A 12-factor full factorial design of experiments would contain  $2^{12}$ , or 4096 treatments. Instead of running that many treatments, a fractional factorial DOE was used. The choice of 32 run DOE ( $2^{12-7}$ ) was made from surveying the available options for 12 factors. The highest available resolution in Minitab for 12 factors was resolution IV, and the minimum number of runs to achieve a resolution IV DOE was 32, excluding center points (Figure 24). This results in a 1/128 fraction of the entire possible design space. With the inclusion of two categorical factors; print bed placement orientation and furnace position; the number of center points was  $2^2$ .

A resolution IV design is defined by its aliasing: main effects are not aliased with any other main effects or two-factor interactions, but two-factor interactions are aliased with other two-factor interactions [51]. Aliasing means that it's not possible to tell the difference between two factors or groupings of factors. Consequently, the results should be viewed keeping this in mind, especially the results showing the effect of factor interactions. The alias structure for the DOE can be viewed in Appendix H.

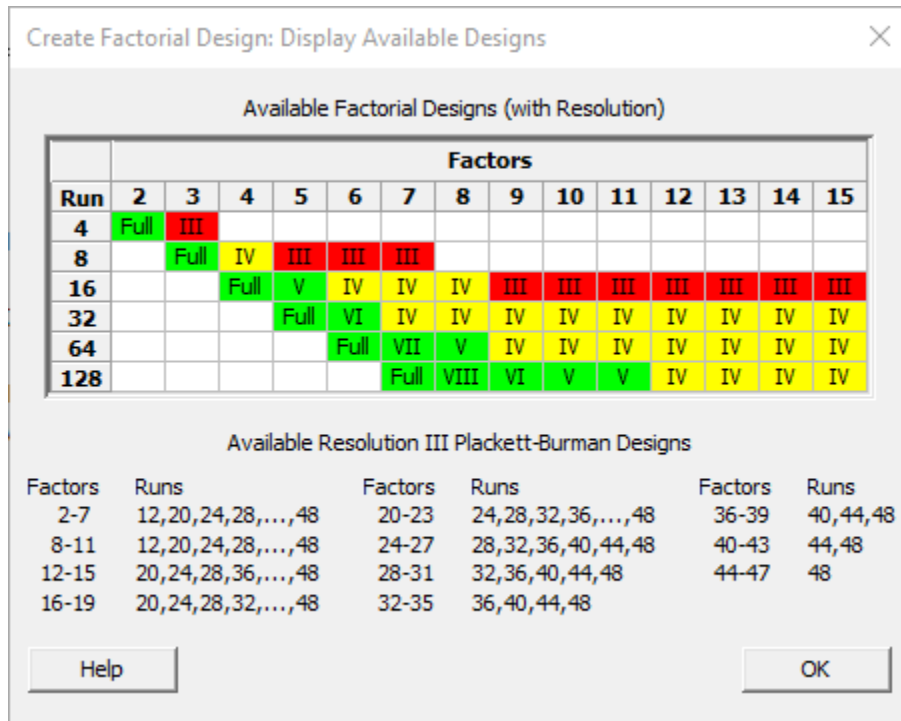


Figure 24. Available factorial designs dialog box in Minitab [52]

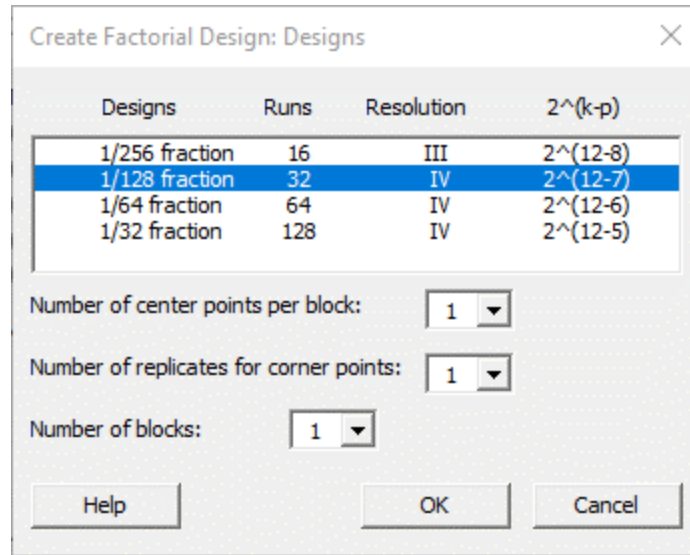


Figure 25. Create Factorial Design: Designs dialog box in Minitab [52]

### 2.3: Printing and Scanning Procedure

For a given treatment, applying of the factors was done at multiple process points. External geometry factors (height, width, and length) were applied by selecting one of nine available CAD models encompassing all the possible combinations for those 3 factors plus one more for the center points ( $2^3 + 1 = 9$ ). Next, factors were applied in the Fabricate slicer (print bed placement orientation, thickness of top and bottom shell, triangular infill density, interface geometry, raft geometry, and cooling fan speed). The last two remaining factors were controlled by the operator interacting with the machines (part hold time and furnace location).

At key processing points (after printing before and after separating from the print sheet, after debinding, and after sintering), a full scan of the part at extra-fine resolution via the FARO laser-line scanner coupled with PolyWorks software [53] was done, and from that scan, warpage was quantified by extracting a plane from the top surface of the part.

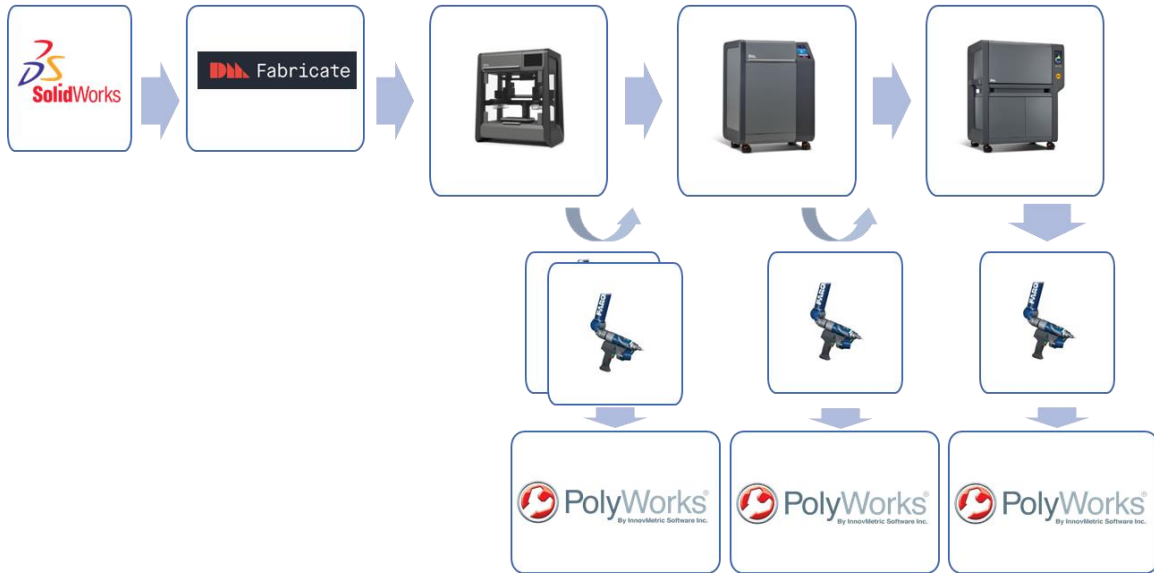


Figure 26. Visual overview of methods employed for the warpage study

### 2.3.1: Part Design in SolidWorks

A prismatic rectangular bar was selected for the DOE because its external geometry can be characterized fully by its length, width, and height. Because of this choice, the total number of external geometry combinations for 2-level factors, including one with center point values, was 9, i.e.,  $(2^3 + 1)$ . After design in SolidWorks, the geometry was sent to Fabricate and stored in the model database. From there, different part setups with different slicing parameters could be created to send to be manufactured. Table 4 shows all of the geometry setups and their model names within Fabricate, with “WarpSpec” being an abbreviated term for “Warpage Specimen” and an underscore number designation. For example, treatment 1 had a height of 4.5 mm, width of 30 mm, and length of 100 mm, so WarpSpec\_7 was used as the base geometry for that treatment.

Table 4. Dimensions of each possible part geometry from the combinations of the rectangular prism major dimensions

<b>Fabricate model name</b>	<b>Length (mm)</b>	<b>Width (mm)</b>	<b>Height (mm)</b>
WarpSpec_1	100.00	20.00	2.25
WarpSpec_2	150.00	20.00	2.25
WarpSpec_3	100.00	30.00	2.25
WarpSpec_4	150.00	30.00	2.25
WarpSpec_5	100.00	20.00	4.50
WarpSpec_6	150.00	20.00	4.50
WarpSpec_7	100.00	30.00	4.50
WarpSpec_8	150.00	30.00	4.50
WarpSpec_9 (centerpoint)	125.00	25.00	3.38

After being designed in SolidWorks, digital models were exported as .STL files, which were imported into Fabricate. At that point, the models were all stored in the Fabricate model library which held all the files digitally for ease of manufacturing.

### **2.3.2: Part Design in Fabricate**

Once the .STL file is imported into Fabricate, there are additional factors that are controlled in the slicing software. These factors include print bed placement, orientation, thickness of top and bottom shell, triangular infill density, interface geometry, raft geometry, and cooling fan speed. All these parameters are set in the slicer and captured in the gcode that is sent to the printer for part building.

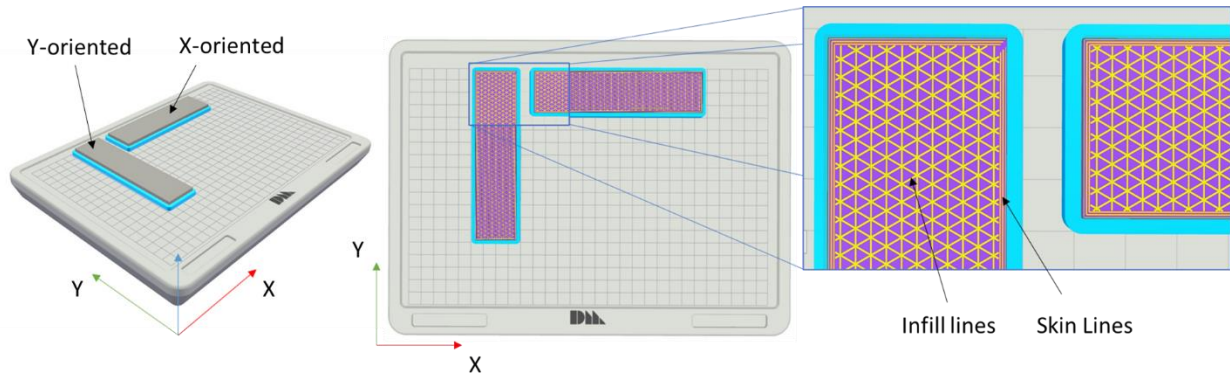


Figure 27. Different printing orientations shown in Fabricate

The print orientation was set in Fabricate by manually rotating the part around the z-axis. Warpage specimens oriented in the x-direction were defined with rotation values of X: 90°, Y: 0°, and Z: 0° (Figure 28). Warpage specimens oriented in the y-direction were defined with rotation values of X: 90°, Y: 0°, and Z: 90° (Figure 32).

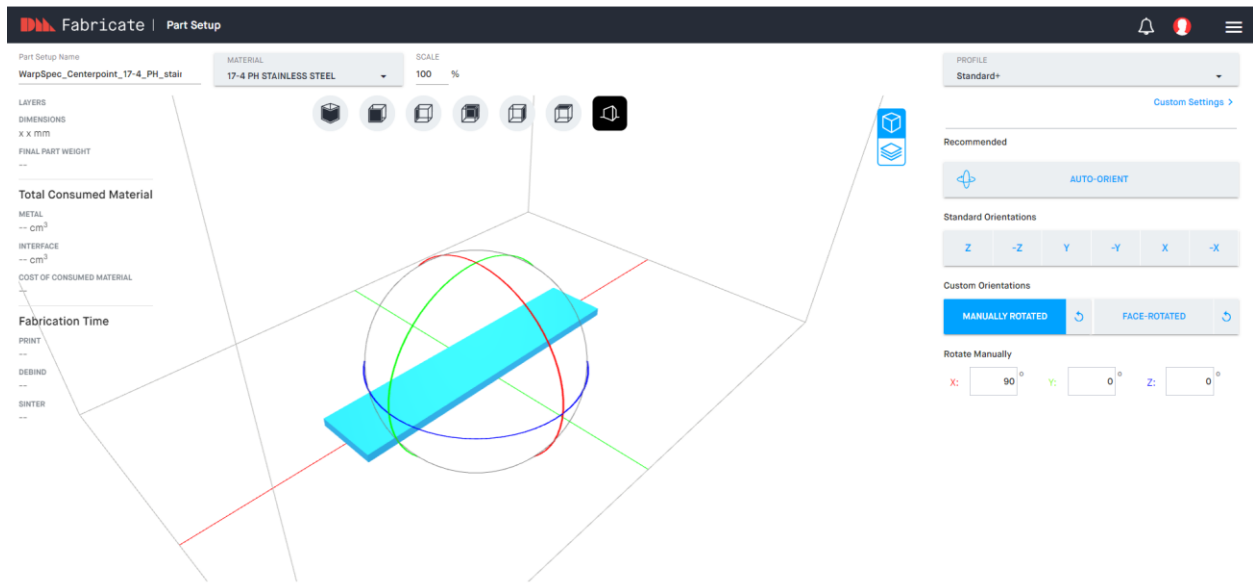


Figure 28. X-oriented warpage specimen

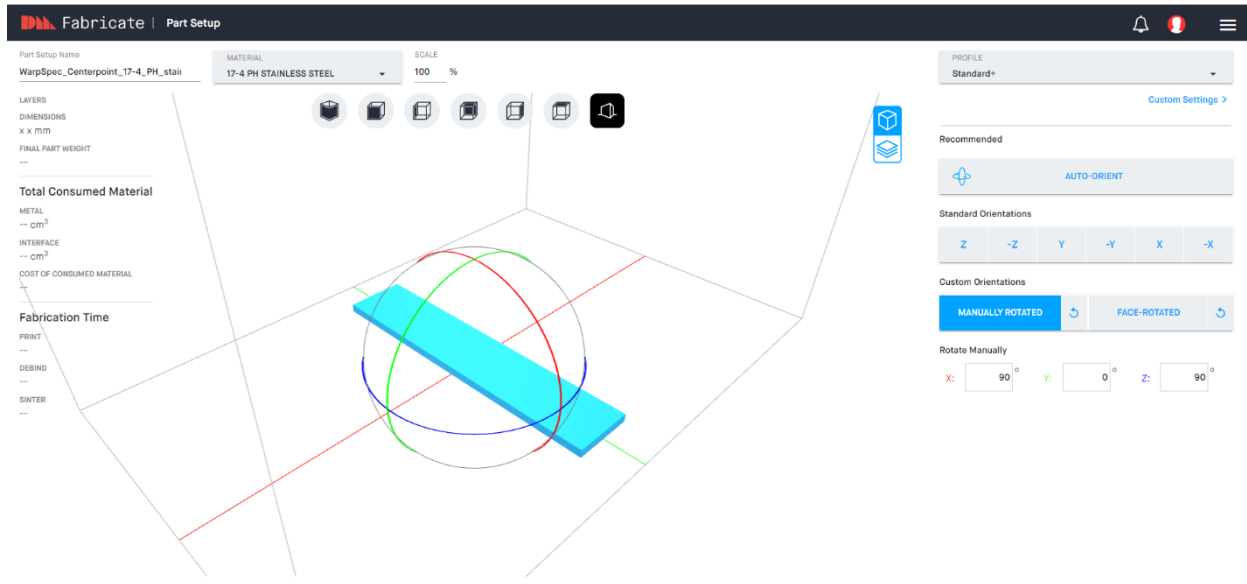


Figure 29. Y-oriented warpage specimen

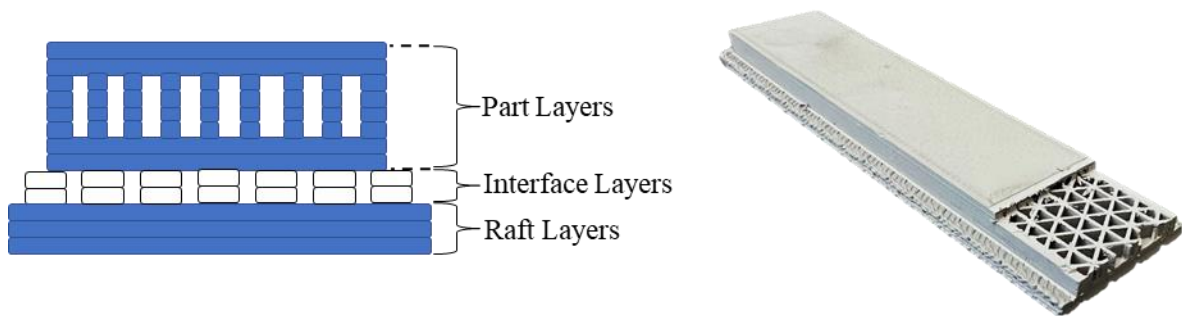


Figure 30. Cartoon (left) showing 2D slice of as-printed cross-section and a representative part (right) the top surface milled away to show infill.

### 2.3.3: Other Factors

Lastly, there are factors that depend on operator influence: part hold time and furnace location. Part hold time describes the amount of time after a print is complete that the part remains on the print bed with vacuum holding the print sheet down before the vacuum is released and the operator is allowed to remove the sheet from the bed. Print job completion depends on temperature setpoints of the print

chamber. At the time of experimentation, part hold time did not exceed 12 hours after print job completion.

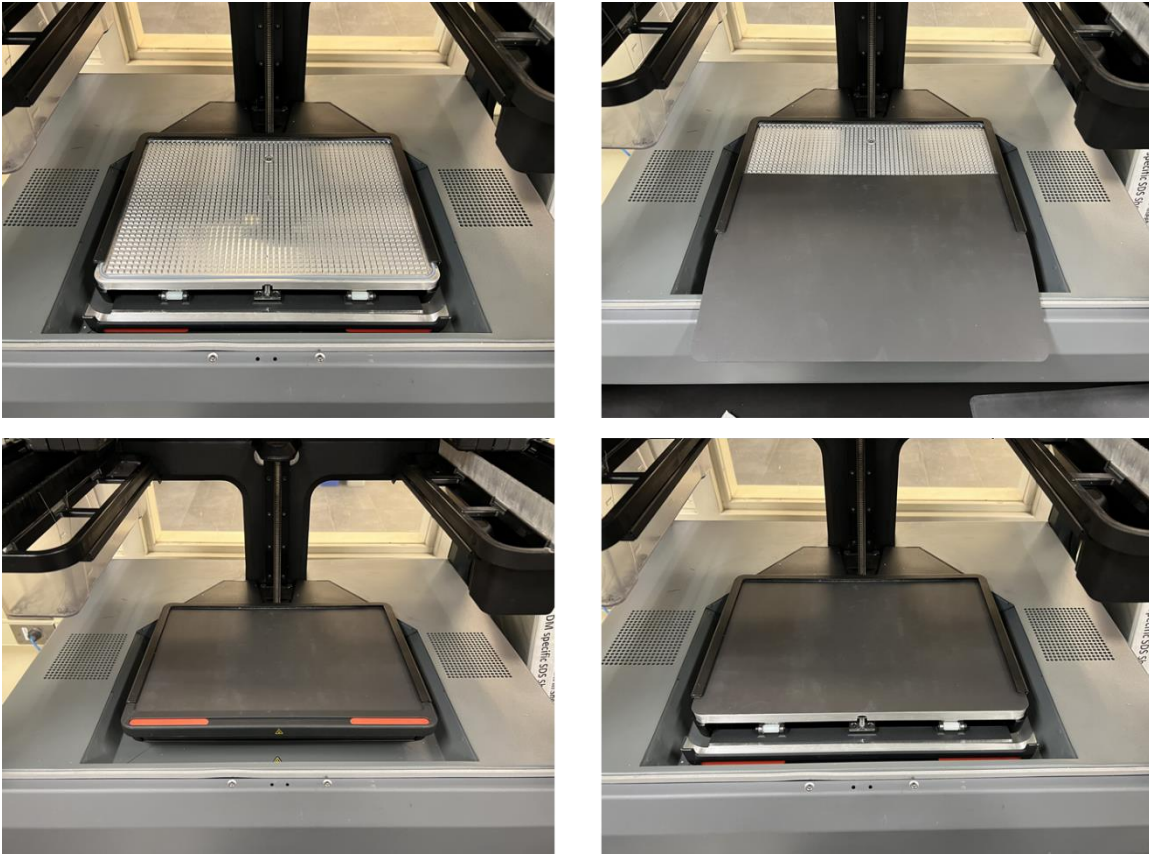


Figure 31. Installation of a print sheet onto the vacuum platform

Furnace location refers to either the left or right side of the furnace tray. Regardless of their printing orientation, parts were oriented in the furnace with the part's major lengths parallel to the left and right sides of the furnace tray, as shown in Figure 32. Parts spanned two setter plates. Some of the parts with smaller geometries could have fit on a setter plate diagonally, but for experimental consistency, all parts were placed with the orientation shown in Figure 32.



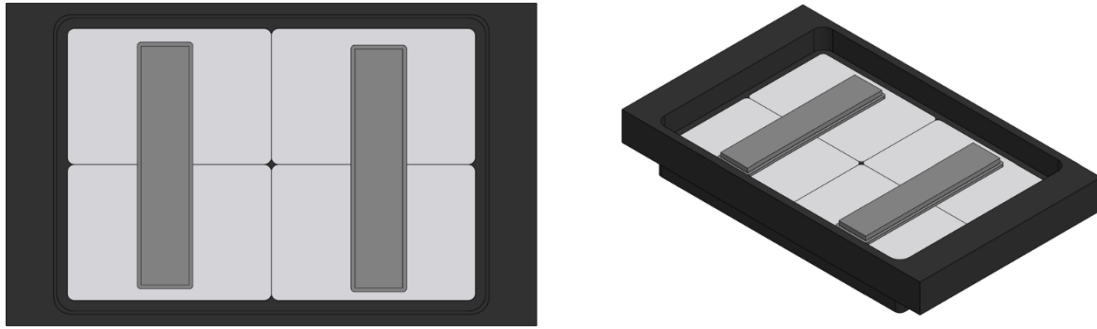


Figure 32. Layout of two warpage specimens on furnace tray

#### 2.4: Part Processing for Warpage DOE

Due to space limitations from the experimental setup, not all parts could be sintered simultaneously. As such, there was a need for batch processing.

While the printer has the surface area capacity to print multiple parts at once, the decision was made to print with a single part in the build volume at a time. This choice reduces the amount of time a layer will cool down before material from the next layer is deposited. This could have a potential impact on the interlayer strength of the part. If the deposited layers do not bond together, the spacing between rasters would be affected, and a gap would prevent particles from touching between layers, prohibiting sintering later in part processing. Studies have shown that inter-layer bond strength increases with increased temperatures of the nozzle and build plate for FFF of polymers [54]. However, it is difficult to compare BMD to FFF in this way due to fundamental material differences in the wax-polymer binder material to the typical polymers found in FFF. Although printing one part at a time can reduce the dwell time of a layer before the next layer of material is deposited, the automatic reloading of material into the printhead may negatively impact the dwell time, which we seek to minimize. Material loading in the DM Studio System printer occurs whenever the currently loaded rod of material runs low. The autoloading occurs automatically and appears to function without consideration of the part geometry, and only when the material loaded reaches a certain low setpoint. The entire printing process must halt

to allow the printing nozzle to cool down to loading temperature before the printhead moves to the loading location to receive a new rod. This process causes a discontinuity in printing that could potentially catalyze poor adhesion or crack propagation later in the process.

After printing, the parts were loaded into the debinder. The debinder is capable of batch processing of parts. Debinding time is automatically calculated in the Fabricate Software. The number of parts that could be processed in a single batch was limited by the furnace capacity. To try and promote experimental consistency, only two parts were placed on a single retort level (Figure 33) and only the top 5 levels of the retort were used because they were removable. The lowest level of the retort was fixed to the bottom of the furnace, which was not desirable because the parts were scanned as they lay on the furnace after sintering. To achieve this, the tray needed to be removed from the furnace carefully to avoid the parts sliding. With the imposed limitations of the number of parts per tray and the number of trays per furnace run, at most, 10 treatments could be done at a time in a single furnace batch.



Figure 33. Layout of parts on setters in a retort layer

## 2.5: Qualitative Warpage Results

To demonstrate the meaningful results of the warpage study, two treatments that have the same processing parameters except for the length and the height were chosen to compare in Figure 34.

Treatment 1 had the low level for length (100 mm) and the high level for height (4.5 mm). For treatment 13, the length was at the high level (150 mm) and the height was at the low level (2.25 mm). As shown in Figure 34, the warpage measured from the as-printed on and off sheet and debound states was little

for both treatments, and this is representative of the entire population. The most warpage was induced by the sintering process, and it can be seen in the as-sintered row of Figure 34 that the warpage was concave up. Note that the amount of as-sintered warpage was less for treatment 1 (0.44 mm deviation from flat) compared to treatment 13 (2.25 mm deviation from flat).

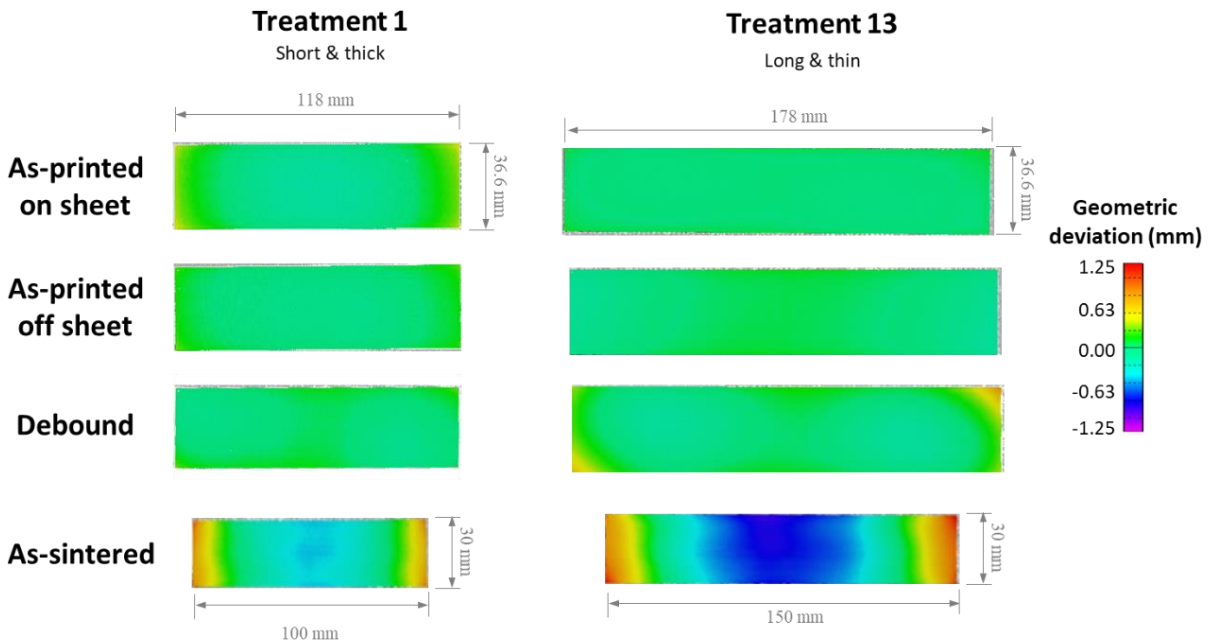


Figure 34. Treatment 1 and treatment 13 warpage comparison

## 2.6: Warpage DOE Analysis and Results

### 2.6.1: Regression Equations

Regression equations generated with Minitab [52] are in either coded or uncoded units [55]. Coded units mean that the low and high settings for a factor are identified by a -1 or 1, respectively in the equation. If the units are uncoded, then the units correspond to the quantities of the factors. For example, the height factor has a low-level of 2.25 mm and a high-level of 4.50 mm. In coded units, the low level would be -1 and the high level would be 1, whereas with uncoded units, the low-level would be

2.25 and the high level would be 4.50. The general form for the regression equation is shown in Equation 3.

$$w_s = \beta_0 + \sum_{j=1}^{m=12} \beta_j x_j + \sum_{i<j} \beta_{ij} x_i x_j + \sum_{j=1}^{m=12} \beta_{jj} x_j^2 + \sum_{i<j<k} \beta_{ijk} x_i x_j x_k + \sum_{j<k} \beta_{jjk} x_j^2 x_k \quad (3)$$

The differentiator within Minitab on whether the regression equation would be in coded or uncoded units was if the model was hierarchical. A hierarchical model is one that contains all lower-order terms of the highest order terms within it [56]. For example, if a model contains A\*B\*C, then the terms A, B, C, A\*B, A\*C, and B\*C must also be contained. If the model was hierarchical, the equation could be reported in uncoded units. If the model was non-hierarchical, uncoded units were not available and coded units were used instead.

#### 2.6.1.1: Green, On-Sheet Warp Regression Equation in Coded Units

$$w_{onsheet} = 0.3570 - 0.0329 A - 0.0829 D + 0.0321 F - 0.0739 K + 0.0526 B * M \quad (4)$$

where  $w_{onsheet}$  is the green, on-sheet warpage in mm,  $A$  is height,  $B$  is width,  $D$  is print bed orientation,  $F$  is infill line distance,  $K$  is cooling fan speed, and  $M$  is parts hold time.

#### 2.6.1.2: Green, Off-Sheet Warp Regression Equation in Coded Units

$$w_{offsheet} = 0.2485 - 0.0734 D - 0.0386 E + 0.0399 F - 0.0742 K + 0.0309 AB - 0.0286 AH + 0.0393 BF + 0.0459 BM \quad (5)$$

where  $w_{offsheet}$  is the green, off-sheet warpage in mm,  $A$  is height,  $B$  is width,  $D$  is print bed orientation,  $E$  is the top and bottom layer count,  $F$  is infill line distance,  $H$  is the interface layers,  $K$  is cooling fan speed, and  $M$  is parts hold time.

### 2.6.1.3: Brown Warpage Regression Equation in Coded Units

$$w_b = 0.6602 + 0.1027 C - 0.1004 D + 0.0699 G + 0.0844 J + 0.1300 K + 0.0652 AB - 0.0671 AC + 0.0768 AH + 0.1567AM - 0.1110 Ct Pt \quad (6)$$

where  $w_b$  is the brown, or rebound, warpage in mm,  $A$  is height,  $B$  is width,  $C$  is length,  $D$  is print bed orientation,  $G$  is raft top layers,  $H$  is interface layers,  $K$  is cooling fan speed, and  $M$  is parts hold time. The  $Ct Pt$  term is at 1 if the variables are at their midpoint and 0 otherwise.

### 2.6.1.4: Sintered Warpage Regression Equation in Uncoded Units

$$w_s = -2.094 + 0.532 A + 0.03324 C - 0.00697 AC - 0.165 Ct Pt \quad (7)$$

where  $w_s$  is the sintered warpage in mm,  $A$  is height,  $C$  is the length. The  $Ct Pt$  term is at 1 if the variables are at their midpoint and 0 otherwise.

## 2.6.2: Pareto Charts

Analyzed data from Minitab can take the form of a Pareto chart, a special kind of bar chart [57]. In displaying these results, bar width corresponds to the effect the factor has on the warpage, with a wider bar having a greater effect on warpage than a narrower bar. The models considered up to third-order

interactions. For example, in the first Pareto chart, term D, which represents the print bed orientation, shows up as the most influential factor for warpage of the part in the green state on the print sheet. An example of a two-factor interaction is term BM, which indicates that the interaction between the part width and the parts hold time is significant in the on-sheet warpage.

The factorial regression analysis within Minitab used backward elimination of terms to discern statistically significance in the terms that would end up in the final model, and as a result, the pareto charts shown only contain the statistically significant factors. The backward elimination used  $\alpha$  of 0.05 to remove terms, which translated to a 95% confidence interval [58]. The p-value for a term is compared to the  $\alpha$  value. If the p-value is less than or equal to the alpha value, it is statistically significant. Otherwise, the term is dropped from the model.

The bars on a pareto chart correspond to the absolute values of the standardized effects. A standardized effect quantifies the t-statistics that test the null hypothesis that the effect is zero. The greater the effect is, the greater the size of the bar on the pareto chart. In other words, if the null hypothesis is rejected, then it is concluded that the effect is significant in explaining the response [57], [59].

The first Pareto chart shown in Figure 35 shows the factors that influence the warpage of the part in the green state prior to separation from the print sheet.

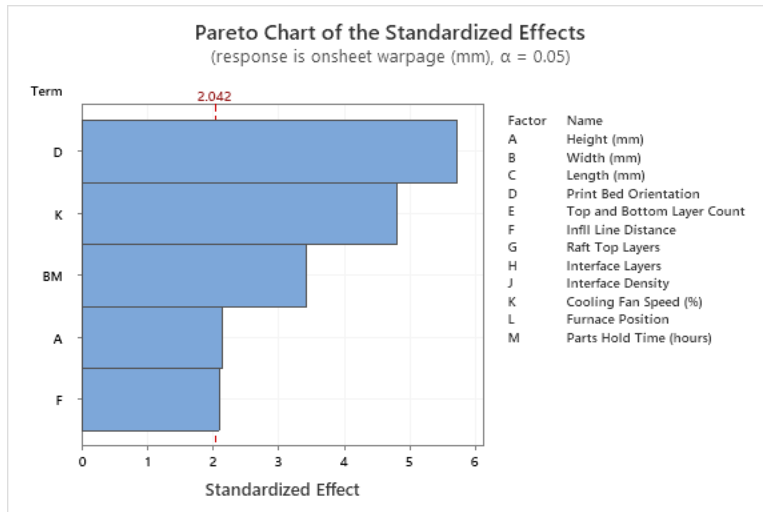


Figure 35. Pareto chart showing warpage of the part on the sheet

Figure 36 shows the factors that influence the warpage of the part in the green state after the operator mechanically separated the green-state part from the print sheet.

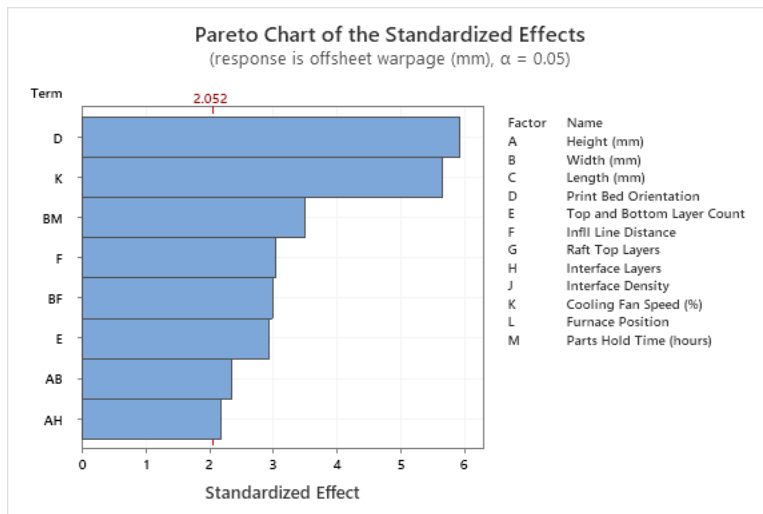


Figure 36. Pareto chart showing warpage of the part after removal from the print sheet

Figure 37 shows a Pareto chart for the factors that influence the warpage of the part in the brown state after removal from the solvent debinding step.

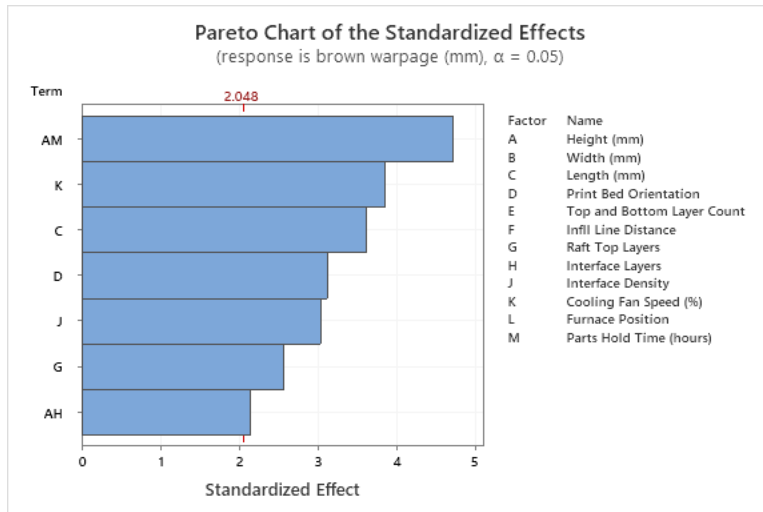


Figure 37. Pareto chart showing warpage of the part in the brown state, after removal from the solvent debinding

Figure 38 shows a Pareto chart of the factors that influence the warpage of the part in the sintered state after removal from the furnace.

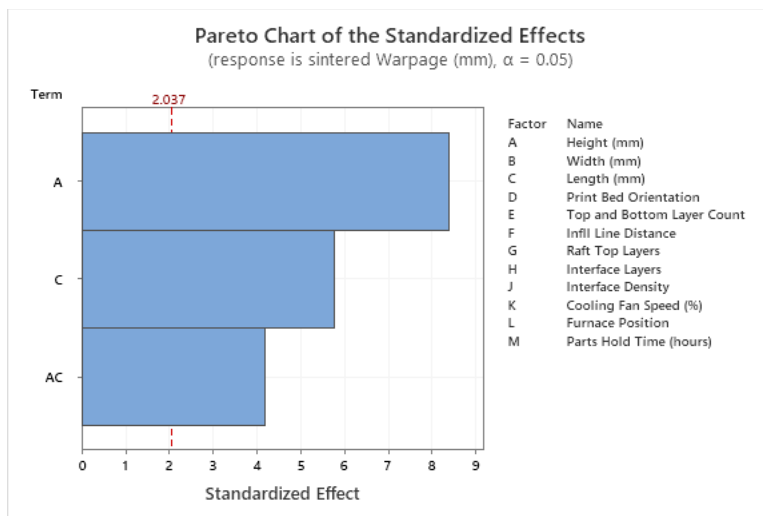


Figure 38. Pareto chart showing warpage of the sintered part, after removal from the furnace

### 2.6.3: Main Effects Plots

The Pareto charts are very useful for quickly determining which factors influence the warpage the most, but they have no indication of how they influence warpage, e.g., which factor level increases or decreases warpage. Main effects plots display the relationship between the response and the individual



variables [60]. The slope of the line indicates whether the low or high level of a factor will increase warpage. For example, a main effect plot with a positive slope means the high level of the factor will cause more warpage than the low level. Conversely, if the slope is negative, then the low level of the factor will cause a greater warpage than the high level. For example, in Figure 39, The negative slope in the height block indicates that increasing the height tends to decrease the response, warpage.

The single terms that were statistically significant for predicting warpage while the part was attached to the print sheet were height, print bed orientation, infill line distance, and cooling fan speed as shown in Figure 39.

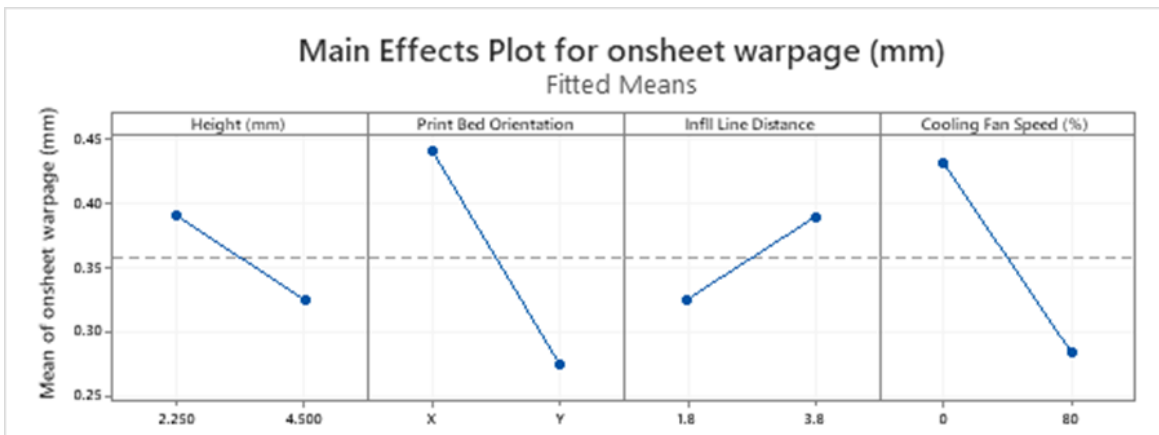


Figure 39. Main effects plot showing first level effects of each factor on the warpage on-sheet.

The single terms that were statistically significant for predicting the warpage after the part was separated from the print sheet were print bed orientation, top and bottom layer count, infill line distance, and cooling fan speed as shown in Figure 40.

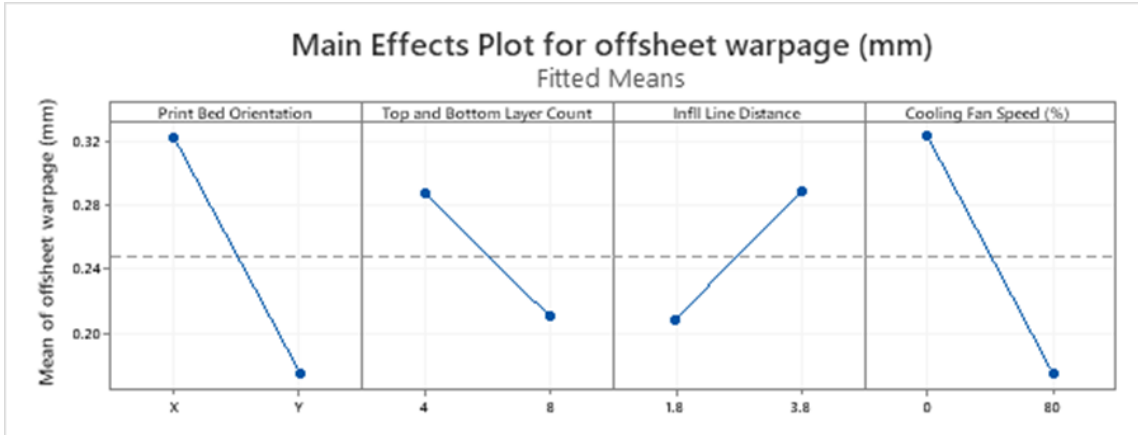


Figure 40. Main effects plot showing first level effects of each factor on the warpage off-sheet.

The single terms that were statistically significant for predicting the warpage after the part was removed from the solvent debinding process were length, print bed orientation, raft thickness, interface density, and cooling fan speed as shown in Figure 41.

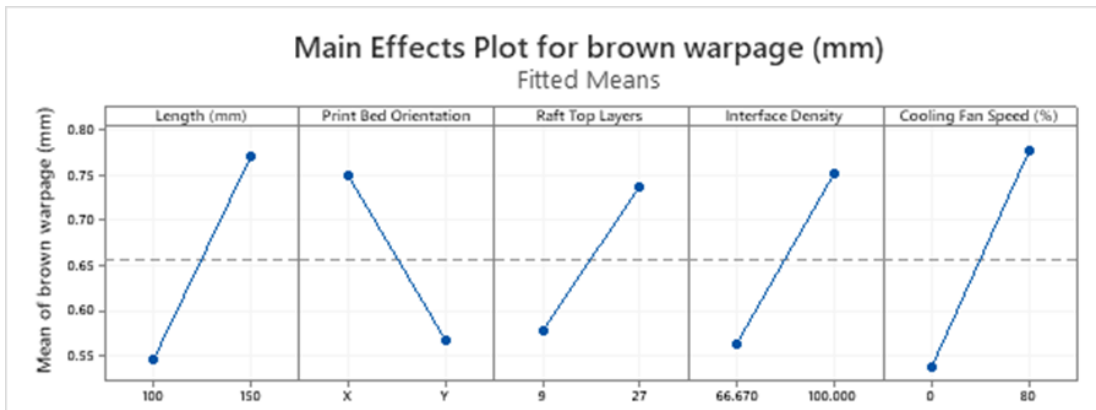


Figure 41. Main effects plot showing first level effects of each factor on the warpage after debinding.

The single terms that were statistically significant for predicting the warpage of the sintered part were height and length as shown in Figure 42.

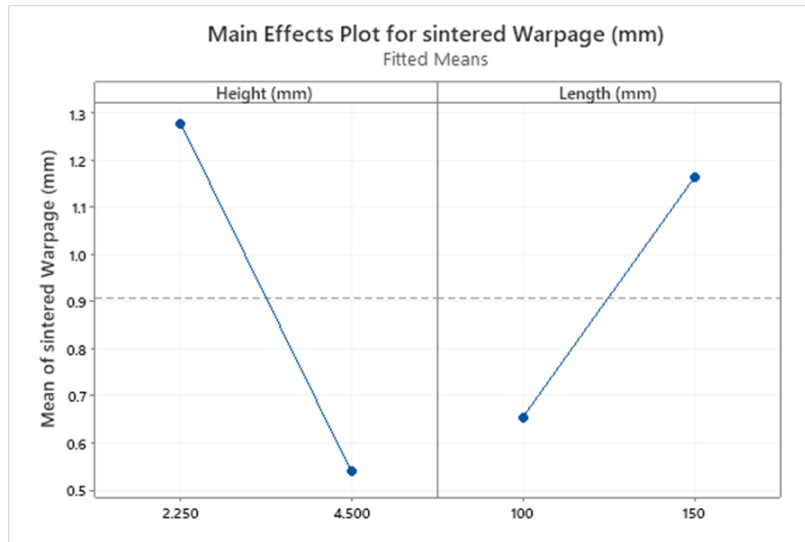


Figure 42. Main effects plot showing first level effects of each factor on the warpage after sintering.

## 2.7: Warpage DOE Discussion

Comparing the warpage of a part before and after it was removed from a print sheet revealed that the top surface deviation from flatness was greater before peeling the part off of the print sheet. This may be due to the print sheet's stiffness resisting shrinkage that the part is prone to during cooling. It has been observed in material cooling rapidly to room temperature, a large curvature can be created in a part while it is still attached to its print sheet. The difference of the thermal expansion in the green material and the print sheet that it adheres to during printing can be blamed for this occurrence. To combat this phenomenon, the Studio System printer hardware has built in hold time to hold the print sheet down flat to the machine until the part is cooled enough to release and keep the part flatter.



Figure 43. Print jobs that were halted during printing that allowed for an abnormally high cooling rate. Although it was not measured in this research, the author recommends that a part be removed from the print sheet as quickly as possible to avoid imparting undesirable curvature to a part. If the part is removed immediately after printing, this could give the part a chance to continue cooling free from the print sheet and avoid curving more than is desirable.

It was also observed that warpage of a part during either the green or brown state did not predict the warpage in the as-sintered state. The part height and length were the only two factors that could predict warpage in the sintered state, but there was a myriad of other factors that predicted warpage in the green state.

Overall, there were some areas that could be delved into deeper to try and eliminate more variables in determining the cause of warpage. A follow-up study with warpage specimens sized to avoid spanning multiple setter plates could eliminate the effect that setter plate spanning has on the outcome of the parts. Increased attention to positioning in the retort (distance from retort edge, distance from other parts, which retort level was used) could also be valuable in understanding how the retort thermally effects the warpage of the part.

## CHAPTER 3: DILATOMETRY

Dilatometry is a technique that measures length change with respect to temperature. This is a common technique used to measure thermal expansion. The thermal expansion properties of BMD 17-4PH stainless steel during the furnace step are important to know to help understand what causes failures such as warpage and cracking. This data can be used to aid in simulation of the sintering process by implementing into a computational model.

Dilatometry testing was performed by HJE Corporation (HJECO) on six solid rectangular prism pieces. Solid parts were printed by increasing the top/bottom thickness of the part to 100, an arbitrary value chosen to ensure no infill would be generated because the number of top and bottom layers exceeded the number of total layers in the part (i.e., the number of top and bottom layers > total layer count). The dimensions of the part were chosen based on the volume restrictions of the hardware at HJECO, as well as for ease of analysis and processing. The dimensions of the parallelepipeds were 0.675-inch length, 0.500-inch width, and 0.275-inch height. This geometry was chosen to fit within the dilatometry equipment [30].

### 3.1: Preparation of Dilatometry Specimens

Pieces were printed with the length directions varied along the three major Cartesian coordinates, *i.e.*, X, Y, and Z, relative to the build volume assuming a right-handed coordinate system representing the BMD printer's build volume. For each direction, two replicates were printed and solvent debound at UMaine. The dilatometry specimens were printed two at a time, for a total of three printing jobs.

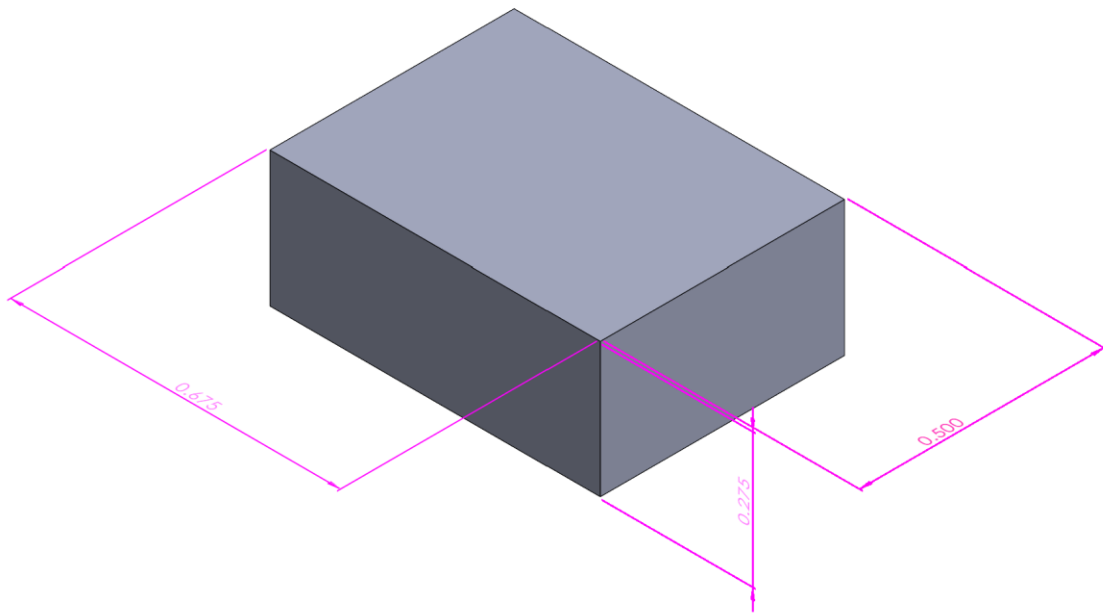


Figure 44. Geometry for XYZ dilatometry specimen showing major dimensions

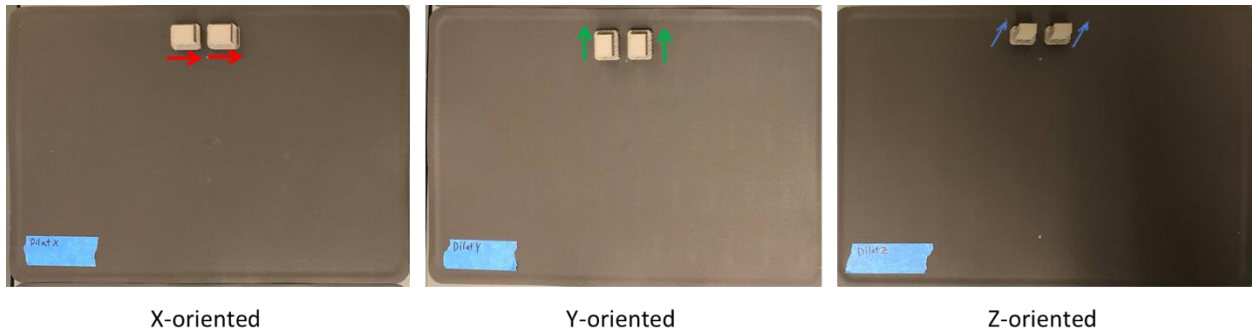


Figure 45. Green-state X-, Y-, and Z-oriented dilatometry specimens Printing layout for dilatometry specimens, colored arrows denote direction of length orientation

After printing and peeling the green-state parts from the print sheets, all six dilatometry specimens were characterized via digital calipers for major dimensions and a mass balance for part mass. The specimens were then debound for approximately 68 hours per DM's Fabricate algorithm.

Two brown-state specimens – one X-orientated specimen, and one Z-oriented specimen – were sputter coated (Figure 46) with a 4-nm of gold in preparation for Scanning Electron Microscopy (SEM) imaging. Sputter coating a 4-nm gold layer increases the amount of secondary electrons on all surfaces to promote a greater signal to noise ratio [61].

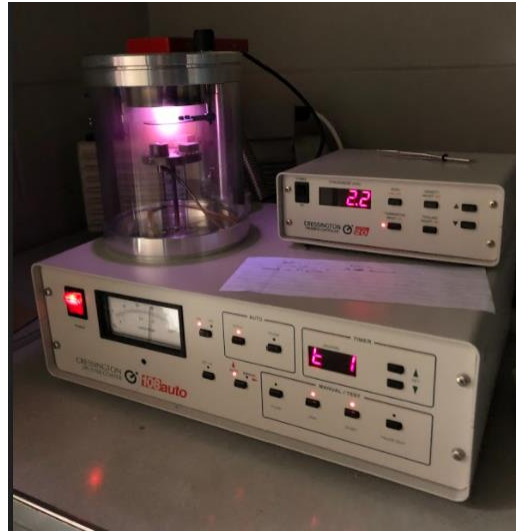


Figure 46. Cressington Sputter Coater 108 auto during coating process

SEM imaging was performed on two different SEM machines, the Nvision 40 and AMRAY 1820, both located on the University of Maine's Orono campus.



Figure 47. SEM machines: Nvision 40 (left) and AMRAY 1820 (right).

### 3.2: Dilatometry Specimen Micrographs

In Figure 48, we are looking at the raft interface that has been separated from the part of one of the z-oriented dilatometry specimens in the brown (post-solvent debind) state. Three vertical lines shown on the image on the left show the interface material on top of the metal media. The ceramic interface media is made up of approximately 50- $\mu\text{m}$ -diameter spheres in a binder material.

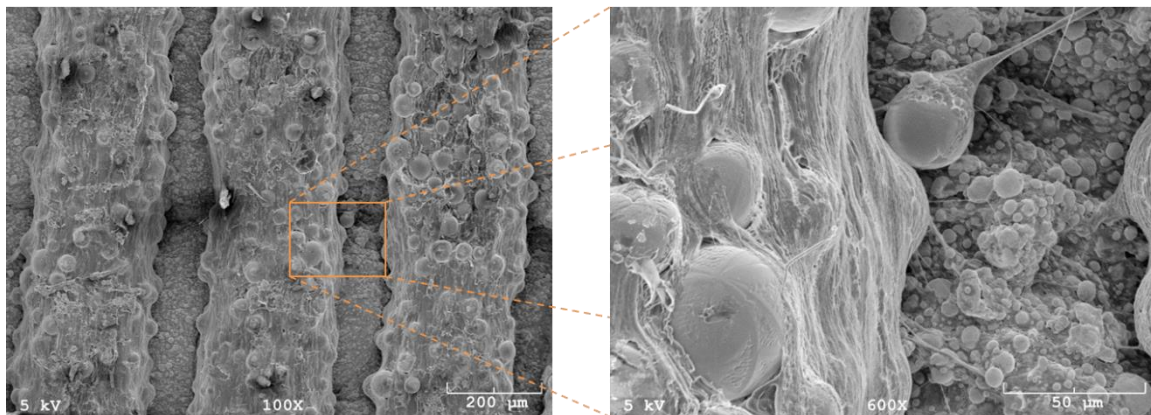


Figure 48. SEM image of a brown state ceramic interface material (larger, more spherical particles) and 17-4PH stainless steel material (smaller, more irregular particles)



### 3.3: Dilatometry Testing

After the SEM imaging was completed, dilatometry specimens were shipped to HJEco to perform the dilatometry testing. Out of the two of each configuration (X, Y, or Z), only one part was tested and the other was for backup in case of damage during handling. The temperatures for the dilatometry processing were chosen to mimic Kwon et al. [62], a previous work from the literature in which dilatometry results were found for powder-injection-molded 17-4PH stainless steel. The thermal profile for the dilatometer runs followed the list below and is shown in Figure 49.

1. Room temperature to 350 °C @ 10 °C / min
2. 60 minute hold at 350 °C
3. 350 C to 450 °C at 2 °C/min
4. 60 minute hold at 450 °C
5. 450 C to 1000 °C at 10 °C/min
6. 60 minute hold at 1000 °C
7. 1000 °C to 1370 °C at 10 °C/min
8. 60 minute hold at 1370 C
9. Furnace cool.

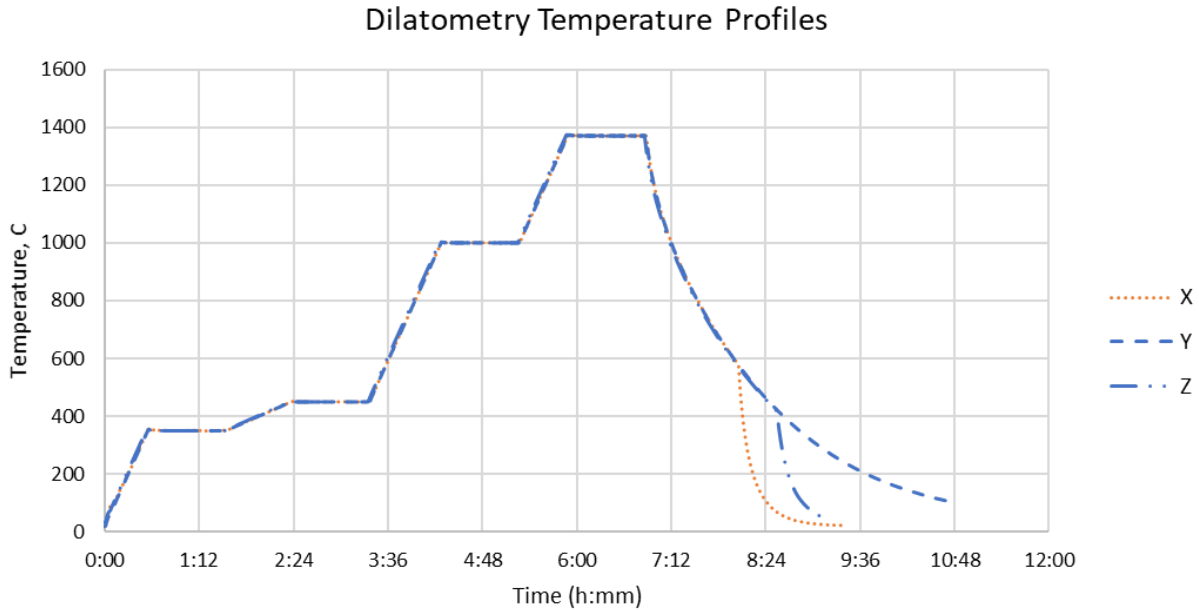


Figure 49. Temperature profiles used in HJEco dilatometry test

The dilatometry apparatus used at HJEco consisted of a pushrod dilatometer that applies a force to the specimen and measured displacement during heating. Due to thermal expansion and densification, the specimen changed size due to exposure to high temperatures is captured by the pushrod and recorded alongside temperature and elapsed time. The pushrod exerts a force of about 60 grams, spread out over a plate approximately 0.42-in by 0.35-in, which results in a pressure of about 0.9 psi or  $0.025 \frac{\text{kg}}{\text{cm}^3}$ . An atmosphere of pure hydrogen was used for the entire thermal cycle.

In addition to the dilatometry test, HJEco also measured the dimensions of the parts before and after sintering with a pair of standard vernier calipers. Due to geometric non-uniformities, the accuracy of the caliper dimensions are expected to be within  $\pm 0.005$  in. Density measurements based on the principle of water displacement were also conducted via ASTM B962 [63].



Figure 50. Dilatometry setup

### 3.4: Dilatometry Results

Plotting the temperature against the percent dilation gives the dilatometry curve in Figure 51. In general, each plot contained noticeable attributes. Around 150°C to 170°C there was an abrupt dilation of the material which can be attributed to the softening of the binder material, which although proprietary is likely a thermopolymer. The initial sintering shrinkage begins to occur at 900°C, and isothermal sintering occurs at 1000°C during the first temperature hold. There is an increase in the sintering rate around 1250°C. At 1340°C, the sintering rate decreases, which can most likely be attributed to the porosity becoming more difficult to eliminate as the free surface energy is reduced due

to particle densification. At 1370°C, there is only a small amount of shrinkage recorded over the 60-minute hold time.

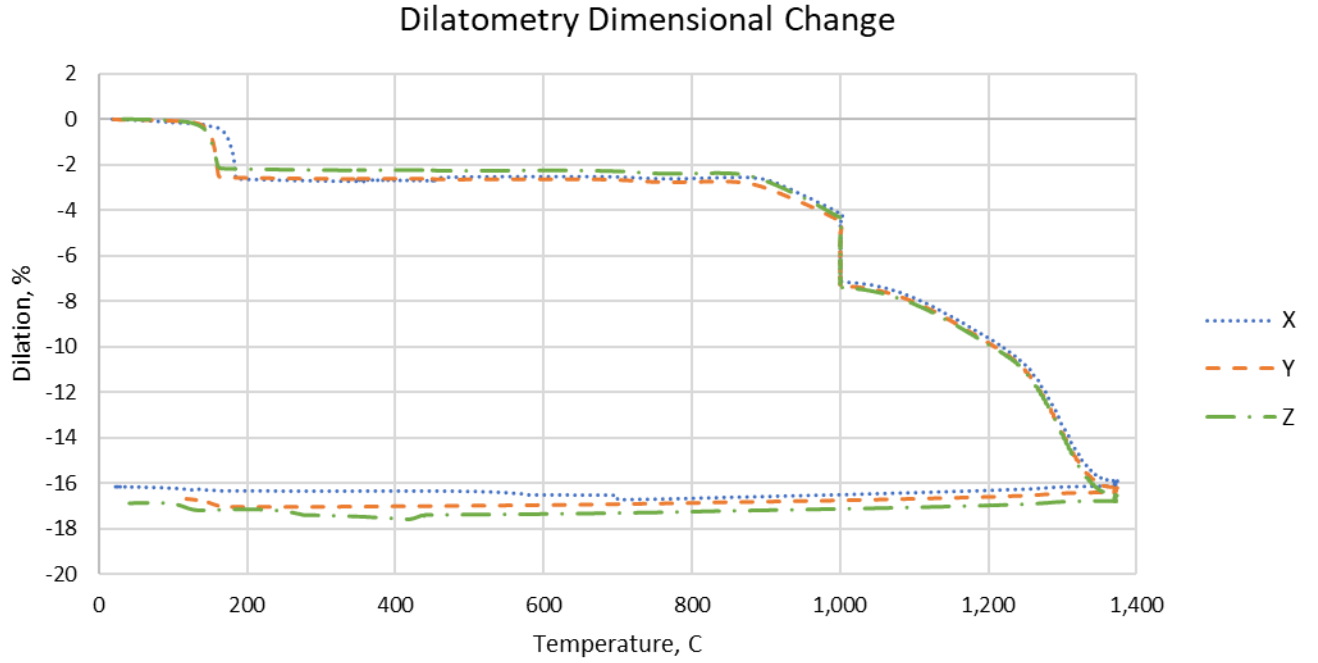


Figure 51. Comparison of dilatometry results for X, Y, and Z printed specimens

The results can also be compared to Kwon et al. [62] by setting the zero-shrinkage starting point to the temperature data after the binder softening (Figure 52).

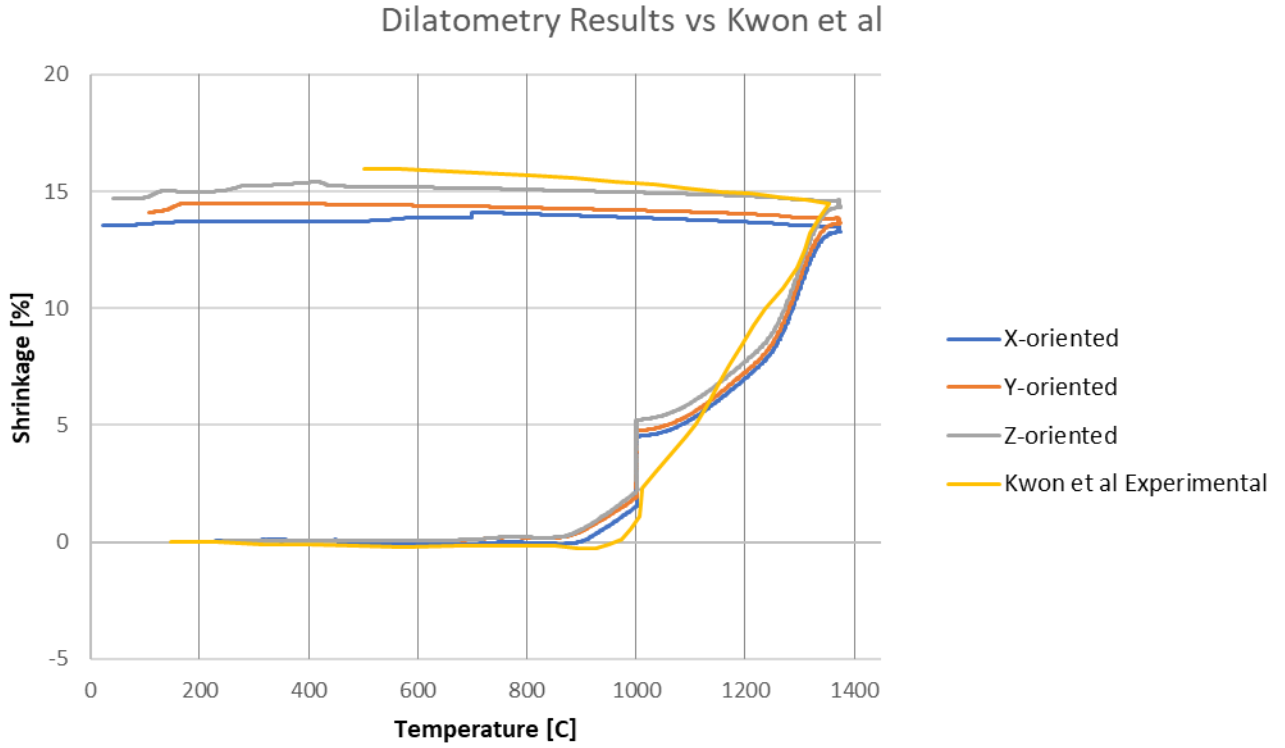


Figure 52. Dilatometry curves of HJEco test compared to Kwon et al. [62].

## CHAPTER 4: LASER ABLATED BOUND METAL DEPOSITION STUDY

### 4.1: Introduction

#### 4.1.1: Laser Ablation

Laser ablation is the process of machining or etching a part by subjecting a surface of the part to a focused laser (light amplification by stimulated emission of radiation) beam. In accordance with Beer Lambert's law, the absorbed radiation for a homogeneous material depends upon the material's radiation path length [64], [65]. The absorbed radiation heats a local region, which liquifies or vaporizes once sufficiently heated. In addition to large recoil pressures, vaporization also causes an elastic-plastic wave in the surface, ejects material, and is the primary material removal phenomenon [66].

Additionally, localized heating via laser ablation may result in a heat affected zone and debris ejection from non-ablated surfaces.

A phenomenological model of laser ablation processes for laser pulse durations less than the electron-phonon relaxation time [67], [68] assumes  $D = \frac{1}{\alpha} \ln \left( \frac{F}{F_{th}} \right)$ , where  $D$  is the ablated depth in  $\mu\text{m}$ ,  $\alpha$  is the characteristic optical penetration depth in  $\frac{1}{\mu\text{m}}$  at which the surface energy density reaches  $e^{-1}$ ,  $F$  is the laser fluence in  $\text{J}/\text{cm}^2$ , and  $F_{th}$  is the fluence ablation threshold in  $\text{J}/\text{cm}^2$ . The phenomenological model has been applied to metallic material systems subjected to femtosecond and picosecond laser pulse durations [67] and to polymeric material systems subjected to picosecond laser pulse durations [68]. For laser pulse durations that greatly exceed the electron-phonon relaxation time, the phenomenological model simplifies to the classical heat conduction equation, with heat penetration depth found as  $D_h = \sqrt{\kappa t}$ , where  $\kappa$  is the heat diffusion coefficient  $\kappa = \frac{k}{\rho c_p}$ ,  $k$  is the thermal conductivity in  $\frac{\text{W}}{\text{m K}}$ ,  $\rho$  is density in  $\frac{\text{kg}}{\text{m}^3}$ ,  $c_p$  is the specific heat at constant pressure in  $\frac{\text{J}}{\text{kg K}}$ , and  $t$  is time in seconds. Additionally, numerical models have been implemented to predict ablation of homogeneous materials in one dimension [69], two dimensions [70], and three dimensions [71].

The laser ablation of composite or inhomogeneous materials, such as a binary composite of spheroidal metallic powders and binder utilized in BMD, presents additional challenges. Slocombe and Li [72] studied the removal rate and surface finish as a function of laser power, scanning speed, and Argon gas assist for a 75-watt Nd:YAG laser ablating 50% spheroidal metallic powder and 50% low-temperature polymer by weight. Slocombe and Li's results indicate machining depths from approximately 250 to 10  $\mu\text{m}$  for scanning speeds between 2 and 20 mm/s, respectively, at a laser power of 70 watts and a laser frequency of 20 kHz. Although laser ablation of composite materials of spheroidal metallic powders is possible [72], Slocombe et al. [73] demonstrated that ablation of composites with irregular-shaped metallic powders is difficult. Slocombe and Li [72] hypothesized that the ablation mechanism was energy transfer from the laser to the metallic powder via absorption, and from the metallic powder to the polymer via conduction, causing the polymer to vaporize and eject metallic powder.

#### **4.1.2: Research Objective**

The objective of this work is to demonstrate a novel hybrid manufacturing process capable of economically incorporating fine-length-scale features to AMM parts. The demonstrated process utilizes laser ablation to create fine-length-scale features within an established bound metal deposition AMM process. The first part of this chapter presents experimental methods and results, discussion, and a conclusion.

### **4.2: Methods**

#### **4.2.1: Manufacturing**

A total of four 17-4 PH specimens were manufactured using a DM Studio+ printer with the manufacturing workflow shown in Figure 53. The manufacturing workflow was initiated by creating the 50 mm  $\times$  50 mm  $\times$  5 mm desired as-sintered geometry in SolidWorks 2020 [74] and slicing the desired as-sintered geometry with the 50 mm  $\times$  50 mm face parallel to the build plane in DM Fabricate v2.14

[11]. To account for sintering shrinkage, Fabricate increased the to-be-printed green state geometry by 19.07% in the build plane and 18.55% out of the build plane, resulting in as-designed green state dimensions of 59.54 mm × 59.54 mm × 5.93 mm. Slicing utilized Fabricate’s default Standard+ slicing parameters, resulting in a 1.44-mm sidewall thickness, 400- $\mu$ m-diameter nozzle, 0.15-mm layer height, and 1.80-mm-thick 100%-infilled region on the top and bottom of the part in the green state. Subtracting the 1.80-mm-thick regions at the top and bottom of the part from the 5.93-mm overall part height resulted in a 2.33-mm thick region in the middle of the part. The middle region contained a triangular infill having a 17.14% density. The default Standard+ slicing parameters mentioned above resulted in a print time of approximately 5 hours and 45 minutes.

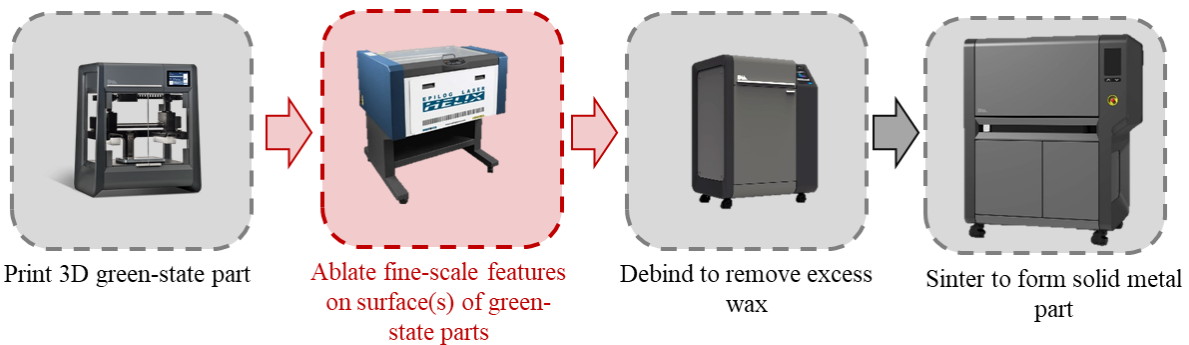


Figure 53. Manufacturing workflow showing BMD process steps (gray backgrounds) and the introduced laser ablation step (red background).

Although default Standard+ slicing parameters were utilized for the as-manufactured parts, Fabricate is capable of slicing at higher resolutions via Fabricate’s Ultra Fine+ slicing profile. Utilizing a 250- $\mu$ m-diameter nozzle and a 0.10-mm layer thickness, the default Ultra Fine+ slicing profile results in an estimated 14 hours and 17 minute print time, which was 148% longer than the approximate print time for the default Standard+ slicing parameters. Altering the Ultra Fine+ profile to utilize the minimum



0.05-mm layer thickness resulted in an estimated 24 hours and 1 minute print time, which was 318% longer than the approximate Standard+ print time. Although finer resolution capabilities were used, the 318% greater print time highlights the tradeoff between print resolution and print time.

The four specimens were then ablated in the green state via a 60-watt CO<sub>2</sub> Epilog Helix laser [75]. The power output from the laser can be adjusted from 0.6 watts to 60 watts in 0.6-watt increments. For this work, laser power was set to either 15 or 45 watts, *i.e.*, 25% or 75%, respectively, of full output power. The laser was configured to autofocus on the first treatment on a given specimen and then turned off for the second through eighth treatments on a given specimen. The autofocus procedure involves a contact probe to set the standoff distance. As the part remained stationary between treatments, subsequent focusing was deemed unnecessary. All treatments utilized the raster mode, meaning the laser pulsed on and off as the laser's carriage swept over the specimen. Adjustable in increments of 1%, the laser speed was set to 50% or 100%. Laser resolution was set to either 600 or 1200 dots per inch (dpi), and the laser made either 1 or 3 passes. In raster mode with a 600 or 1200 dpi resolution, the laser will attempt to ablate patterned regions as thin as 0.127 mm. Integrated into the Helix laser machine, a 1/8-hp air compressor directed approximately 1.6 ft<sup>3</sup>/min of air flow over the workpiece to cool the point of ablation and dilute any combustible materials directly around the laser point.

Within a patterned region, the laser pulsed on and off as the carriage traveled, creating a multitude of ablated circular spots. At low resolutions, the ablated spots overlapped only slightly. For increasing resolutions, the center-to-center spacing between adjacent ablated spots decreased, causing increased overlapping of spots. Hence, resolution as well as speed and power affect the total energy, or fluence, imparted within a patterned region [75].

Figure 54 shows a composite ablation pattern for Treatments 1-8 for Specimen 1. In Figure 54, the black-colored regions indicate patterned regions to be ablated, and the gray-colored regions indicate

regions to remain non-ablated. Each treatment’s ablation pattern contains three features: (1) an Arabic number uniquely identifying the treatment number, (2) a 5.95-mm diameter circle, and (3) a 1.19-mm wide by 35.72-mm long rectangle. Arabic numbers were approximately 3.18-mm tall and had line widths of approximately 0.3 mm. Similar to overall specimen dimensions, ablation patterns were expected to shrink during sintering, resulting in an anticipated 5.00-mm diameter circle and an anticipated 1.00-mm-wide by a 30.00-mm-long rectangle. As each treatment utilized different ablation processing parameters, each specimen was ablated eight times, once for each treatment’s ablation pattern. After all but the eighth ablation treatment, each specimen remained stationary within the Epilog Helix laser machine to maintain the specimen’s position with respect to the laser.

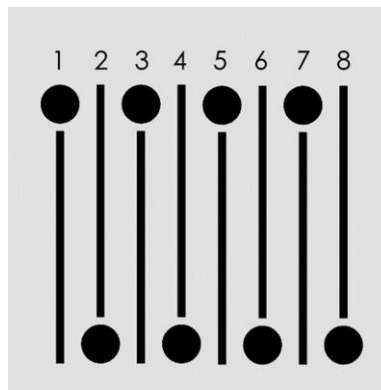


Figure 54. Composite ablation pattern for Specimen 1 showing the eight ablation patterns for Treatments 1-8. Ablation patterns for Specimens 2, 3, and 4 are similar except that the ablated numbers at the top of the pattern are 9 through 16, 17 through 24, and 25 through 32, respectively. Each composite ablation pattern has overall dimensions of 59.54 mm × 59.54 mm.

As shown in Figure 55, ablation patterns were oriented either (a) perpendicular or (b) parallel to the laser’s raster direction. Starting at the top-left of each sub-figure, the laser beam (thick solid red line) was emitted from the laser source before being reflected off the mirror (blue) and focused to the surface of the specimen (gray) via the focusing lens (black). The mirror and the focusing lens were

located on the carriage (not shown), which rapidly translated parallel to the  $y$ -direction to ablate a single raster. After completing a raster, the carriage translated a small distance in the positive  $x$ -direction before completing another raster. In this manner, alternating rasters were completed in the positive and negative  $y$ -directions. Specimens 1 and 3 were ablated with the major axes of the to-be-ablated rectangles perpendicular to the laser's raster direction (cf. Figure 55a). Specimens 2 and 4 were ablated with the major axes of the to-be-ablated rectangles parallel to the laser's raster direction (cf. Figure 55b). For all treatments, the laser beam was perpendicular to the to-be-ablated surface. *i.e.*, the laser beam was parallel to the  $z$ -direction as shown in Figure 55.

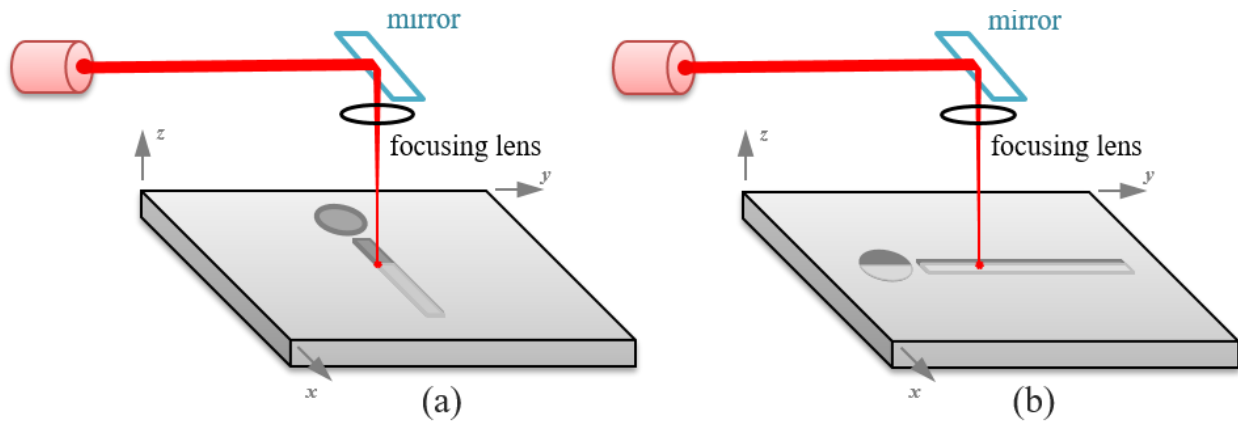


Figure 55. Schematic showing ablation pattern relative to the laser rastering direction for (a) perpendicular and (b) parallel orientations.

The time to ablate the eight treatments on a given specimen was between 5 and 36 minutes. If a single set of processing parameters had been used for a specimen's composite ablation pattern, the ablation time would have decreased to approximately 0.5 to 9 minutes. Ablation time was primarily influenced by two parameters, ablation resolution and pattern orientation. First, ablation resolution influenced

ablation time with the print time approximately doubling as the ablation resolution doubled from 600 to 1200 dpi. Second, pattern orientation increased ablation time from 14 seconds for a single pass in a parallel orientation to 1.5 minutes for a single pass in the perpendicular orientation.

After ablation, specimens were debound and sintered in accordance with Desktop Metal guidelines (cf. [23]). As described below in Section 2.2, a Design of Experiments (DOE) was utilized to determine the overall experimental strategy. Lastly, characterization utilized a VHX-7000 digital microscope as described in Section 2.3.

#### 4.2.2: Design of Experiments

A five-factor two-level, *i.e.*,  $2^5$ , full factorial DOE was executed using the laser ablation factors and levels shown in Table 5. Laser ablation factors and levels. The selected factors address laser ablation, not BMD, process parameters. Values for low and high levels were determined based upon qualitative experimentation prior to conducting the design of experiments. Factors and levels were randomized and blocked according to the direction of laser travel by Minitab 19 [52] to create the sequence of treatments.

Table 5. Laser ablation factors and levels.

Factor	Symbol	Units	Low level	High level
# of laser passes	$n$	--	1	3
Laser power	$p$	%	25	75
Laser speed	$s$	%	50	100
Direction of laser travel	$d$	--	Perpendicular	Parallel
Laser resolution	$r$	dpi	600	1200

Response surfaces for four responses – average ablation depth  $D$ , ablated surface roughness  $S_q$ , and the angle between ablated and non-ablated surfaces  $\Theta$ , and width at the bottom of the rectangular ablated region – were calculated in Minitab 19 [52] assuming an incomplete  $2^{\text{nd}}$  order model of the form

$$y = \beta_0 + \sum_{i=1}^n \beta_i x_i + \sum_{j=1}^n \sum_{k=1}^n \beta_{j,k} x_j x_k + \epsilon \quad \forall j \neq k \quad (8)$$

where  $y$  is the response of interest;  $\beta_0$ ,  $\beta_i$ , and  $\beta_{j,k}$  are the regression coefficients;  $x_i$ ,  $x_j$ , and  $x_k$  are factors;  $n = 5$  is the number of factors; and  $\epsilon$  is the error term. The exclusion of center points from the DOE means that quadratic terms of a single factor were undeterminable. Statistically significant hierarchical response surfaces for each of the three responses were then calculated via backward elimination [76]. Backward elimination consists of two iterative steps. In Step 1, regression coefficients and  $p$ -values for the regression coefficients were calculated using the model in Eqn. (8). In Step 2,  $p$ -values for the regression coefficients were compared to the assumed  $\alpha = 0.05$  significance level. If all  $p$ -values were less than the assumed  $\alpha = 0.05$  significance level, iteration ceased resulting in a model in which all terms were statistically significant. However, if any  $p$ -value for any regression coefficient was greater than the assumed  $\alpha = 0.05$  significance level, the factor or two-factor interaction corresponding to the regression coefficient having the greatest  $p$ -value was removed from the model, resulting in a new reduced model for Step 1. The two steps of backward elimination were iterated until only statistically significant hierarchical terms remained.

### 4.2.3: Measurement System

A Keyence VHX-7000 digital microscope was utilized to obtain optical and topological images, depth measurements, surface roughnesses, angles between ablated and non-ablated surfaces, and widths at the bottom of the ablated rectangles. Imaging and measurements were possible due to the microscope's depth composition capabilities in which a sequence of images were captured at multiple heights above a specimen. The sequenced images were then digitally combined to create a composite image showing the most in-focus features across the range of considered heights.

The digital microscope utilizes a VHX-E100 high-resolution objective lens, which at 100X magnification captures a 3.05 mm by 2.28 mm image. Using the High-resolution (4K Mode OFF) mode, the microscope's VHX-7100 fully integrated head digitizes 2880 pixels by 2160 pixels, resulting in an in-plane resolution of 1.1  $\mu\text{m}$  per pixel [77]. The microscope's 1- $\mu\text{m}$  out-of-plane resolution is independent of magnification [77].

#### 4.2.3.1: Average Ablation Depth, $D$

From the scanned and stitched images, the average ablation depth,  $D$ , was calculated by measuring the average ablated depth from a non-ablated region to an ablated region along the ablated rectangle's major axis. As shown in Figure 56, the average ablated depth along the centerline,  $\underline{d}_c$ , equals the average depth from a line located on a non-ablated surface (yellow line) to a line located in the ablated region (cyan line). The yellow line was placed on the non-ablated surface sufficiently distant to avoid any heat affected zone. Depth calculations were performed in the VHX-7000 microscope's VHX-H5M measurement software package [77].

Recognizing that the rectangle may or may not have a uniform depth across the rectangle's minor axis, average depths near the top and bottom of each rectangular region,  $\underline{d}_t$  and  $\underline{d}_b$ , were calculated. The average ablated depth for a treatment was calculated as  $D = \frac{1}{3}(\underline{d}_t + \underline{d}_c + \underline{d}_b)$ .

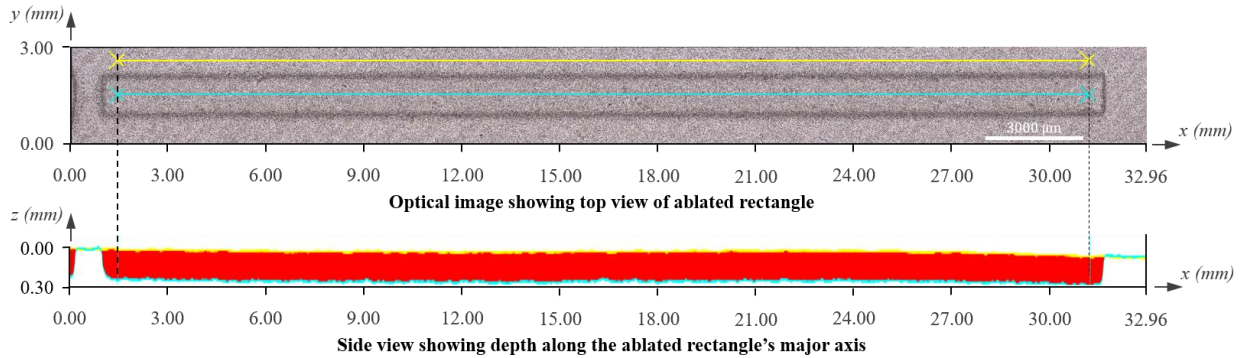


Figure 56. Optical image showing the top view of the ablated rectangle (top) and a side view showing depth along the ablated rectangle's major axis (bottom) for Treatment 1. The yellow line indicates the measured non-ablated height, and the cyan line indicates the measured ablated height.

#### 4.2.3.2: Surface Roughness of Ablated Regions, $S_q$

Starting from the scanned and stitched images, surface roughness measurements were calculated via VHX-7000's measurement software within a 4.0-mm-diameter circular region of each treatment's as-sintered 5.0-mm-diameter ablated circle. Figure 57 shows the centered positioning of the surface roughness measurement region (filled red circle) within the 5.0-mm-diameter ablated region for Treatment 10. Edge effects were mitigated by including a 0.5-mm radial buffer between the measured region and the ablated region.

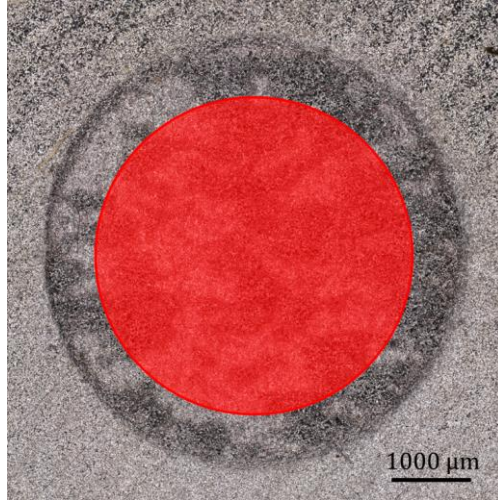


Figure 57. Positioning of the 4.0-mm-diameter surface roughness measurement region (red circle) within the 5.0-mm-diameter circular ablated region for Treatment 10.

Surface roughness was calculated as the root mean square of height at each point in the selected region using

$$S_q = \sqrt{\frac{1}{A} \int \int_A z^2(x, y) dx dy} \quad (9)$$

where  $A$  is the area of the region of interest and  $z$  is the measured height as a function of  $x$  and  $y$  coordinates. The root mean square of height is equivalent to a standard deviation of height [78].

#### 4.2.3.3: Angle Between Ablated and Non-Ablated Surfaces, $\theta$

The angle between ablated and non-ablated surfaces  $\theta$  was measured by imaging and saving topology images of each treatment's rectangular ablated region in the as-sintered state. Saved images were then analyzed in the VHX-7000's VHX-H5M software to determine the maximum angle between ablated and non-ablated surfaces on the two 30-mm-long sides of the rectangular ablated region. An average cross



section of the rectangular ablated region was created from 23 individual profiles taken at 0.5-mm intervals along the ablated rectangle's 30-mm-long direction to measure an 11-mm long region in the middle of the profile. Figure 58 shows the average cross section for Treatment 1 annotated with VHX-7000 measurements of the 54.0° and 53.2° maximum angles on the left and right side, respectively, of the average cross section.

The average angle  $\theta$  is the average of the maximum angles on the left and right side of the cross section. Accordingly, the average angle is the average of 46 individual measurements per treatment. The difference in maximum ablation angle from the left to the right side of the cross section  $\Delta\theta$  equals the absolute value of the maximum angles on the left and right side of the average cross section. Referring to Figure 58, the average angle  $\theta$  for Treatment 1 is 53.6°, and the difference in angles  $\Delta\theta$  for Treatment 10 is 0.8°.

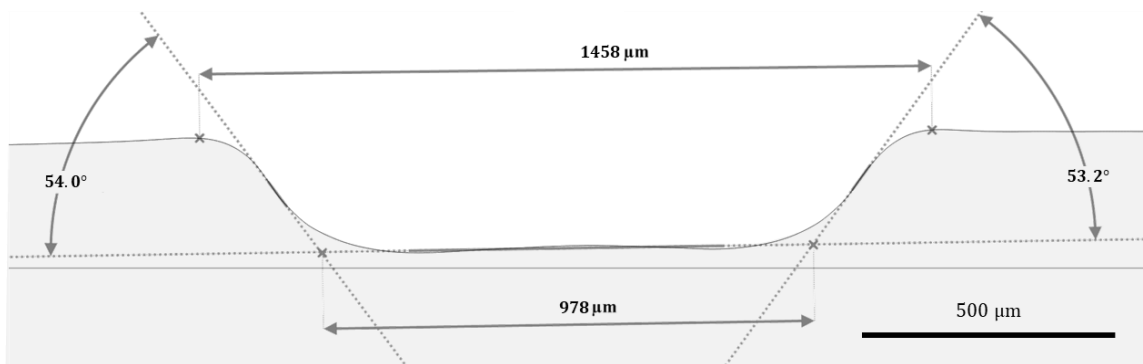


Figure 58. Cross section profile of the rectangular ablated region for Treatment 1, averaged over an 11.00-mm region in the channel middle for treatment 1 in the sintered state. The gray-colored region was added to indicate non-ablated material; hence, the gray coloring fails to show actual non-ablated microstructure, such as intra- and inter-bead porosity.

#### 4.2.3.4: Ablated Width, W

The ablated widths were measured from the same averaged profile as the angles. Width was measured at the top and bottom of the rectangular feature. The width at the top of the channel was measured from edge to edge by determining where a line lowered down on top of the profile would first intersect with the profile and measuring the shortest distance between two manually selected points. The width at the bottom of the channel was measured from the shortest distance between the intersection points between the lines created when measuring the angle on each side of the channel. For treatment 1, the width at the top of the channel was measured to be 1458  $\mu\text{m}$  and the width at the bottom of the channel was 978  $\mu\text{m}$ .

#### 4.3: Results

Each of the four printed specimens was ablated with eight treatments, resulting in a total of 32 treatments. Specimens were debound and sintered in the same batch to reduce the influence of variability during debinding and sintering processes. Optical images of the as-sintered specimens are shown in Figure 59.

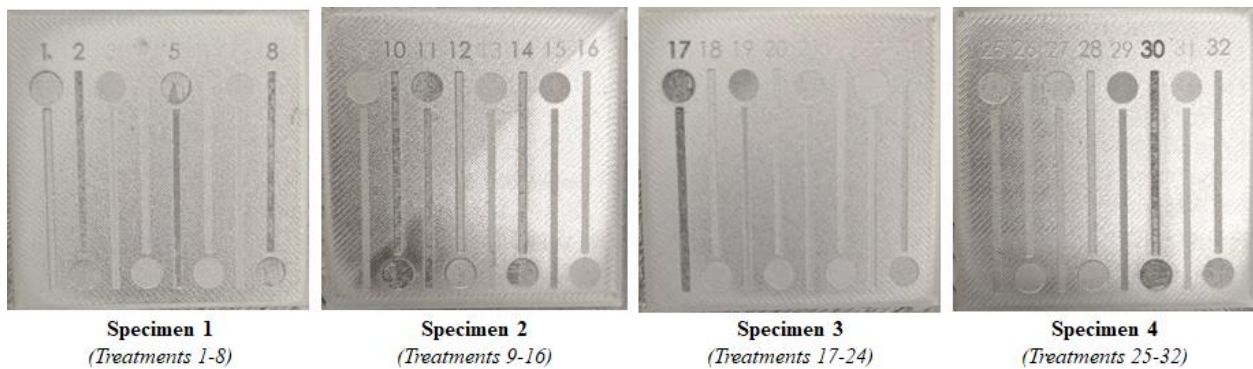


Figure 59. As-sintered Specimens 1 through 4 showing Treatments 1 through 32.

Figure 60 shows a qualitative comparison of channel topology for the mid-region of Treatments 1 through 8 on Specimen 1. The approximately 20-mm long region is highlighted by a blue-colored rectangle overlaid on the image of Specimen 1 in the top right-hand corner of Figure 60. The optical and topological images in Figure 60 are for the same surface.

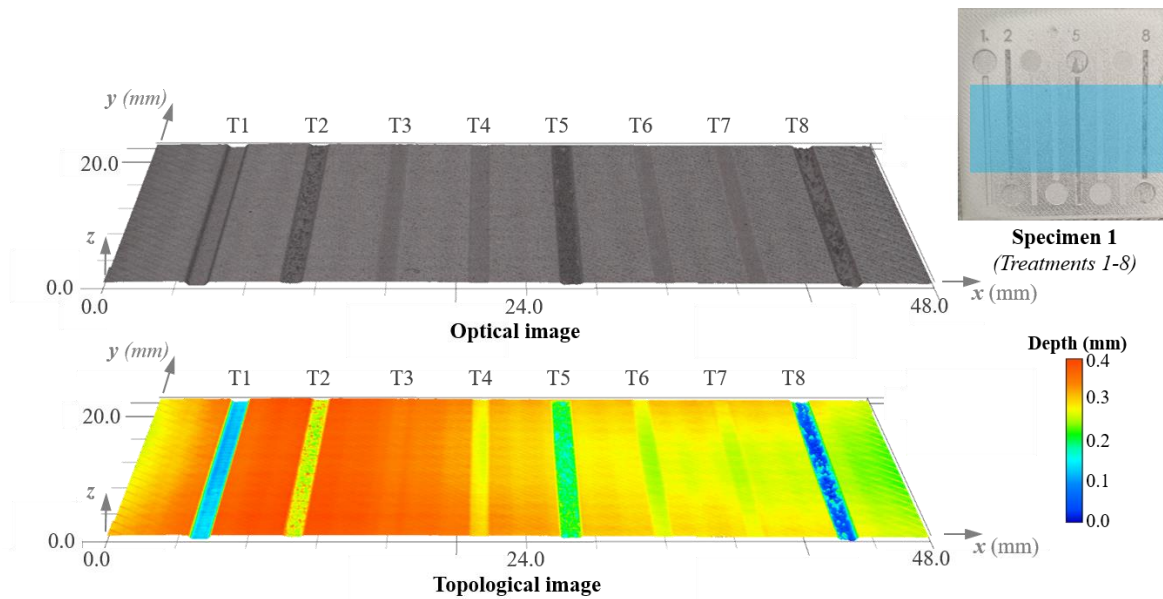


Figure 60. Optical (top) and topological (bottom) images showing a 20-mm-long region of channels for Treatments 1-8 (*i.e.*, Specimen 1). The approximate location of the imaged region is indicated by the blue-colored rectangle overlaid on Specimen 1 (cf. top right corner).

Table 6 shows the corresponding treatment number, factors, levels, and numerical results for all treatments. For example, Treatment 1 was subjected to 3 passes of a 75% power laser traveling at a 50 % speed perpendicular to the direction of the channel and having a 600 dpi resolution. The average depth in the as-sintered state of Treatment 1 was 229  $\mu\text{m}$ , the average depth / pass was 76  $\mu\text{m}$ , the surface roughness was 7.0  $\mu\text{m}$ , the average angle was 51.9°, and the difference in angles was 2.2°.

Table 6. Laser ablation treatment number, processing parameters, and as-sintered depth, roughness, and ablation angles.

T#	Passes #	Power %	Speed %	Laser direction	Resolution dpi	As-Sintered State						
						Avg Depth $\mu\text{m}$	Avg Depth / pass $\mu\text{m}$	StDev Depth $\mu\text{m}$	Roughness ( $S_q$ ) $\mu\text{m}$	Avg Angle deg	Angle Diff deg	Width bottom $\mu\text{m}$
1	3	75	50	Perp.	600	229	76	7	7.0	53.6	0.8	978
2	3	25	50	Perp.	1200	102	34	1	23.0	30.3	1.5	887
3	1	25	100	Perp.	1200	4	4	0	7.2	2.0	0.1	760
4	1	75	100	Perp.	600	31	31	2	11.8	11.5	1.8	855
5	1	75	50	Perp.	1200	88	88	4	13.5	28.6	0.3	1052
6	1	25	50	Perp.	600	17	17	0	8.6	7.0	0.9	877
7	3	25	100	Perp.	600	8	3	0	7.6	3.4	-0.1	729
8	3	75	100	Perp.	1200	115	38	6	12.2	33.3	2.5	997
9	1	25	100	Paral.	1200	15	15	3	3.7	9.3	2.8	1070
10	3	75	100	Paral.	1200	147	49	3	50.8	62.1	4.8	1085
11	3	25	50	Paral.	1200	85	28	7	24.7	55.1	7.0	1070
12	3	75	50	Paral.	600	183	61	2	17.6	65.5	-6.1	1059
13	1	25	50	Paral.	600	17	17	1	3.8	9.6	0.4	1078
14	1	75	50	Paral.	1200	122	122	2	15.9	47.6	10.7	1032
15	3	25	100	Paral.	600	9	3	1	6.3	9.6	-2.1	1097
16	1	75	100	Paral.	600	13	13	2	5.8	12.7	1.0	1031
17	3	75	50	Perp.	1200	81	27	5	73.6	50.7	6.0	1254
18	3	75	100	Perp.	600	114	38	0	15.5	34.8	1.9	926
19	3	25	100	Perp.	1200	12	4	1	10.7	6.4	-0.6	984
20	3	25	50	Perp.	600	56	19	4	16.5	17.1	2.5	795
21	1	25	50	Perp.	1200	36	36	1	6.0	9.4	2.6	798
22	1	25	100	Perp.	600	3	3	0	11.2	1.2	0.1	732
23	1	75	50	Perp.	600	67	67	2	6.0	19.9	2.1	941
24	1	75	100	Perp.	1200	63	63	2	6.2	17.7	0.6	831
25	1	75	100	Paral.	1200	64	64	4	8.1	27.1	8.6	1029
26	1	75	50	Paral.	600	56	56	1	12.5	24.8	5.2	1011
27	3	25	50	Paral.	600	52	17	1	7.4	38.4	1.3	1080
28	3	75	100	Paral.	600	81	27	2	15.7	47.3	13.1	1073
29	3	25	100	Paral.	1200	14	5	2	9.0	12.8	-0.1	1086
30	3	75	50	Paral.	1200	253	84	7	79.0	68.2	8.4	1077
31	1	25	100	Paral.	600	4	4	0	3.2	2.9	0.4	1107
32	1	25	50	Paral.	1200	22	22	1	9.9	16.4	0.8	1042

#### 4.3.1: Ablated Depth, D

As shown in Table 6, average ablated depths ranged from 3 to 253  $\mu\text{m}$ . Treatments 30, 1, and 12 – all employing 3 laser passes at 75% power and 50% speed – resulted in the three longest ablation depths of 253, 229, and 183  $\mu\text{m}$ , respectively. In contrast, treatments 22, 3, and 31 – all employing 1 laser pass at 25% power and 100% speed – resulted in the three shortest ablation depths of 3, 4, and 4  $\mu\text{m}$ , respectively. Dividing each treatment’s ablation depth by the number of passes results in ablated depths from 3 to 122  $\mu\text{m}$  / pass.

Assuming up to 2nd-order interaction terms within a regression model for the five factors, the regression equation for as-sintered ablated depth is

$$D = 63.8 - 3.49 d - 0.961 s + 0.367 p - 1.2 n + 0.599 pn \quad (10)$$

where  $D$  is the as-sintered depth in  $\mu\text{m}$ ,  $d$  is the direction of laser travel with perpendicular directions coded as 1 and parallel directions coded as 0,  $s$  is the laser speed in % (*i.e.*, coded as “50” for 50% power),  $p$  is the laser power in %, and  $n$  is the number of laser passes. The regression equation has an  $R^2 = 0.784$ . It is interesting that for the factors and levels considered, the resolution  $r$  was statistically insignificant at  $\alpha = 0.05$  in determining the ablated depth  $D$ .

Figure 61 shows the regressed average sintered depth as a function of measured as-sintered depth for all 32 treatments. Except for Treatments 1, 17, and 30, the regression equation predicts the depth within  $\pm 25 \mu\text{m}$ , as shown by the dashed lines in Figure 61.

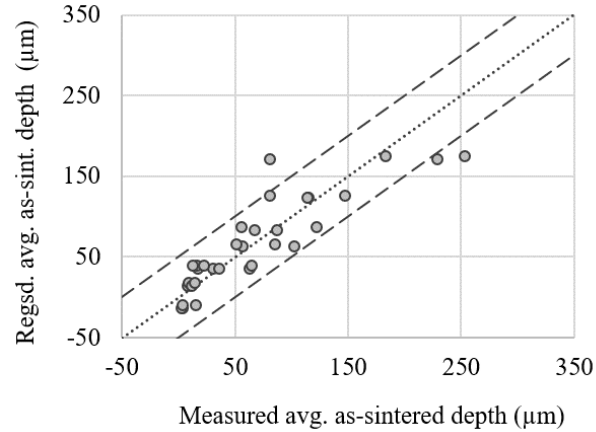


Figure 61. Regressed average as-sintered depth as a function of measured average as-sintered depth. Perfect correlation is indicated by the dotted line. The dashed line above and below the dotted line indicate +50 and -50 offsets, respectively.

#### 4.3.2: Surface Roughness, $S_q$

The regression equation for as-sintered surface roughness is

$$S_q = 22.6 - 1.15 d + 0.333 s - 0.625 p - 18.17 n - 0.00370 r - 0.000564 sr + 0.1747 pn + 0.000574 pr + 0.01892 nr \quad (10)$$

where  $S_q$  is the surface roughness in  $\mu\text{m}$ ,  $r$  is the laser resolution in dpi, and  $d$ ,  $s$ ,  $p$ , and  $n$  were previously defined, and. The  $R^2 = 0.7678$  for Eqn. (10). Figure 62 shows the regressed average sintered roughness as a function of measured as-sintered roughness for all 32 treatments. Except for Treatments 8, 17, and 30, regressed surface roughnesses were within  $\pm 12 \mu\text{m}$  of the measured surface roughnesses, as shown by the dashed lines in Figure 62.

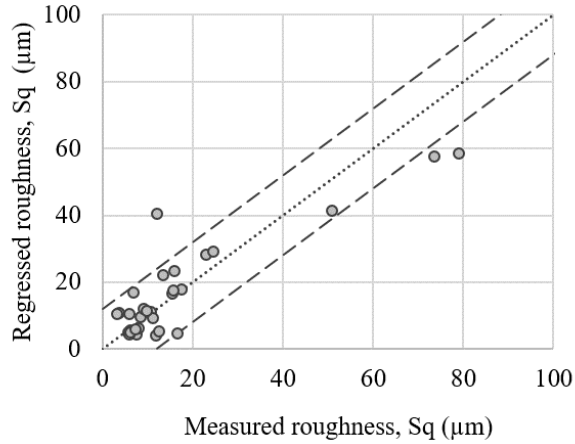


Figure 62. Regressed as-sintered roughness as a function of measured as-sintered roughness. Perfect correlation is indicated by the dotted line. The dashed line above and below the dotted line indicate +12 and -12 offsets, respectively.

#### 4.3.3: Average Angle Between Ablated and Non-Ablated Surfaces, $\theta$

The regression equation for the average as-sintered angle between ablated and non-ablated surfaces in the rectangular region is

$$\theta = -9.62 - 0.94 d - 0.0832 s + 0.1929 p + 12.27 n + 0.01227 r - 2.38 dn - 0.1135 sn + 0.1378 pn \quad (11)$$

where  $\theta$  is the average angle between ablated and non-ablated surfaces in degrees and  $d, s, p, n,$  and  $r$  were previously defined. The  $R^2 = 0.941$  for Eqn. (11). Figure 63 shows the regressed angle  $\theta$  as a function of measured angle  $\theta$  for all 32 treatments. Except for Treatments 10 and 11, all treatments were within  $\pm 15^\circ$  of the measured angle, as shown by the dashed lines in Figure 63. A maximum average angle  $\theta$  of  $68.2^\circ$  was measured for Treatment 30, having 3 passes at 75% power and 50% speed parallel to rectangular ablation pattern at a 1200 dpi resolution.

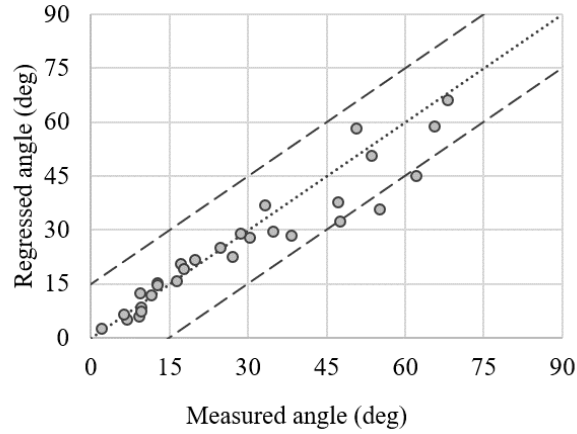


Figure 63. Regressed as-sintered angle as a function of measured as-sintered angle. Perfect correlation is indicated by the dotted line. The dashed line above and below the dotted line indicate +15 and -15 offsets, respectively.

#### 4.3.4: Ablated Width at Bottom of Rectangle, $W_b$

The regression equation for the as-sintered width at the bottom of the rectangular ablated region is

$$W_b = 989.6 - 164.9 d - 0.797 s + 1.299 p - 38.6 n - 0.0789 r - 1.121 ds + 1.878 dp + 0.0809 dr + 0.0751 nr \quad (12)$$

where  $W_b$  is the average width at the bottom of the rectangular ablated region in  $\mu\text{m}$  and  $d, s, p, n,$  and  $r$  were previously defined. The  $R^2 = 0.756$  for Eqn. (12). Figure 64 shows the regressed width  $W_b$  as a function of measured  $W_b$  for all 32 treatments. Except for Treatments 9, 15, and 31, Eqn. (12) predictions were within  $\pm 150 \mu\text{m}$  of the measured width, as shown by the dashed lines in Figure 64.



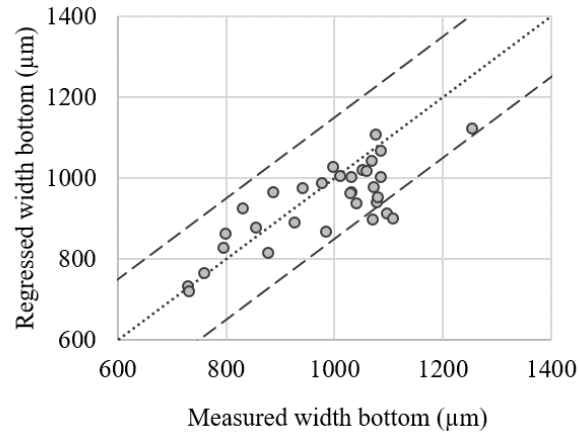


Figure 64. Regressed as-sintered width as a function of measured as-sintered width. Perfect correlation is indicated by the dotted line. The dashed line above and below the dotted line indicate +150 and -150  $\mu\text{m}$  offsets, respectively.

At its coarser 600-dpi resolution, the laser can spatially resolve  $42 \mu\text{m}$  during green-state ablation.

Assuming a 19.07% shrinkage, the spatial resolution in the as-sintered state is approximately  $35 \mu\text{m}$ .

Hence, it is relatively trivial to adjust a simple-shaped ablation pattern, such as a rectangle, to create a desired width.

For more complex ablation patterns, it is important to note that Eqn. (12) demonstrates directionality via ablation direction  $d$ . Specifically,  $W_b$  was on average  $164 \mu\text{m}$  wider for parallel ablation directions as compared to perpendicular ablation directions. The  $164\text{-}\mu\text{m}$  increase in width was statistically significant at  $\alpha = 0.05$  as determined by a two-sample t-test ( $p < 0.001$ ). Recalling that parallel ablation patterns require less processing time, it is likely that heat affected regions adjacent to vaporized regions have less time to dissipate heat. Hence, the finding that parallel ablation patterns result in wider widths suggests a temperature-dependent fluence ablation threshold and motivates the development of path-dependent numerical modeling.

### 4.3.5: D–S<sub>q</sub>–θ Response Space

Specific applications may require combinations of responses in the  $D$ – $S_q$ – $\theta$  space. For example, a mold for microfluidic applications may require controllable widths and depths, while maximizing angle and minimizing surface roughness [43]. The responses in the  $D$ – $S_q$ – $\theta$  space are shown in Figure 65, in which the (a), (b), and (c) subfigures show paired responses in the  $\theta$ – $S_q$ ,  $\theta$ – $D$ , and  $S_q$ – $D$  planes. In Figure 65b and Figure 65c, the ablated depth is normalized by the number of passes. A primary use of such

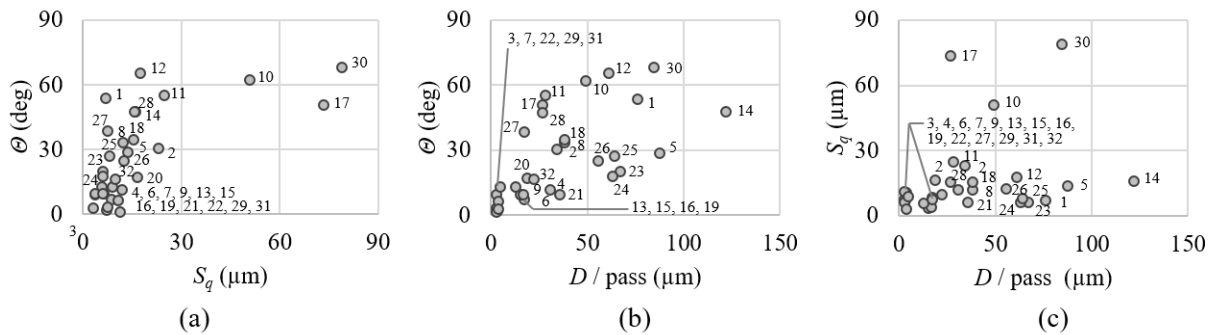


Figure 65.  $D$ – $S_q$ – $\theta$  response space showing the (a)  $\theta$ – $S_q$ , (b)  $\theta$ – $D$ , (c) and  $S_q$ – $D$  planes. Treatment number is indicated via a number adjacent to each point.

Whereas Figure 65 primarily serves as a useful design tool identifying feasible response combinations, additional insights are available via such representations. For example, Figure 65a indicates a non-linear relationship between ablation angle  $\theta$  and surface roughness with ablation angles limited to less than  $70^\circ$  regardless of surface roughness. Just as interesting, Figure 65c suggests that the ablation depth  $D / \text{pass}$  may be increased from 3 to  $122 \mu\text{m} / \text{pass}$  while maintaining a surface roughness  $S_q \leq 30 \mu\text{m}$ .

#### 4.4: Discussion

Compared to the BMD manufacturing process, the demonstrated laser ablated BMD (laBMD) process embodies several advantages. First, the laBMD process resulted in finer feature depths than those possible with BMD. For example, 22 of the 32 treatments produced depths / pass < 42.17  $\mu\text{m}$  / layer, *i.e.*, the finest layer height possible in the as-sintered state for BMD. Second, the laBMD process produced fine-scale circular features having significantly finer in-plane features than possible via BMD. Because of the laser's in-plane resolution, this laBMD capability is anticipated to be extendable to more complex curvilinear features. Third, the laBMD process produces positive draft angles, which is critical in molding operations, such as molds to manufacture microfluidic assays via roll-to-roll manufacturing [79]. Fourth, the laBMD process was able to manufacture green state parts in approximately 6 hours, which was approximately 4 times faster than the 24 hours required to print hi-resolution green state parts.

Beyond the demonstrated advantages, laBMD is anticipated to offer additional advantages as compared to BMD. For example, laBMD is expected to be able to produce debossed features having green state widths as narrow as 127  $\mu\text{m}$  [75], which is 49% smaller than the 250  $\mu\text{m}$  green state channels possible via BMD. Second, it is anticipated that multiple ablation passes having different process settings can be combined to result in even greater control of ablation depth, surface finish, and angles between ablated and non-ablated surfaces.

Beyond the demonstrated process, laBMD has many natural extensions. For example, the demonstrated laBMD process could easily be extended to any powder metallurgy process in which green state parts exist. A non-exclusive list of similar manufacturing processes includes powder metallurgy, metal injection molding, and metal fused filament fabrication. It's also important to note that the described ablation of a previously manufactured green-state part represents only one possible way to incorporate laser ablation. For example, a being-printed green state part could be laser ablated

while the green state part is being formed (e.g., ablating a layer or a portion of a layer while printing a part within a DM printer). This exciting extension could result in fine-scale internal features within a part instead of the fine-scale surface features described within this paper. Another extension is to introduce a rotational degree of freedom to the laser beam, potentially allowing the manufacture of even greater angles between ablated and non-ablated surfaces.

Despite seeking an accurate and complete characterization of the effects of laser ablation on green state BMD parts, this work has at least two major limitations. First, this work only examined the effects of laser ablating 17-4 PH green state parts intended to be processed via solvent debind before sintering. Although Slocombe and Li [72] successfully ablated 3 different polymer-metallic composites, other BMD material systems may have different constituents, constituent volume fractions, and absorption and thermal properties that require more experimentation. Second, this work considers the ablation of relatively small regions at the top of 5.93-mm-thick green state parts. It is possible and likely that ablating large percentages of a relatively thin part may require additional geometric considerations. For example, ablating a large percentage of the surface area may either release residual stresses or induce thermal stresses within the green state part, resulting in warpage of the part. Reductions in green-state part thickness may exacerbate such effects.

## CHAPTER 5: MICROFLUIDICS APPLICATION OF LASER ABLATED BMD

One application of laBMD is producing a microfluidics mold for a roll-forming process [79]. One of the main problems plaguing microfluidics is scale. In Boutiette et al. [79], a roll-to-roll continuous casting process was developed. The mold mounted on the roller was processed using DurusWhite material 3D-printed with an Objet30 Desktop 3D Printer with a resolution of  $\pm 100 \mu\text{m}$ . This resolution was important to creating the geometry for the fine-length-scale requirements of the mold. The 3D printed part was then used to make a mold out of epoxy for a polydimethylsiloxane (PDMS) part, which would then be used for mounting to the roller. These molds would be slotted into a drum mold that has a cutout to put the part into and then a polymer resin material is applied in a thin layer over the mold.

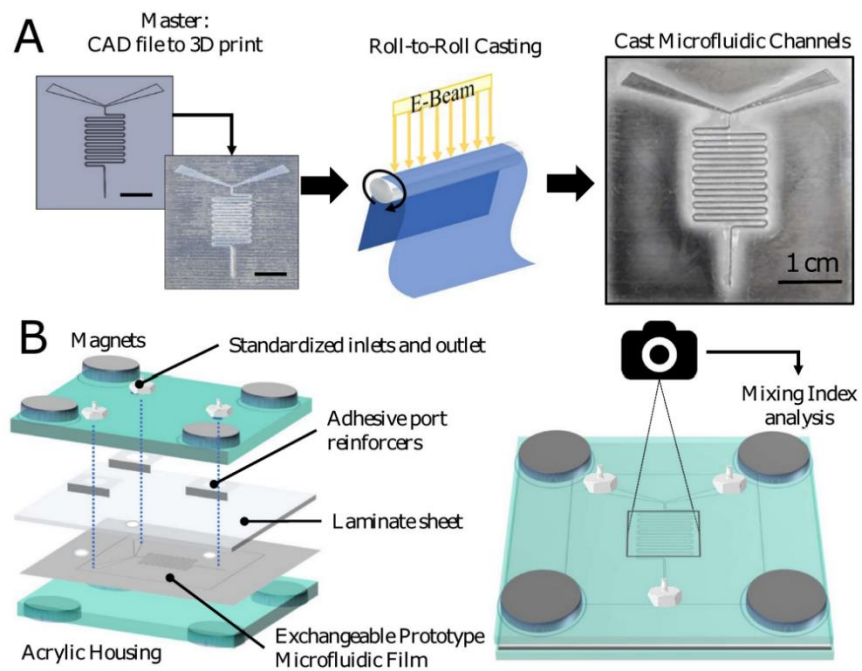


Figure 66. Major processing steps in a roll-to-roll forming process utilizing a polymer mold (Boutiette et al. [79])

The steps involved in creating the roll-mounted mold are many, which drives the need for streamlining the production process as well as searching for ways to improve the longevity of the molds. Using a metal mold would have better strength and hold up to repeated use over a long time. Combining BMD

and laser ablation, a method for producing microfluidics molds was conceptualized and deployed to manufacture cast films. The details of this application are in the remainder of this thesis section.

One possible method of manufacturing microfluidics molds is with a stamp-forming process. In this type of process, 3D printing could be used to produce two mold halves that deform a piece of sheet metal into the desired shape.

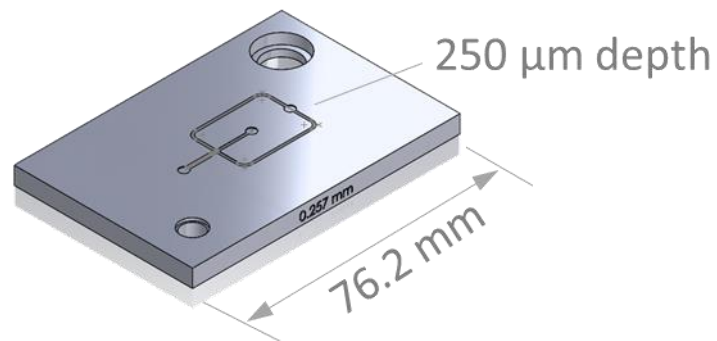


Figure 67. Half of the mold for the first design idea

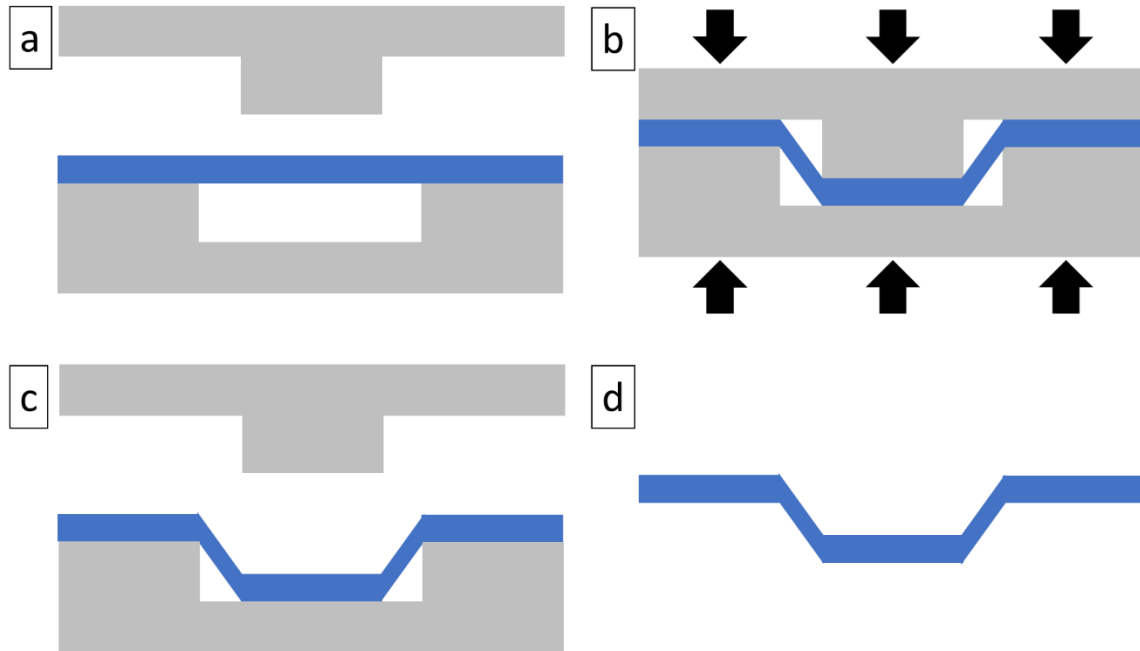


Figure 68. Schematic showing stamp forming process, with stamp parts in grey and the shim stock in blue, starting with the flat shim stock (a), then pressure is applied to the stamp halves, deforming the shim material (b), the stamp pressure is relieved (c), and the part is deformed (d)

The 3D printed mold halves could have the molding patterns directly printed into them or they could utilize laBMD to create the mold patterns. This process could be beneficial for mass producing metal molds if a large amount of identical molds are required. However, some challenges for this process are the requirement of additional assembly items such as locating pins and an industrial press to use it. Instead of stamp forming the molds, the molds themselves could be produced via laBMD. This would eliminate a processing step compared to the stamp forming process. The direct production of molds via laBMD was done to apply the findings of the laBMD study described in Chapter 4. The findings from the microfluidics application are detailed in the following sections.

### 5.1: Microfluidics Mold Design Parameters

The microfluidics mold design was initially created by considering the minimum bead size of the DM Studio System. Considering the limitations of the high-resolution nozzle and the ultra-fine print profile, the minimum bead size was as 0.250-mm wide by 0.050-mm tall. Incorporating a microfluidics path

pattern provided by Dr. Caitlin Howell of the University of Maine and the limitations of the DM Ultra Fine+ printing profile (e.g., minimum bead width, minimum bead height), the microfluidics pattern shown in Figure 69 was developed.

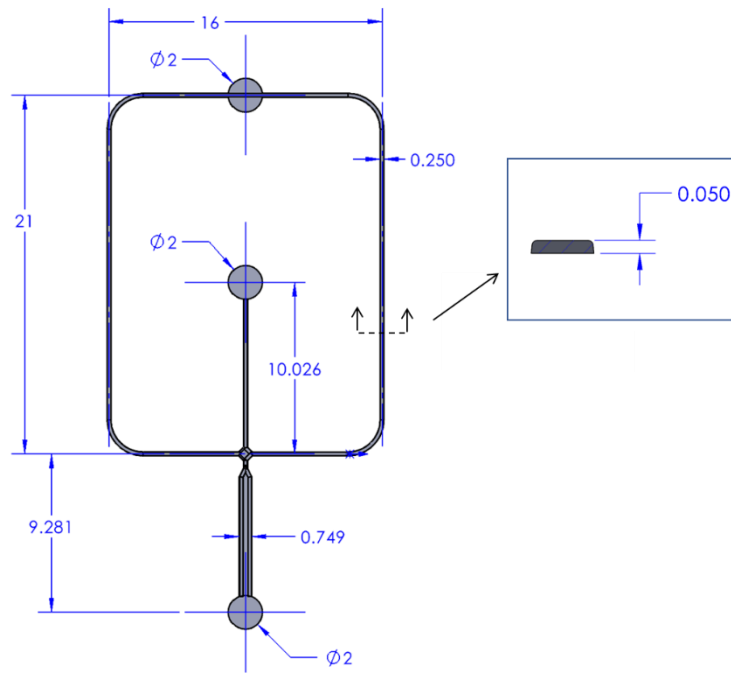


Figure 69. A sketch of the microfluidics pattern (gray with black outline) and dimensions (blue) in mm of the designed geometry (sintered geometry).

The major dimensions of the microfluidic blank are 50.8-mm height  $\times$  50.8-mm width  $\times$  0.635-mm thickness. Of note is the thickness (0.635-mm), as it was the maximum thickness allowable for the process as defined by operators of the roll forming process. Printing a part that thin is challenging, as BMD parts with small thicknesses are susceptible to high warpages as described in Chapter 2. Additionally, the microfluidics patterns have an embossed feature, which contrasts with the debossed features from the laBMD DOE described in Chapter 4. The additional heat required for ablating a larger surface area may result in greater thermo-mechanical effects, such as liquification of the surface material [80].



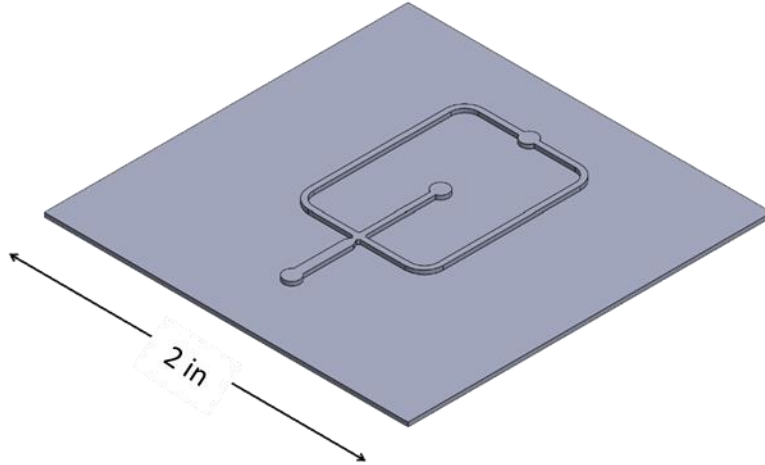


Figure 70. Desired microfluidics mold

To account for the shrinkage of the part as it went through the BMD process, a scale factor was applied within the SolidWorks [74] drawing. The scale factor corresponded to the sintering scale factor (SSF) in the XY plane for the material, 17-4PH stainless steel v1. As defined in Fabricate [11], the SSF value for 17-4PH v1 is 1.1907. To determine the size of a green state dimension, the sintering scale factor is multiplied the desired final, sintered dimension, like in Equation 13.

$$L_{green} = L_{sintered} * SSF_{17-4PHv1} \quad (13)$$

where  $L_{green}$  is some green state length,  $L_{sintered}$  is some sintered length, and  $SSF_{17-4PH}$  is the sintering scale factor of v1 17-4PH stainless steel.

## 5.2: Direct Laser Ablation of the Channel Pattern

The first try at ablation of the microfluidics pattern was by taking the microfluidics pattern with the as-designed dimensions and ablating that onto two BMD squares, one with 2.5 mm thickness and one with 0.328 mm thickness. The less thick part's 0.328-mm thickness was less than the 0.635-mm maximum thickness recommended by the roll-to-roll forming company. However, from previous experience with

BMD, it was expected that the thin part would experience much more warpage than the thicker part or possibly crack.

### 5.3: Study A, Thick Printed Parts

The first approach to producing the mold was to print the part thicker than the maximum thickness desired (0.635-mm), with the plan to reduce the thickness of the part with surface grinding. For this study, the part thickness was 2.5 mm and the material chosen was v1 17-4PH stainless steel for consistency between the DOE and the proof-of-concept application. Four Study A parts were printed with the designations A001, A002, A003, and A004. These parts followed the same manufacturing process as the laBMD study in Chapter 4, just with different geometry of the starting blank and of the pattern being ablated. A rendering of the 2.5 mm thick blank is shown in Figure 71.

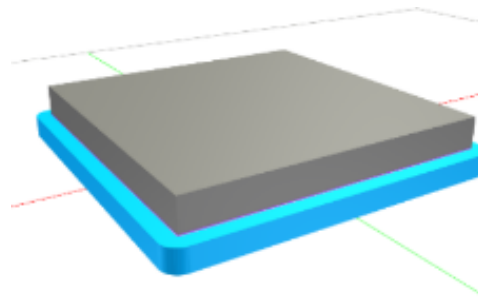


Figure 71. Fabricate rendering of Study A blank

The ablation parameters matched those used for treatment 1 in the laBMD study described in Chapter 4. Those parameters were chosen by looking at the  $\theta - S_q$  (angle and roughness) response space shown in Figure 72 to select parameters that would increase the sidewall angle and decrease the roughness. Those chosen ablation parameters were 45-watt laser power (75%), 50% speed, 3 passes, and 600 dpi.

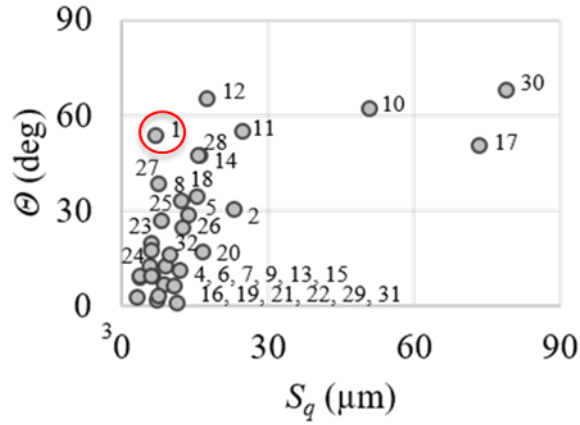


Figure 72. Angle  $\theta$  – surface roughness  $S_q$  response space highlighting  $\theta$ - $S_q$  response for Treatment 1.

Three variations of the microfluidics pattern were generated and applied to the parts in study A (see Figure 73). Pattern 1 was applied to parts A001 and A002, pattern 2 was applied to A003, and pattern 3 was applied to A004. For the three patterns, the major difference was in the widths of the thin and thick channel features. Another distinctive difference between the patterns in the margin area on pattern 2.

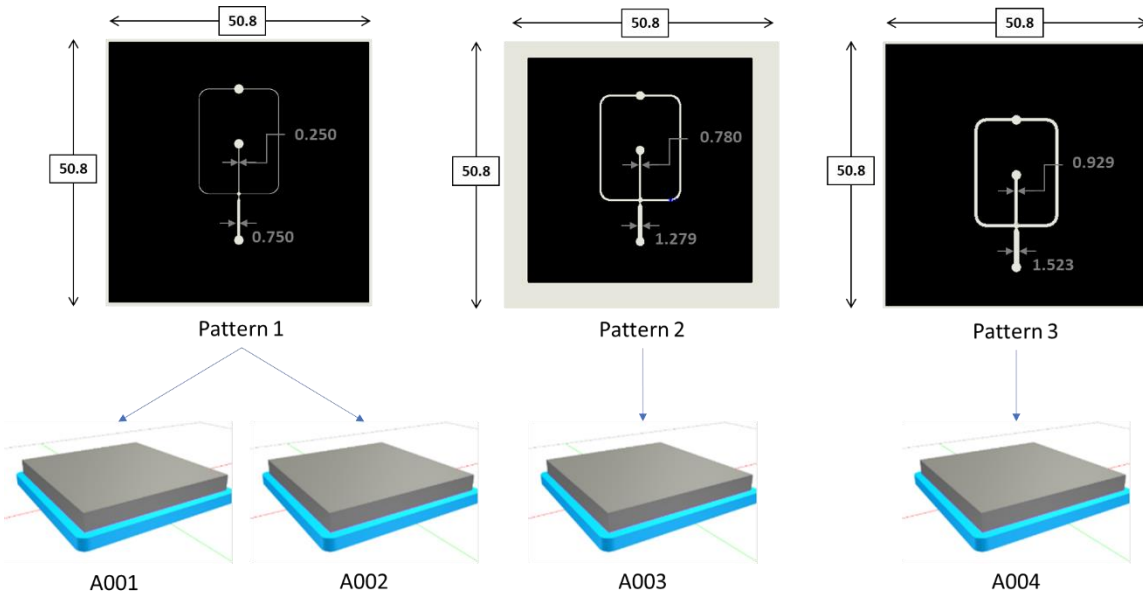


Figure 73. Study A laser pattern dimensions, all length units are in mm

Upon completion of sintering, the VHX-7000 was used to 3D scan the top surface that was treated with ablation. The scans were created in the same manner as the 3D scans to analyze the laBMD study in Chapter 4. Those 3D scans were used to create color deviation maps and extract angles, depths, and widths from the channels.

After the scans were complete, the as-sintered 2.50-mm thickness was reduced for treatment A003 only by surface grinding the non-ablated surface, i.e., the back side of the mold. Treatment A003 was selected because of its edge margin that would allow it to lay flatter on the magnetic fixture of the surface grinder. The surface grinding process involves successively removing material in small layer increments with a grinding wheel that makes passes over the part until a desired thickness is reached. An image of A003 towards the end of the surface grinding process is presented here in Figure 74.



Figure 74. Photo of A003 On surface grinding machine

As the part thickness got very thin, the part began to warp concave down, as seen in Figure 74. The warping of thin metal during surface grinding is a known issue among shop experts, who discuss how to address the problem and some of the causes, such as heat imparted to the material, in forums [81], [82].

In addition to the warping, there was also a nonconstant thickness imparted on A003. This can be observed by looking at the side view of the part in Figure 75, observing the color deviation map in Figure

76, and by seeing the thickness distribution from vernier caliper measurements (Figure 77 and Figure 78).

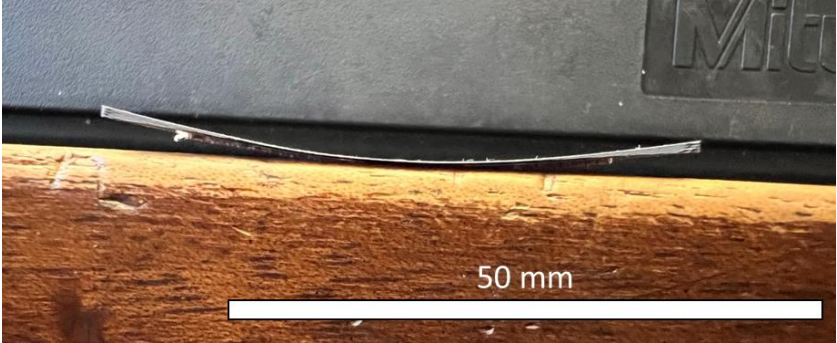


Figure 75. side view of A003 after surface grinding

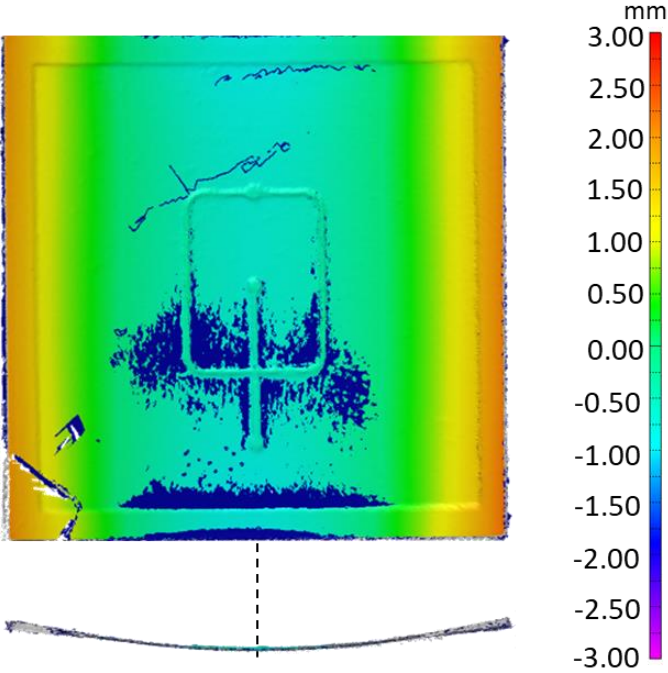


Figure 76. Deviation from flatness of A003 after surface grinding



Figure 77. Vernier micrometers with a cone tip placed on the ablated surface (shown) and a flat anvil on the non-ablated surface (not shown) measuring the thickness of A003.

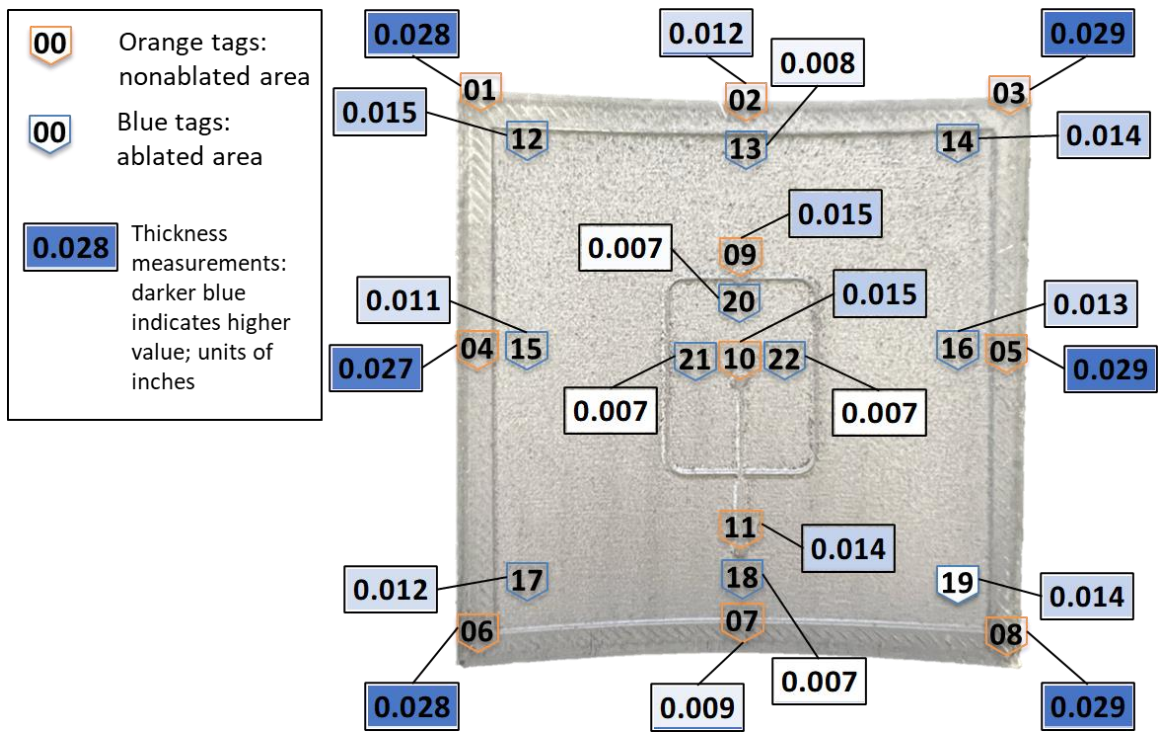


Figure 78. Thickness measurements of A003 using dial micrometers, units in inches

To avoid the warping that results in a nonconstant thickness, typically thin parts are flipped, and material is taken off both sides. This option was not available for this investigation because of the

presence of the microfluidics pattern on one side of the material. One potential solution is to employ the use of tape or other adhesive to keep the part flat during the machining process.

#### 5.4: Study B, Thin Printed Parts

The thin parts within Study B had as-sintered dimensions of  $50.8 \times 50.8 \times 0.328 \text{ mm}^3$ , so the as-printed dimensions would be  $60.488 \times 60.488 \times 0.389 \text{ mm}^3$ . In Study B, there was curiosity about whether laser ablation had a significant effect on the final as-sintered warpage of the part. To investigate this question, two identical thin blanks were printed, a rendering of one shown in Figure 79, and one remained unablated (B001) while the other was treated with laser ablation (B002).

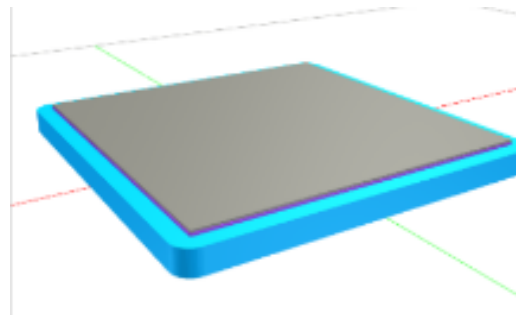


Figure 79. Fabricate rendering of Study B part

The ablation pattern for Study B, shown in Figure 80, was very similar to the one used for part A003, as the margin was found to be useful in reducing the amount of ablated area, which would help lessen the thermo-mechanical impact of the ablation process on the green-state part. Another difference is the widths of the parallel vs perpendicular features.

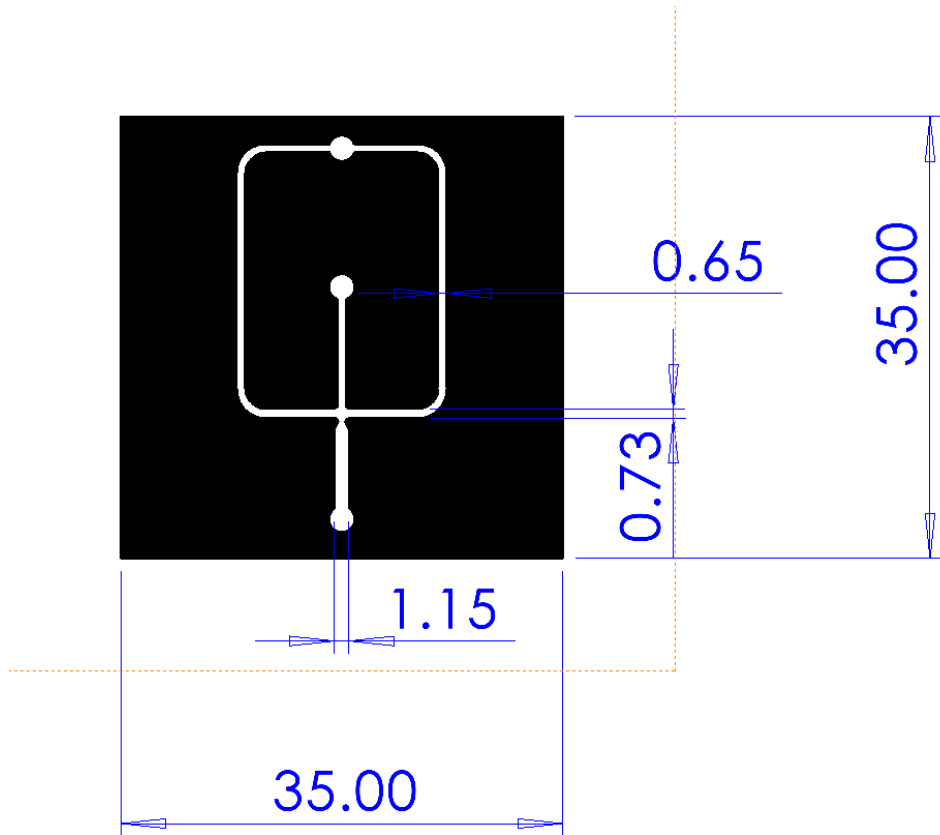


Figure 80. Ablation Pattern for B001, units of mm

After ablating B001, both B001 and B002 were debound and sintered following the normal BMD procedures. Figure 81 shows B001 on the setter plate after the sintering step.



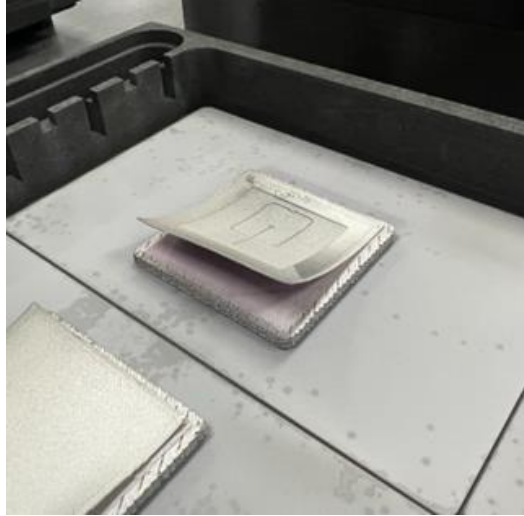


Figure 81. B001 as-sintered

As a comparison to the surface grinding process used on A003, the same set of vernier calipers was used to measure the thickness of B001 and those values are shown in Figure 82

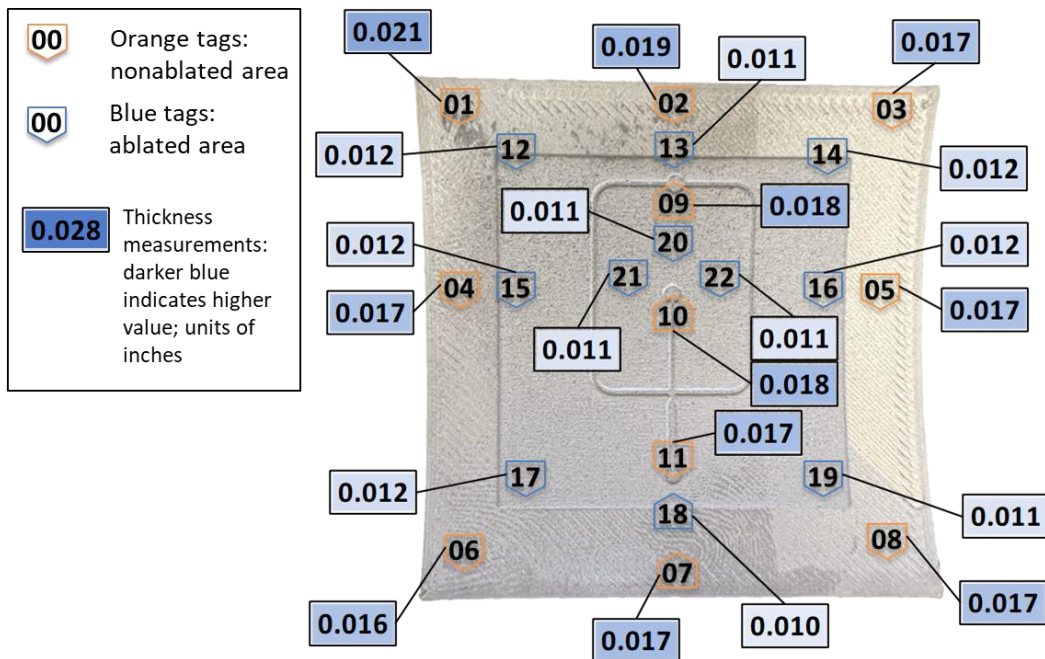


Figure 82. Thickness of B001 measured using dial micrometers, units of inches.

The Faro laser line probe [83] coupled with PolyWorks [84] was used to measure the deviation from flatness of the top surface of B001 after sintering (Figure 83). Comparing B001 to its unablated B002 counterpart, the warpage induced by sintering is approximately the same magnitude, indicating that the laser ablation did not have a significant impact on the as-sintered warpage of the thin (0.328 mm) part.

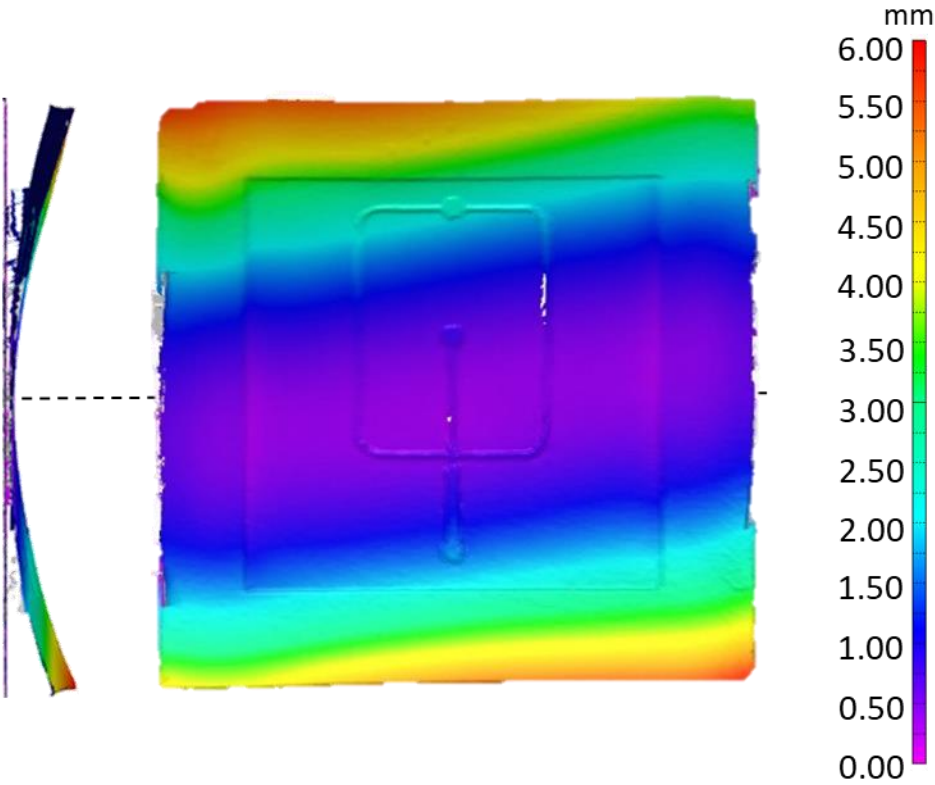


Figure 83. Deviation from flatness of ablated B001 as-sintered

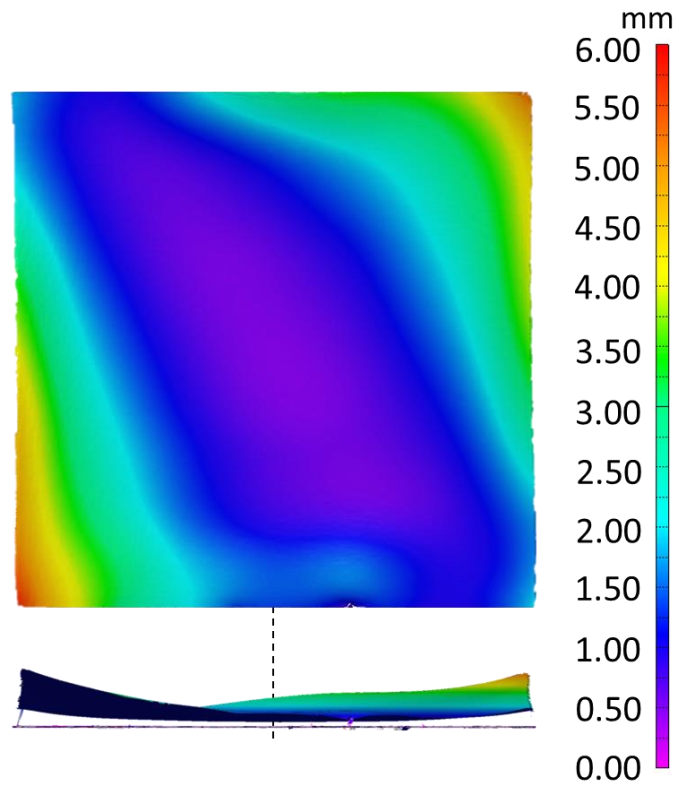


Figure 84. Deviation from flatness of unablated B002 as-sintered

### 5.5: Roll-to-Roll Casting Tests with BMD Molds

Two microfluidics molds – mold A003 from Study A (Figure 85), and mold B001 from Study B (Figure 86) – were sent to SAPPI North America in Westbrook, Maine for roll-to-roll casting trials. The trials produced thermopolymer microfluidic devices from both molds.

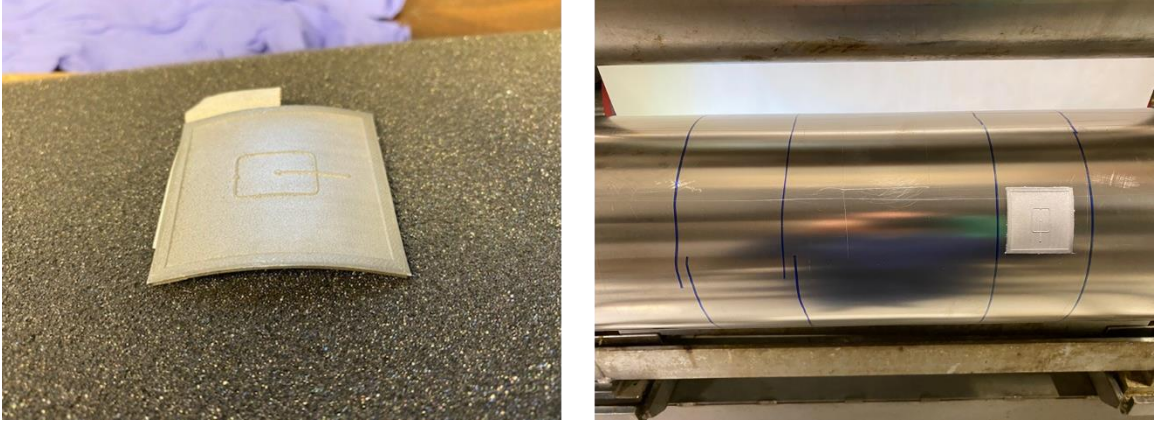


Figure 85. A003 on the left, deformed after being mounted on the roller, and on the right, mounted on the roller.

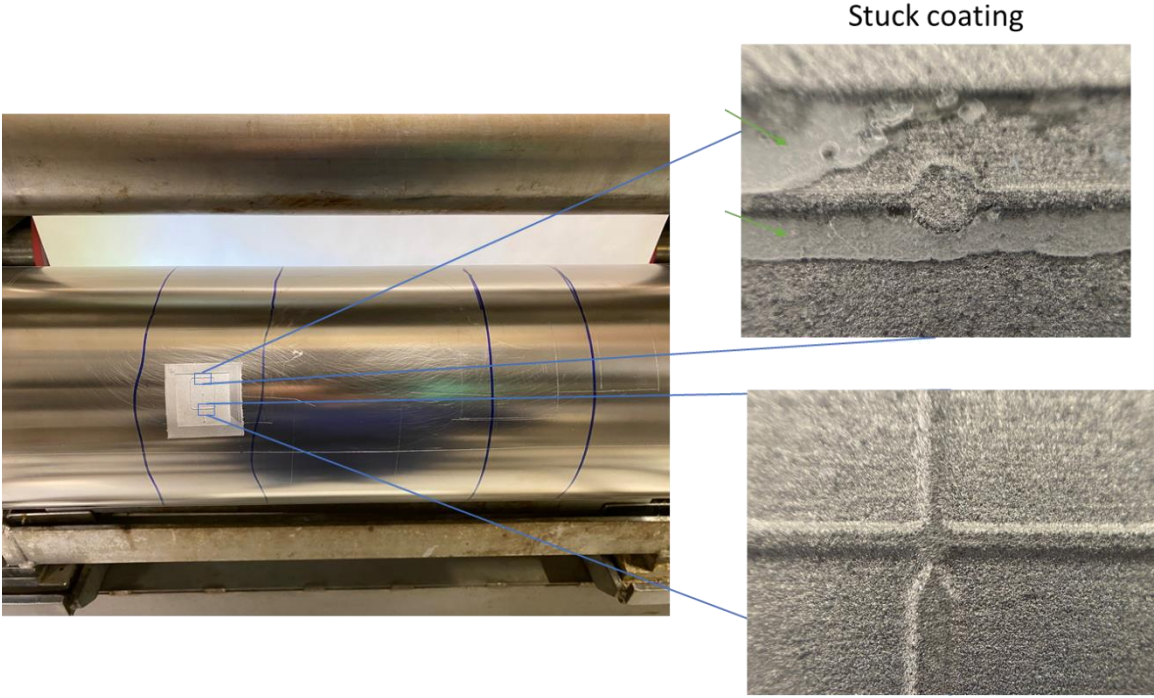


Figure 86. Close-up photos taken after mold use showing stuck coating at the top region of the pattern, while lower down, the pattern was free of stuck coating

Feedback from SAPPI personnel and visual inspection of the as-manufactured microfluidic devices suggests: (1) both A003 and B001 molds were able to be installed without issue, and (2) surface roughness is an opportunity for further improvement. In addition to influencing their microfluidic performance, rough molding surfaces increase the likelihood of polymer sticking to a mold during molding, which requires an operator to stop the trial and clean the mold with a wipe. Positive feedback was received on the draft angles being adequate to allow the polymer shims to release from the mold.

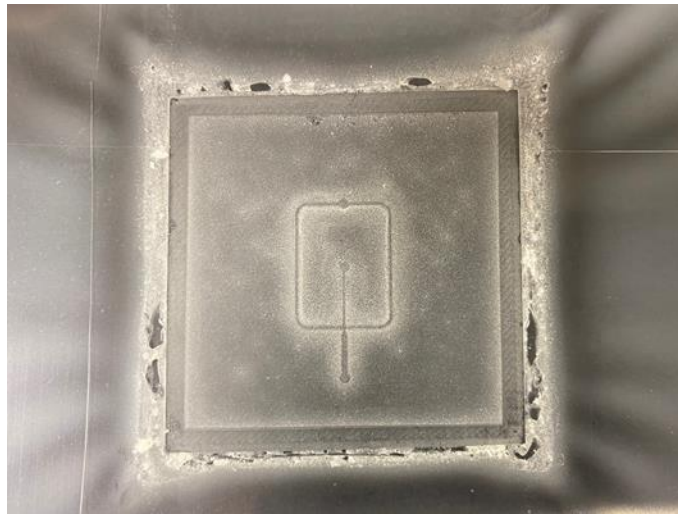


Figure 87. Device produced from roll-to-roll casting of A003

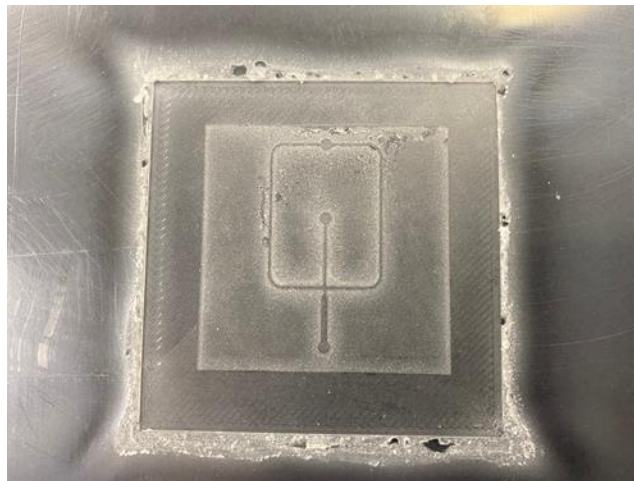


Figure 88. film produced from roll-to-roll casting of B001

## 5.6: Measurement of Profiles

To characterize the results from the microfluidics application, it was desired to compare the characteristics of the ablated pattern to the equivalent treatment from the laBMD study in Chapter 4. The key results analyzed were the depth of the ablated area and the angle between ablated and non-ablated regions and depth. The measurements were taken in the same manner outlined in section 4.2.3, with some slight modifications. The length of the area available to measure was shorter, so only 7 profiles spaced 0.5-mm apart were used to create a single averaged profile as seen in Figure 89.

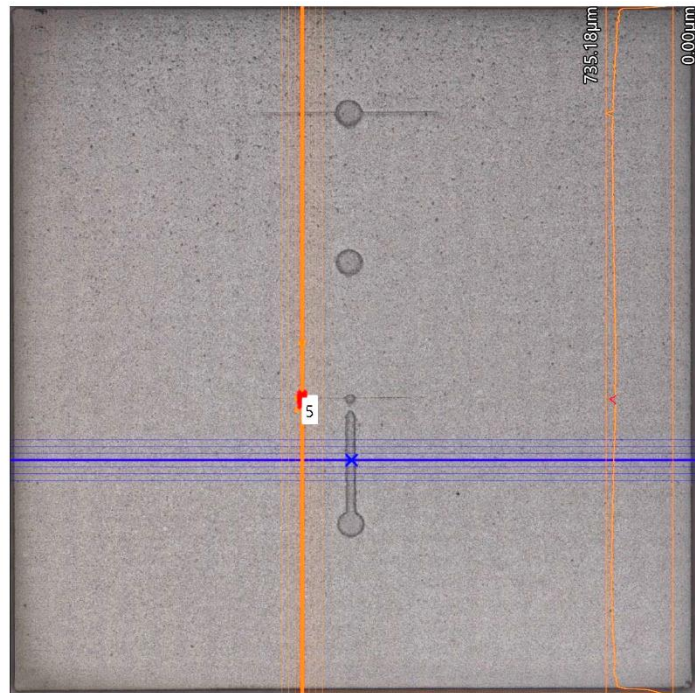


Figure 89. Two different profile measurement regions shown on specimen A001

The profiles were extracted in three different regions of the pattern, shown in Figure 90. There were two measurements of profiles that ran parallel to the gantry movement direction, the parallel left section, and the parallel right section. Additionally, there was one profile measured that ran

perpendicular to the gantry move direction. These profiles were chosen to measure because they were all designed to have the same thickness, so any differences between them would be process induced.

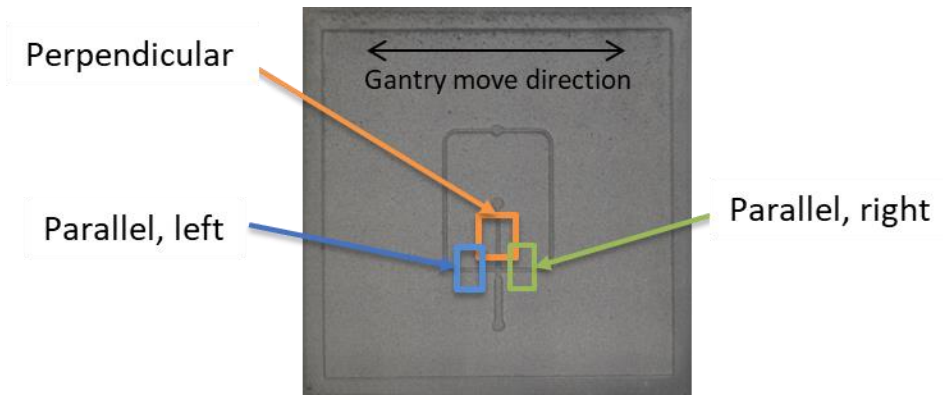


Figure 90. Regions of profile extractions for parts from study A

The measurements above were applied to three of the study A specimens in the sintered state, prior to any post processing. The only part that post processing would need to be considered for is A003, which is the only part that was treated with surface grinding to achieve a thickness reduction. The reason for only investigating study A specimens is because they are conducive to having their profiles extracted while they are still flat. Additional measures would need to be taken to measure the profiles in Study B, as the part B001 had significant curvature in the surface because of the sintering process.

## 5.7: Results

All the profile measurements shown below are for the parts after sintering and were created using the 3D measurement capabilities of the VHX-7000 microscope. A002 profiles are not reported due to shifting during the ablation process that uncharacteristically changed the effects of the laser process.

### 5.7.1: Color Deviation Maps

After sintering, color deviation maps for the ablated patterns were created for the study A parts. An important note to consider while viewing the color deviation maps of the as-sintered surfaces of the

Study A parts is that the color deviation maps do not have matching ranges on the scale bars, so color to color comparison from one color deviation map to the next must keep that in mind.

The color map for the ablated region in the sintered state for A001 is shown in Figure 91.

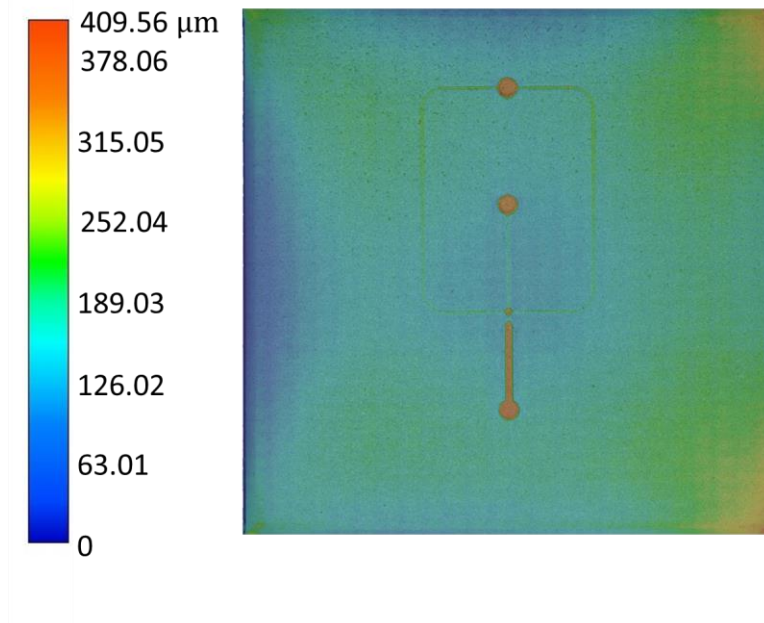


Figure 91. A001 color deviation of the ablated region after sintering

The color map for the ablated region in the sintered state for A002 is shown in Figure 92. It can be seen from inspecting the color deviation in the pattern that sometime between the repeating passes, the part shifted, and it caused the ablation to skew from its original destination. Because of this, it was decided to omit the cross-sectional measurements for A002 as they would not be characteristic of the parameters if they were applied correctly (without shifting).



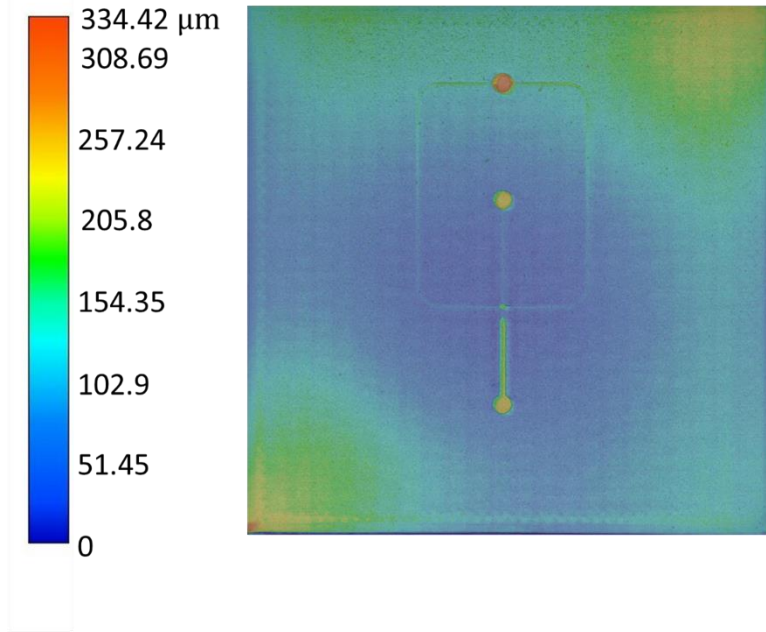


Figure 92. A002 color deviation of the ablated region after sintering

The color map for the ablated region in the sintered state for A003 is shown in Figure 93.

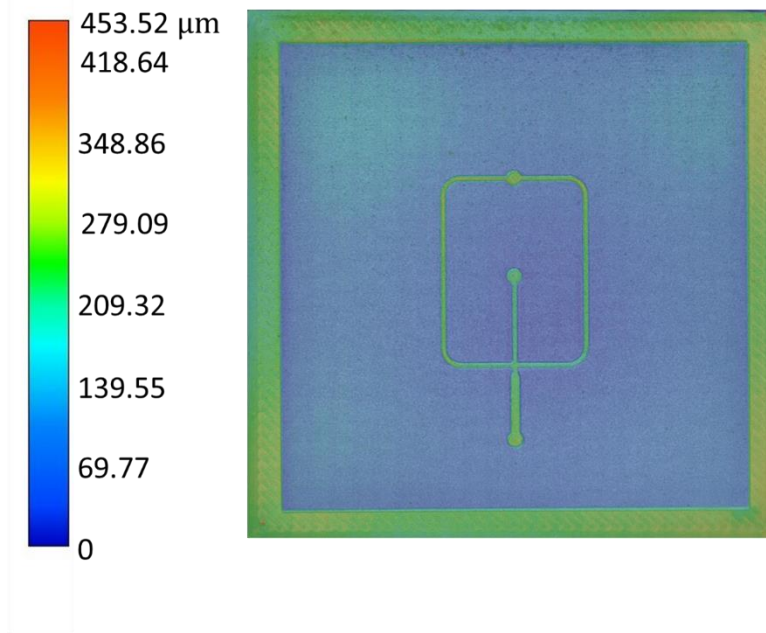


Figure 93. A003 color deviation of the ablated region after sintering

The color map for the ablated region in the sintered state for A004 is shown in Figure 94.

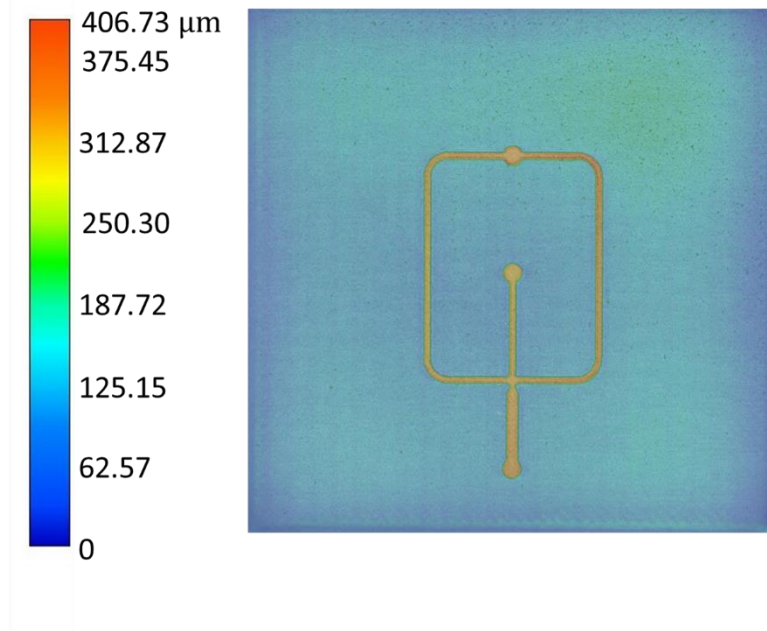


Figure 94. A004 color deviation of the ablated region after sintering

### 5.7.2: A001 Profiles

The perpendicular to gantry movement profile measurements for A001 are shown in Figure 95.

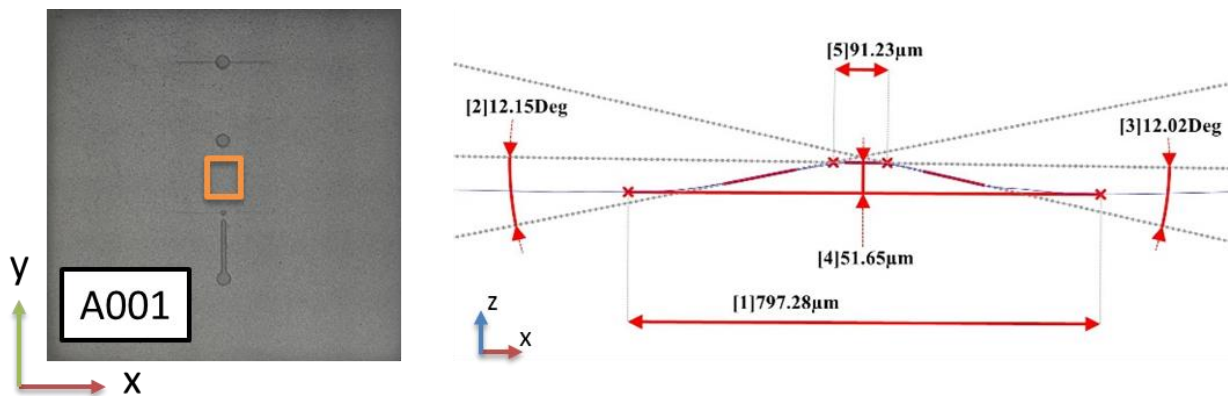


Figure 95. A001 perpendicular to gantry movement profile

The left side, parallel to gantry movement profile measurements for A001 are shown in Figure 96.

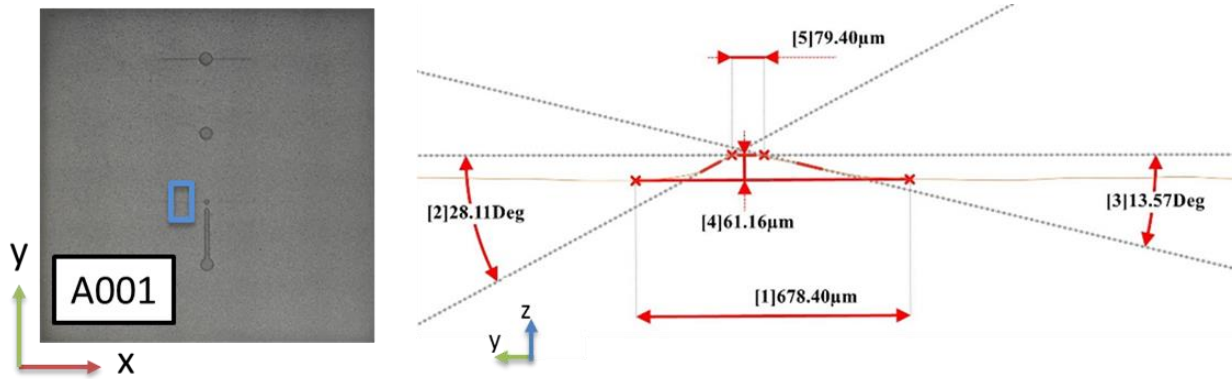


Figure 96. A001 left side, parallel to gantry movement profile

The right side, parallel to gantry movement profile measurements for A001 are shown in Figure 97.

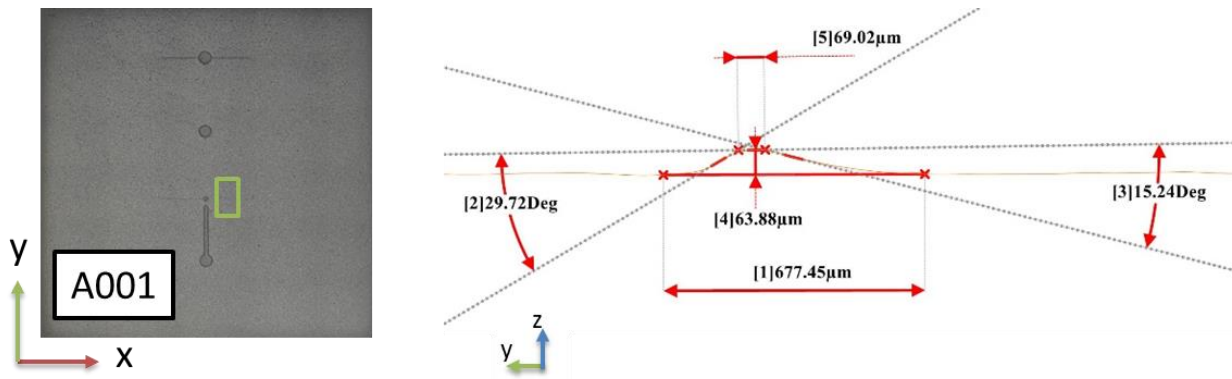


Figure 97. A001 right side, parallel to gantry movement profile

### 5.7.3: A003 Profiles

The perpendicular to gantry movement profile measurements for A003 are shown in Figure 98.

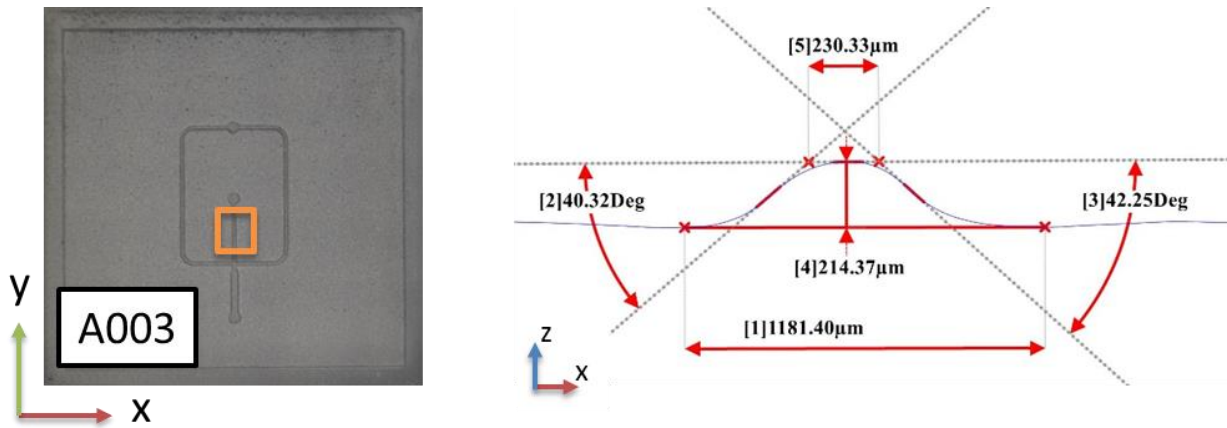


Figure 98. A003 perpendicular to gantry movement profile

The left, parallel to gantry movement profile measurements for A003 are shown in Figure 99.

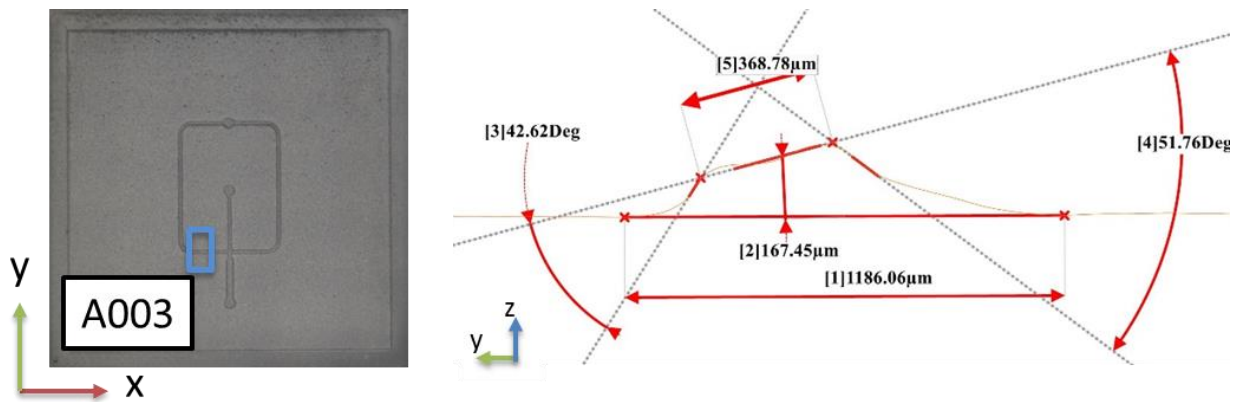


Figure 99. A003 left, parallel to gantry movement profile

The right, parallel to gantry movement profile measurements for A003 are shown in Figure 100.

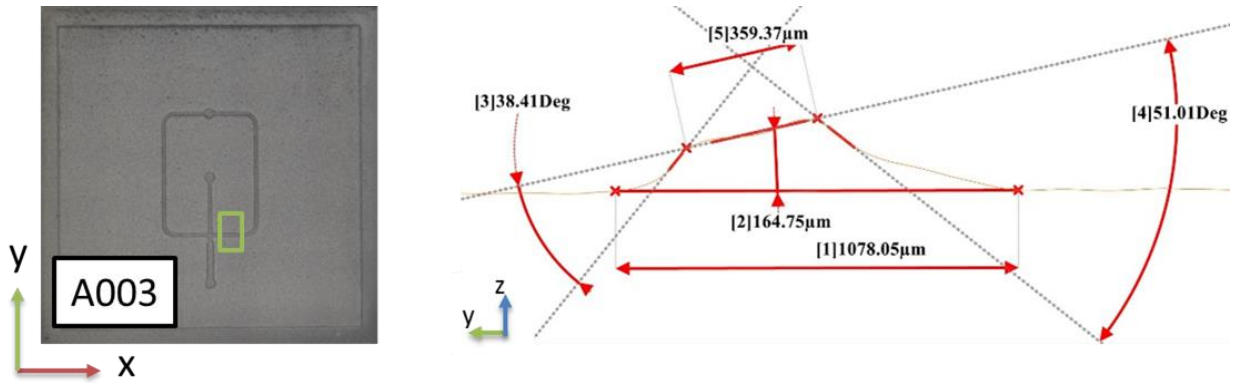


Figure 100. A003 right, parallel to gantry movement profile

#### 5.7.4: A004 Profiles

The perpendicular to gantry movement profile measurements for A004 are shown in Figure 101.

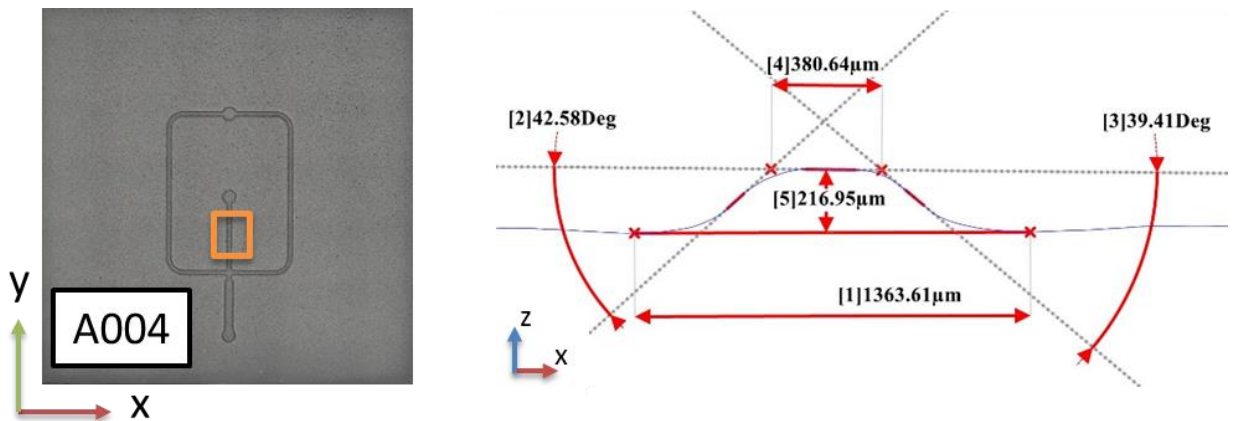


Figure 101. A004 perpendicular to gantry movement profile

The left, parallel to gantry movement profile measurements for A004 are shown in Figure 102.

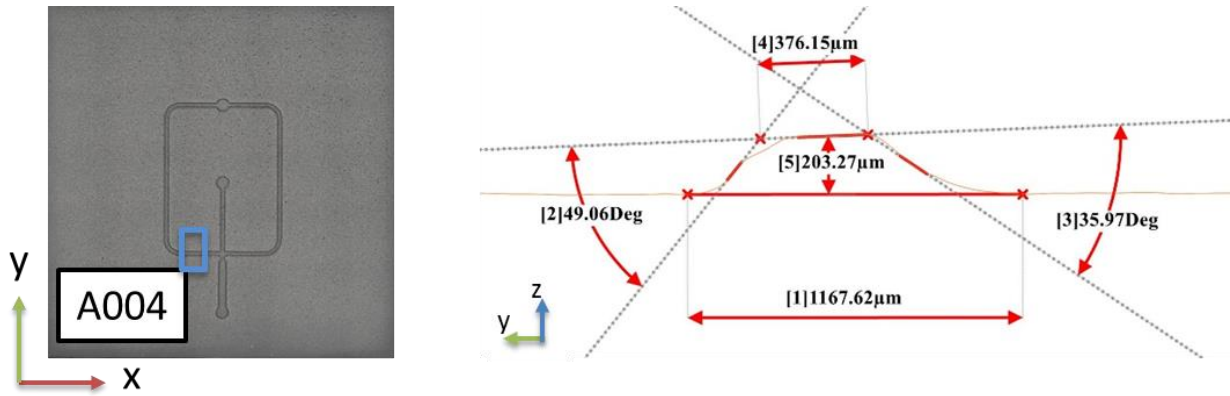


Figure 102. A004 left, parallel to gantry movement profile

The right, parallel to gantry movement profile measurements for A004 are shown in Figure 103.

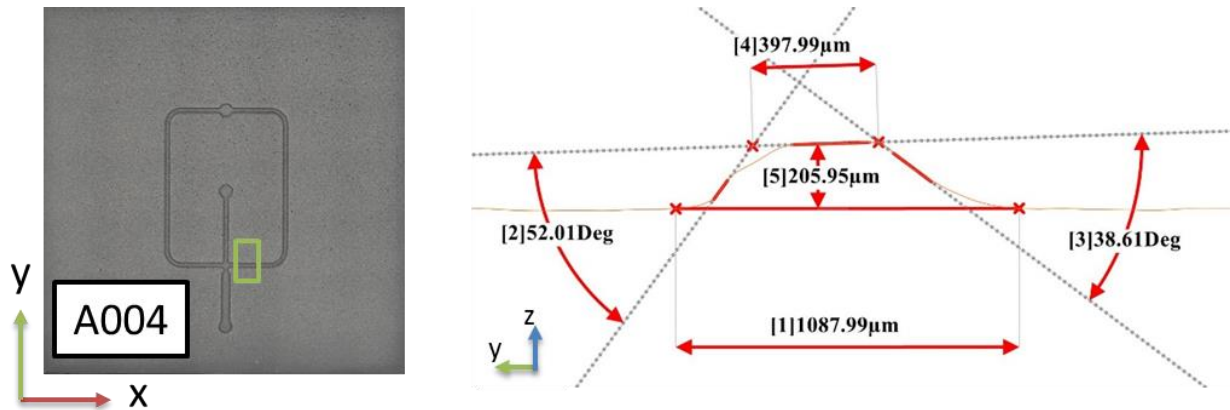


Figure 103. A004 right, parallel to gantry movement profile

### 5.7.5: Comparing Profiles

One comparison that can be made is between the parallel and perpendicular profiles in the sidewall angles. The average and standard deviation between the two angles on either side of the profile are reported and compared in Table 7. In addition to the Study A profiles, treatment 1 from the laBMD study described in Chapter 4 is included for comparison as well. The parameters used to produce the Study A microfluidics devices match the parameters used in treatment 1, so comparing them is a good

way to investigate whether the angles for a large area ablation (>50% surface area ablated), such as those seen in the microfluidics application, are similar to small area ablation (<50% surface area ablated), such as those in the laBMD study.

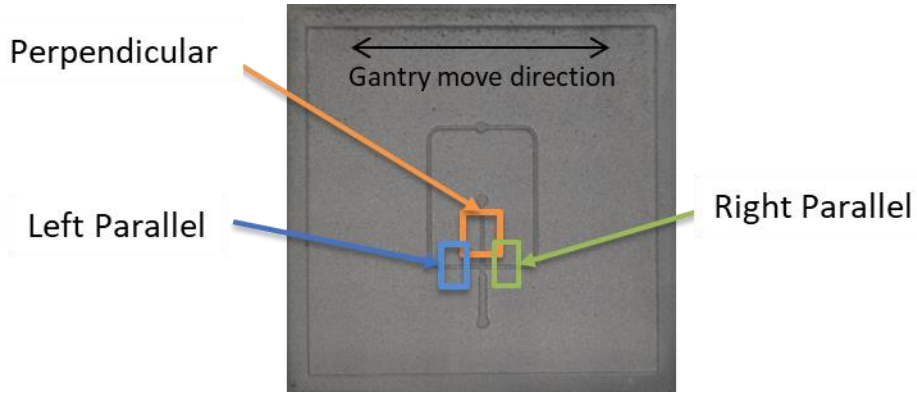


Figure 104. Location of measurement for profiles in Table 7

Table 7. Profile angles for A001, A003, and A004 and treatment 1

	Perpendicular Profile		Left Parallel Profile		Right Parallel Profile	
	$\theta_{avg}$	StDev $\theta$	$\theta_{avg}$	StDev $\theta$	$\theta_{avg}$	StDev $\theta$
A001	12.085	0.065	20.84	7.27	22.48	7.24
A003	41.285	0.965	47.19	4.57	44.71	6.3
A004	40.995	1.585	42.515	6.545	45.31	6.7
Treatment 1	53.6	0.4				

The standard deviation between the angles is greater for the parallel profiles than it is for the perpendicular profiles. The average standard deviation for the perpendicular profiles was 0.87°, whereas the average standard deviation for the left and right parallel profiles were 6.13° and 6.75°

The resulting angles show that the angles from study A were less than the expected angles from the laBMD experiment.

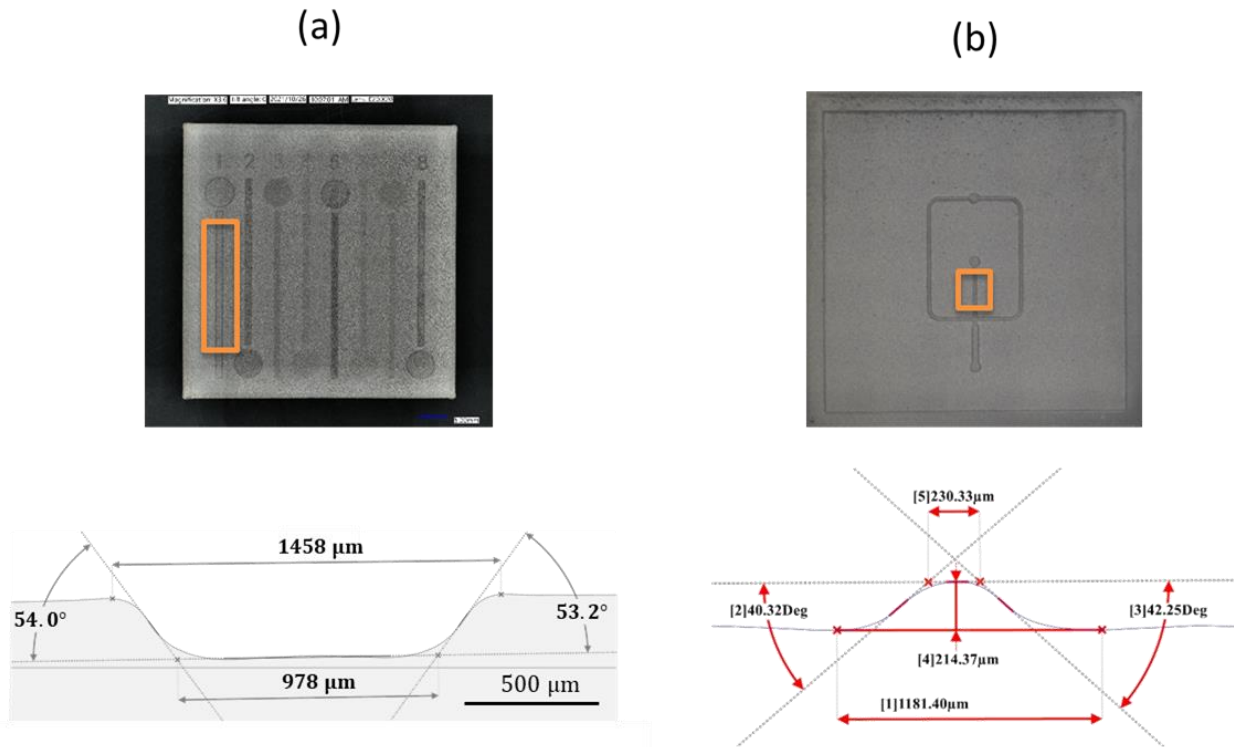


Figure 105. Comparison of (a) profile from treatment 1 channel to (b) profile from A003

## 5.8: Discussion and Conclusions

### 5.8.1: Pattern Features

The margin that originated from part A003 turned out to be beneficial to the laBMD process for the microfluidics application. In surface grinding, the extra margin provided a greater surface area for the part to sit on the work surface. Additionally, a greater margin reduces the amount of surface area that requires ablation which decreases the time of the ablation step. This reduces the thermal effects of the laser ablation on the bulk of the part since the part is subject to less material ablation.

### 5.8.2: Surface Grinding Considerations

Because the fixturing method is magnetic, the part either needs to be ferritic or attached to a ferritic base through clamping or adhesive to use the surface grinder. It was determined through consulting machining experts that the magnetic force on the BMD 17-4PH stainless steel was sufficient to hold the



workpiece down at the beginning of the surface grinding process. However, as the part approached the target thickness, two phenomena occurred that increased the difficulty of the surface grinding process. First, as mass of the metal in the part was reduced from grinding, the magnetic force on the part decreased since magnetic force is a function of the thickness, and subsequently mass, of the magnetic metal [85]. Second, material removal resulted in residual stresses deforming the mold, causing the mold's mid-section to raise up towards the grinding wheel. The first difficulty was responsible for multiple instances of the part dislodging from its position on the magnetic table, requiring repositioning on the magnetic plate via operator intervention. The second difficulty caused a nonuniform thickness of the final part.

## CHAPTER 6: SUMMARY AND CONCLUSIONS

In this work, there were two major undertakings: characterization of warpage in BMD and characterization of laser ablation. These studies provide pieces to use in predictive models.

### 6.1: Warpage Summary and Conclusions

Warpage was characterized for 17-4PH stainless steel material produced via BMD. This characterization was utilized a 12-factor, 2-level resolution IV fractional factorial DOE with center points, resulting in a total of 36 treatments. The factors include (1) height [2.25-mm, 4.50-mm], (2) width [20-mm, 30-mm], (3) length [100-mm, 150-mm], (4) print bed orientation [X, Y], (5) top and bottom layer count [4 layers, 8 layers], (6) infill line distance [1.8-mm, 3.8-mm], (7) raft top layers [9 layers, 27 layers], (8) interface layers [1 layer, 3 layers], (9) interface density [66.67%, 100%], (10) cooling fan speed [0%, 80%], (11) furnace position [left side, right side], and (12) parts hold time [1 hour, 12 hours]. Responses considered were the warpage at four processing points: one prior to separating the green-state part from the build sheet, one after separating the green-state part from the build sheet, one after solvent debinding, and one after sintering.

For the factors and levels considered, in the green state, prior to removing the part from the print sheet, height, print bed orientation, infill line distance, and cooling fan speed were the only single factor terms that influenced warpage. After peeling the part from the print sheet, print bed orientation, infill line distance, top and bottom layer count, and cooling fan speed were the only single factor terms that influenced warpage. After solvent debinding, length, print bed orientation, raft top layers, interface density and cooling fan speed influenced warpage. For sintered warpage, height and length were the only statistically significant factors

The warpage in the as-sintered state was dominant over the other 3 process points where warpage was measured. As parts progressed through the BMD process, the warpage magnitude tended to increase

along with the standard deviation of the warpage for the entire dataset. The average warpage before print sheet removal was 0.358 mm with 0.151 mm standard deviation. Similarly, the average warpage after print sheet removal was 0.248 mm with 0.150 mm standard deviation. After solvent debinding, the average warpage was 0.648 mm with standard deviation of 0.315, an as-sintered, the average warpage was 0.898 mm with a standard deviation of 0.528 mm.

The warpage of the as-sintered parts decreased with decreasing part length and increasing part height, and all other factors were insignificant in predicting the sintered warpage.

Next steps to continue the warpage part of this research may include validating the results of the experiment further with additional specimens generated from within the factor levels chosen for the study. Comparing the results to thermomechanical models and sintering simulation software such as live-sinter could be useful in validation efforts. A natural extension of a bounded factorial DOE would be to attempt to extrapolate from the data and exceed the factor ranges tested to see if assumptions still hold, providing more range to the predictive capabilities of models.

## **6.2: Laser Ablated BMD Summary and Conclusions**

This work demonstrates a novel laser ablated Bound Metal Deposition (laBMD) manufacturing process to create fine-scale features on additively manufactured parts. The demonstrated process utilizes a 60-watt CO<sub>2</sub> Epilog Helix laser to ablate green state 17-4 PH parts processed via a bound metal deposition (BMD). The laBMD process was characterized via a full-factorial design of experiments utilizing 5 factors each having 2 levels: (1) number of laser passes [1 pass, 3 passes], (2) laser power [25%, 75%], (3) laser speed [50%, 100%], (4) direction of laser travel [perpendicular, parallel], and (5) laser resolution [600 dpi, 1200 dpi]. The 5-factor 2-level DOE resulted in a total of 32 treatments and considered 4 responses: ablated depth, ablated surface roughness, angle between ablated and non-ablated regions, and ablated width.

For the factors and levels considered, the as-sintered ablation depths / pass ranged from 3 and 122  $\mu\text{m}$ , the ablated surface roughness ranged from 3 to 79  $\mu\text{m}$ , the angle between ablated and non-ablated regions ranged from  $1^\circ$  to  $68^\circ$ , and ablated widths ranged from 729 to 1254  $\mu\text{m}$ . Each of the four responses of interest were regressed using an incomplete 2<sup>nd</sup>-order model and backward elimination to determine statistically significant terms. Results indicate that the five factors predict between 75 and 94% of the observed variation in the response for the factors and levels considered. Lastly, an examination of the  $D-S_q-\theta$  response space allows for combinations of responses of interest to be identified and identifies a non-linear  $D-S_q$  relationship.

Compared to the BMD process, the laBMD process has at least six demonstrated or anticipated advantages: (1) finer control of depth, (2) finer control of curvilinear in-plane features, (3) positive draft angles, (4) approximately  $\frac{1}{4}$  of the manufacturing time of BMD's finest-resolution printing while being able to produce finer features, (5) narrower widths for embossed features, and (6) an ability to tailor ablation processing parameters to have even more control on responses of interest.

As with many new manufacturing methods, a more thorough understanding of laBMD is required to fully realize its capabilities. Potential future efforts include exploring a broader range of laBMD process-structure-property relationships, demonstrating laBMD for mold-manufacturing applications, and understanding, modeling relevant mechanisms for the ablation of inhomogeneous materials, and comparing post-laser treatment measurements before and after sintering.

This work is significant in that it demonstrates and motivates the use of hybrid manufacturing processes that will greatly expand the capabilities of additive manufacturing. One potential application is the manufacture of fine-scale molding surfaces such as those utilized in microfluidic molds.

## BIBLIOGRAPHY

- [1] “Metal Additive Manufacturing Market size to Increase by USD 7.19 Bn | Featuring Top Vendors Including 3D Systems Corp., EOS GmbH Electro Optical Systems, and General Electric Co. | Technavio.” <https://www.yahoo.com/now/metal-additive-manufacturing-market-size-103000794.html> (accessed Mar. 25, 2022).
- [2] A. Vafadar, F. Guzzomi, A. Rassau, and K. Hayward, “Advances in Metal Additive Manufacturing: A Review of Common Processes, Industrial Applications, and Current Challenges,” *Appl. Sci.*, vol. 11, p. 1213, Jan. 2021, doi: 10.3390/app11031213.
- [3] “3D-printing market report shows dramatic growth in metals and huge pricing disparities,” *plasticstoday.com*, Mar. 09, 2017. <https://www.plasticstoday.com/3d-printing/3d-printing-market-report-shows-dramatic-growth-metals-and-huge-pricing-disparities> (accessed Apr. 17, 2022).
- [4] “Mind Meld: How GE And A 3D-Printing Visionary Joined Forces | GE News.” <https://www.ge.com/news/reports/mind-meld-ge-3d-printing-visionary-joined-forces> (accessed Apr. 17, 2022).
- [5] “Additive Manufacturing Technology explained in 18 processes,” AMPOWER Report on Additive Manufacturing. <https://additive-manufacturing-report.com/additive-manufacturing-metal-technology/> (accessed Apr. 06, 2022).
- [6] “New and Upcoming Metal AM Technologies,” AMPOWER, Feb. 28, 2020. <https://ampower.eu/insights/new-metal-technologies/> (accessed Apr. 29, 2022).
- [7] S. Singh, G. Singh, C. Prakash, and S. Ramakrishna, “Current status and future directions of fused filament fabrication,” *J. Manuf. Process.*, vol. 55, pp. 288–306, Jul. 2020, doi: 10.1016/j.jmapro.2020.04.049.
- [8] D. Metal, “Deep Dive: Bound Metal Deposition (BMD),” *Desktop Metal*. <https://www.desktopmetal.com/resources/deep-dive-bmd> (accessed Apr. 25, 2022).
- [9] “3D Printing of Metal with Bound Metal Deposition Technology.” <https://www.metal3d.gr/en/metal3d> (accessed Apr. 25, 2022).
- [10] K. Rane and M. Strano, “A comprehensive review of extrusion-based additive manufacturing processes for rapid production of metallic and ceramic parts,” *Adv. Manuf.*, vol. 7, no. 2, pp. 155–173, Jun. 2019, doi: 10.1007/s40436-019-00253-6.
- [11] Desktop Metal, Fabricate. [Online]. Available: <https://fab.desktopmetal.com>
- [12] H. D. Morgan, H. U. Levatti, J. Sienz, A. J. Gil, and D. C. Bould, “GE jet engine bracket challenge: A case study in sustainable design,” *KES Trans. Sustain. Des. Manuf.*, vol. 1, no. 1, Art. no. 1, 2014.
- [13] “GE jet engine bracket challenge | Engineering & Design Challenges | GrabCAD.” <https://grabcad.com/challenges/ge-jet-engine-bracket-challenge> (accessed Apr. 25, 2022).
- [14] W. T. Carter et al., “The GE Aircraft Engine Bracket Challenge: An Experiment in Crowdsourcing for Mechanical Design Concepts,” 2014. Accessed: Apr. 25, 2022. [Online]. Available: <https://repositories.lib.utexas.edu/handle/2152/89299>

- [15] ASTM, "Standard terminology for additive manufacturing technology," ASTM, West Conshohocken, PA, F2792-12a, Aug. 2019.
- [16] J. Walter, A. Baumgärtel, M. Hustedt, R. Hebisch, and S. Kaierle, "Inhalation exposure to hazardous substances during powder-bed processes," *Procedia CIRP*, vol. 74, pp. 295–299, Jan. 2018, doi: 10.1016/j.procir.2018.08.114.
- [17] M. N. Azzougagh, F.-X. Keller, E. Cabrol, M. Cici, and J. Pourchez, "Occupational exposure during metal additive manufacturing: A case study of laser powder bed fusion of aluminum alloy," *J. Occup. Environ. Hyg.*, vol. 18, no. 6, pp. 223–236, Jun. 2021, doi: 10.1080/15459624.2021.1909055.
- [18] S. Dugheri et al., "A Qualitative and Quantitative Occupational Exposure Risk Assessment to Hazardous Substances during Powder-Bed Fusion Processes in Metal-Additive Manufacturing," *Safety*, vol. 8, no. 2, Art. no. 2, Jun. 2022, doi: 10.3390/safety8020032.
- [19] M. Nozar, V. Pokorna, and I. Zetkova, "Potential Health Hazards of Additive Manufacturing," in *DAAAM Proceedings*, 1st ed., vol. 1, B. Katalinic, Ed. DAAAM International Vienna, 2019, pp. 0654–0662. doi: 10.2507/30th.daaam.proceedings.090.
- [20] T. Kraft and H. Riedel, "Numerical simulation of die compaction and sintering," *Powder Metall.*, vol. 45, no. 3, Art. no. 3, Oct. 2002, doi: 10.1179/003258902225006989.
- [21] O. Coube and H. Riedel, "Numerical simulation of metal powder die compaction with special consideration of cracking," *Powder Metall.*, vol. 43, no. 2, pp. 123–131, Feb. 2000, doi: 10.1179/003258900665871.
- [22] W. Fang, X.-B. He, R.-J. Zhang, S. Yang, and X. Qu, "Evolution of stresses in metal injection molding parts during sintering," *Trans. Nonferrous Met. Soc. China*, vol. 25, Feb. 2015, doi: 10.1016/S1003-6326(15)63637-8.
- [23] A. Watson, J. Belding, and B. D. Ellis, "Characterization of 17-4 PH Processed via Bound Metal Deposition (BMD)," in *TMS 2020 149th Annual Meeting & Exhibition Supplemental Proceedings*, Cham, 2020, pp. 205–216. doi: 10.1007/978-3-030-36296-6\_19.
- [24] "Rods vs. Filament: Key advantages of bound metal rods – Knowledge Base | Desktop Metal." <https://knowledge.desktopmetal.com/hc/en-us/articles/360012062493-Rods-vs-Filament-Key-advantages-of-bound-metal-rods> (accessed Apr. 08, 2022).
- [25] "Studio System™ v.1 material process: print, debind, and sinter," Knowledge Base | Desktop Metal. <https://knowledge.desktopmetal.com/hc/en-us/articles/360005418833-Studio-System-v-1-material-process-print-debind-and-sinter> (accessed Apr. 08, 2022).
- [26] "English (North America) - Safety data sheets and site prep guide," Knowledge Base | Desktop Metal. <https://knowledge.desktopmetal.com/hc/en-us/articles/360024786694-English-North-America-Safety-data-sheets-and-site-prep-guide> (accessed Apr. 07, 2022).
- [27] "How do I dispose of waste in the debinder waste canister?," Knowledge Base | Desktop Metal. <https://knowledge.desktopmetal.com/hc/en-us/articles/360005362234-How-do-I-dispose-of-waste-in-the-debinder-waste-canister-> (accessed Apr. 07, 2022).
- [28] "To what temperature is the processing tank and/or the fluid heated to during the debind cycle?," Knowledge Base | Desktop Metal. <https://knowledge.desktopmetal.com/hc/en->

us/articles/360006009373-To-what-temperature-is-the-processing-tank-and-or-the-fluid-heated-to-during-the-debind-cycle- (accessed Apr. 07, 2022).

[29] “How many parts can I fit into the debinder?,” Knowledge Base | Desktop Metal. <https://knowledge.desktopmetal.com/hc/en-us/articles/360011732053-How-many-parts-can-I-fit-into-the-debinder-> (accessed Apr. 08, 2022).

[30] “Strategies for reducing debind time – Knowledge Base | Desktop Metal.” <https://knowledge.desktopmetal.com/hc/en-us/articles/360018824474-Strategies-for-reducing-debind-time> (accessed Apr. 07, 2022).

[31] “Setter plates for Ceramic and Metal Injection Moulding sintering,” Powder Injection Moulding International, Feb. 26, 2018. <https://www.pim-international.com/setter-plates-cim-mim-sintering/> (accessed Apr. 28, 2022).

[32] “Gas Specifications for Desktop Metal® Furnace,” Knowledge Base | Desktop Metal. <https://knowledge.desktopmetal.com/hc/en-us/articles/360011618613-Gas-Specifications-for-Desktop-Metal-Furnace> (accessed Apr. 28, 2022).

[33] “What is the role of gas in the furnace?,” Knowledge Base | Desktop Metal. <https://knowledge.desktopmetal.com/hc/en-us/articles/360013417154-What-is-the-role-of-gas-in-the-furnace-> (accessed Apr. 28, 2022).

[34] “What is Surface Energy? Calculation Models and More Explained,” Ossila. <https://www.ossila.com/pages/a-guide-to-surface-energy> (accessed Apr. 04, 2022).

[35] B. Bhushan, Ed., Springer Handbook of Nanotechnology. Berlin, Heidelberg: Springer Berlin Heidelberg, 2017. doi: 10.1007/978-3-662-54357-3.

[36] R. German, Powder Metallurgy & Particulate Materials Processing. Metal Powder Industry, 2005.

[37] D. Metal, “Thermal Debinding and Sintering 101,” Desktop Metal. <https://www.desktopmetal.com/resources/sintering-101> (accessed Apr. 26, 2022).

[38] “Desktop Metal reveals how its 3D printers rapidly churn out metal objects,” TechCrunch. <https://social.techcrunch.com/2017/04/25/desktop-metal-reveals-how-its-3d-printers-rapidly-churn-out-metal-objects/> (accessed Apr. 09, 2022).

[39] D. Metal, “Studio System™,” Desktop Metal. <https://www.desktopmetal.com/products/studio> (accessed Apr. 09, 2022).

[40] “Troubleshoot Warping,” Knowledge Base | Desktop Metal. <https://knowledge.desktopmetal.com/hc/en-us/articles/360022376893-Troubleshoot-Warping> (accessed Apr. 16, 2022).

[41] “Troubleshoot Blistering,” Knowledge Base | Desktop Metal. <https://knowledge.desktopmetal.com/hc/en-us/articles/360050332973-Troubleshoot-Blistering> (accessed Apr. 16, 2022).

[42] “Slumping [part defects],” Knowledge Base | Desktop Metal. <https://knowledge.desktopmetal.com/hc/en-us/articles/360005476813-Slumping-part-defects-> (accessed Apr. 16, 2022).

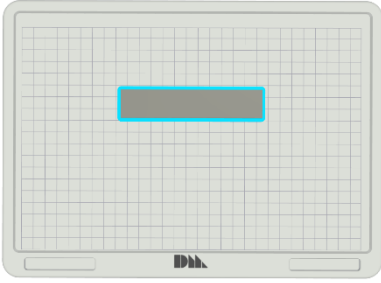
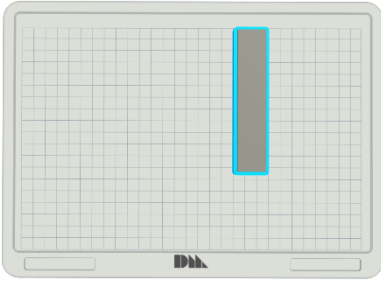
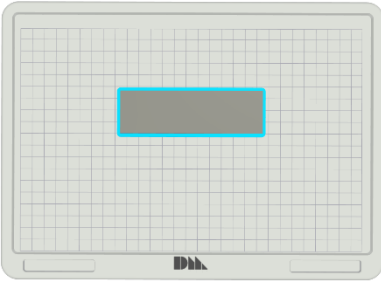
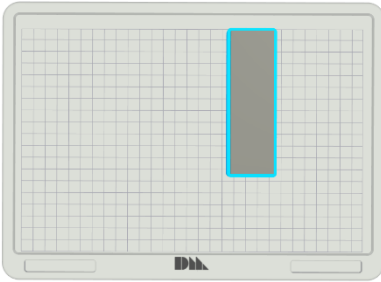
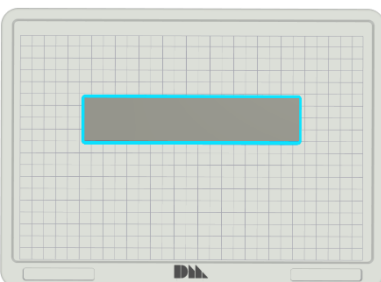
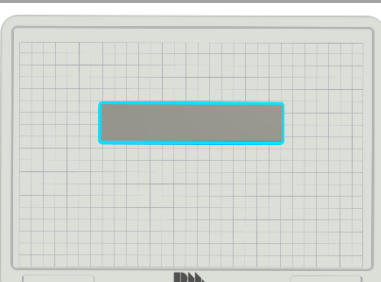
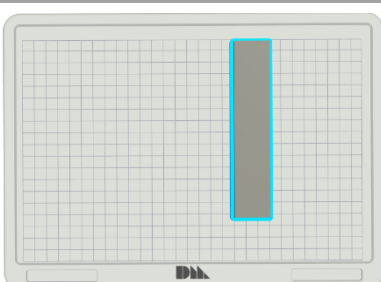
- [43] “Design guide – Knowledge base | Desktop Metal,” Sep. 09, 2019. <https://knowledge.desktopmetal.com/hc/en-us/categories/360001012354-Design-guide> (accessed Sep. 08, 2019).
- [44] M. Gabilondo, X. Cearsolo, M. Arrue, and F. Castro, “Influence of Build Orientation, Chamber Temperature and Infill Pattern on Mechanical Properties of 316L Parts Manufactured by Bound Metal Deposition,” *Materials*, vol. 15, no. 3, p. 1183, Feb. 2022, doi: 10.3390/ma15031183.
- [45] E28 Committee, “Test Methods for Tension Testing of Metallic Materials,” ASTM International. doi: 10.1520/E0008\_E0008M-16.
- [46] D. Metal, “Live Sinter,” Desktop Metal. <https://www.desktopmetal.com/resources/live-sinter> (accessed Apr. 10, 2022).
- [47] M. Semenova, “AMC Bridge | AMC Bridge Implements First-of-Its-Kind Sinter-Based Simulation Technology: Desktop Metal’s Live Sinter Case Study.” <https://www.amcbridge.com/case-studies/amc-bridge-implements-first-of-its-kind-sinter-based-simulation-technology-desktop-metal-s-live-sinter-case-study> (accessed Apr. 10, 2022).
- [48] “PIM International September 2020,” issue, pp. 67–74.
- [49] “BMD Process Limitations,” Knowledge Base | Desktop Metal. <https://knowledge.desktopmetal.com/hc/en-us/articles/360019351974-BMD-Process-Limitations> (accessed Apr. 29, 2022).
- [50] Y. Zhang et al., “Additive Manufacturing of Metallic Materials: A Review,” *J. Mater. Eng. Perform.*, vol. 27, no. 1, pp. 1–13, Jan. 2018, doi: 10.1007/s11665-017-2747-y.
- [51] D. Montgomery, *Design and analysis of experiments*, Third. John Wiley & Sons, 1991.
- [52] Minitab, *Minitab 19*. State College, PA: Minitab, 2020. [Online]. Available: <https://www.minitab.com/>
- [53] “PolyWorks Version Compatibility With the Edge ScanArm HD or Laser Line Probe HD,” FARO® Knowledge Base, Dec. 20, 2016. [https://knowledge.faro.com/Hardware/FaroArm\\_and\\_ScanArm/FaroArm\\_and\\_ScanArm/PolyWorks\\_Version\\_Compatibility\\_With\\_the\\_Edge\\_ScanArm\\_HD\\_or\\_Laser\\_Line\\_Probe\\_HD](https://knowledge.faro.com/Hardware/FaroArm_and_ScanArm/FaroArm_and_ScanArm/PolyWorks_Version_Compatibility_With_the_Edge_ScanArm_HD_or_Laser_Line_Probe_HD) (accessed Apr. 21, 2022).
- [54] T. J. Coogan and D. O. Kazmer, “Healing simulation for bond strength prediction of FDM,” *Rapid Prototyp. J.*, vol. 23, no. 3, pp. 551–561, Jan. 2017, doi: 10.1108/RPJ-03-2016-0051.
- [55] “What is the difference between coded units and uncoded units?” <https://support.minitab.com/en-us/minitab/18/help-and-how-to/modeling-statistics/doe/supporting-topics/basics/coded-units-and-uncoded-units/> (accessed Apr. 28, 2022).
- [56] “What are hierarchical models?” <https://support.minitab.com/en-us/minitab/19/help-and-how-to/statistical-modeling/anova/supporting-topics/anova-models/what-are-hierarchical-models/> (accessed Apr. 28, 2022).
- [57] “Effects plots for Analyze Factorial Design.” <https://support.minitab.com/en-us/minitab/19/help-and-how-to/statistical-modeling/doe/how-to/factorial/analyze-factorial-design/interpret-the-results/all-statistics-and-graphs/effects-plots/> (accessed Apr. 07, 2022).



- [58] “Interpret the key results for Analyze Factorial Design.” <https://support.minitab.com/en-us/minitab/19/help-and-how-to/statistical-modeling/doe/how-to/factorial/analyze-factorial-design/interpret-the-results/key-results/?SID=128050> (accessed Apr. 22, 2022).
- [59] “T-Test Definition,” Investopedia. <https://www.investopedia.com/terms/t/t-test.asp> (accessed Apr. 25, 2022).
- [60] “Overview for Factorial Plots.” <https://support.minitab.com/en-us/minitab/19/help-and-how-to/statistical-modeling/using-fitted-models/how-to/factorial-plots/before-you-start/overview/> (accessed Apr. 07, 2022).
- [61] G. Höflinger, “Brief Introduction to Coating Technology for Electron Microscopy,” Aug. 2013, Accessed: Apr. 07, 2022. [Online]. Available: <https://www.leica-microsystems.com/science-lab/brief-introduction-to-coating-technology-for-electron-microscopy/>
- [62] Y.-S. Kwon, Y. Wu, P. Suri, and R. M. German, “Simulation of the sintering densification and shrinkage behavior of powder-injection-molded 17-4 PH stainless steel,” *Metall. Mater. Trans. A*, vol. 35, no. 1, pp. 257–263, Jan. 2004, doi: 10.1007/s11661-004-0126-4.
- [63] B09 Committee, “Test Methods for Density of Compacted or Sintered Powder Metallurgy (PM) Products Using Archimedes Principle,” ASTM International. doi: 10.1520/B0962-17.
- [64] S. Ravi-Kumar, B. Lies, H. Lyu, and H. Qin, “Laser Ablation of Polymers: A Review,” *Procedia Manuf.*, vol. 34, pp. 316–327, Jan. 2019, doi: 10.1016/j.promfg.2019.06.155.
- [65] N. Ahmed, S. Darwish, and A. M. Alahmari, “Laser Ablation and Laser-Hybrid Ablation Processes: A Review,” *Mater. Manuf. Process.*, vol. 31, no. 9, pp. 1121–1142, Jul. 2016, doi: 10.1080/10426914.2015.1048359.
- [66] J. Hoffman, “The effect of recoil pressure in the ablation of polycrystalline graphite by a nanosecond laser pulse,” *J. Phys. Appl. Phys.*, vol. 48, no. 23, Art. no. 23, May 2015, doi: 10.1088/0022-3727/48/23/235201.
- [67] D. Förster, V. Onuseit, R. Weber, and T. Graf, “Energy transfer mechanisms during laser pulsed processing of metals,” Jun. 2015.
- [68] G. Raciukaitis and M. Gedvilas, “Processing of polymers by UV picosecond lasers,” in *International Congress on Applications of Lasers & Electro-Optics*, Miami, Florida, USA, 2005, p. M403. doi: 10.2351/1.5060544.
- [69] H. D. Vora, S. Santhanakrishnan, S. P. Harimkar, S. K. S. Boetcher, and N. B. Dahotre, “One-dimensional multipulse laser machining of structural alumina: evolution of surface topography,” *Int. J. Adv. Manuf. Technol.*, vol. 68, no. 1–4, pp. 69–83, Sep. 2013, doi: 10.1007/s00170-012-4709-8.
- [70] G. Galasso, M. Kaltenbacher, A. Tomaselli, and D. Scarpa, “A unified model to determine the energy partitioning between target and plasma in nanosecond laser ablation of silicon,” *J. Appl. Phys.*, vol. 117, no. 12, Art. no. 12, Mar. 2015, doi: 10.1063/1.4915118.
- [71] G. B. J. Cadot, D. A. Axinte, and J. Billingham, “Continuous trench, pulsed laser ablation for micro-machining applications,” *Int. J. Mach. Tools Manuf.*, vol. 107, pp. 8–20, Aug. 2016, doi: 10.1016/j.ijmactools.2016.04.011.

- [72] A. Slocombe and L. Li, "Laser ablation machining of metal/polymer composite materials," *Appl. Surf. Sci.*, vol. 154–155, pp. 617–621, Feb. 2000, doi: 10.1016/S0169-4332(99)00391-8.
- [73] A. Slocombe, A. Taufik, and L. Li, "Diode laser ablation machining of 316L stainless steel powder/polymer composite material: Effect of powder geometry," *Appl. Surf. Sci.*, vol. 168, no. 1, Art. no. 1, Dec. 2000, doi: 10.1016/S0169-4332(00)00566-3.
- [74] Dassault Systemes, SolidWorks. 2020. [Online]. Available: <https://www.solidworks.com/>
- [75] Epilog Laser, "Owner's manual for Epilog Mini/Helix - Model 8000," 2009.
- [76] M. Y. Noordin, V. C. Venkatesh, S. Sharif, S. Elting, and A. Abdullah, "Application of response surface methodology in describing the performance of coated carbide tools when turning AISI 1045 steel," *J. Mater. Process. Technol.*, vol. 145, no. 1, Art. no. 1, Jan. 2004, doi: 10.1016/S0924-0136(03)00861-6.
- [77] Keyence, "VHX-7000 series digital microscope catalog," VHX7000-KA-C3-US, 2019. [Online]. Available: <https://www.keyence.com>
- [78] Keyence, "VHX-7000 User's Manual," Japan, 96M16057 GB, 2019.
- [79] A. L. Boutiette, C. Toothaker, B. Corless, C. Boukaftane, and C. Howell, "3D printing direct to industrial roll-to-roll casting for fast prototyping of scalable microfluidic systems," *PLOS ONE*, vol. 15, no. 12, p. e0244324, Dec. 2020, doi: 10.1371/journal.pone.0244324.
- [80] A. D. Zweig, "A thermo-mechanical model for laser ablation," *J. Appl. Phys.*, vol. 70, no. 3, pp. 1684–1691, Aug. 1991, doi: 10.1063/1.349537.
- [81] "surface grinding question," *BladeForums.com*. <https://www.bladeforums.com/threads/surface-grinding-question.846194/> (accessed Apr. 29, 2022).
- [82] "Surface Grinding Thin Parts." <https://www.practicalmachinist.com/vb/general/surface-grinding-thin-parts-373982/> (accessed Apr. 29, 2022).
- [83] FARO, "FARO 8-axis Edge FaroARM & ScanArm." Dec. 11, 2018. [Online]. Available: [https://knowledge.faro.com/Hardware/FaroArm\\_and\\_ScanArm/FaroArm\\_and\\_ScanArm/Technical\\_Specification\\_Sheet\\_for\\_the\\_Edge\\_FaroArm\\_and\\_ScanArm](https://knowledge.faro.com/Hardware/FaroArm_and_ScanArm/FaroArm_and_ScanArm/Technical_Specification_Sheet_for_the_Edge_FaroArm_and_ScanArm)
- [84] "Polyworks." [Online]. Available: <https://www.innovmetric.com/en>
- [85] "Steel Thickness Calculator." <https://www.kjmagnetics.com/blog.asp?p=steel-thickness-calculator> (accessed Apr. 27, 2022).

**APPENDIX A: PRINT FOOTPRINTS FOR WARPAGE DOE**

Length	Width	Width (mm)	Length (mm)	Warp Specimens	X-Orientation	Y-Orientation
Lo	Lo	20	100	1, 5		
Lo	Hi	30	100	3, 7		
Hi	Lo	20	150	2, 6		
Hi	Hi	30	150	4, 8		
Mid	Mid	25	125	9		

## APPENDIX B: FABRICATE AND STUDIO SYSTEM UPDATES

Studio Firmware 1.8.2.7 - 03/08/2019

Fabricate Cloud 1.11 - 05/02/2019

Fabricate Cloud 1.12 - 05/30/2019

Studio Furnace 1.9.7.9 - 05/31/2019

Fabricate Cloud 1.12.1 - 06/17/2019

Fabricate Cloud 1.13 - 06/19/2019

Fabricate Cloud 1.14 - 07/17/2019

Fabricate Cloud 1.15 - 08/14/2019

Studio Firmware 2.1.4 - 08/28/2019

Studio Firmware 2.4.13 - 10/28/2019

Fabricate Cloud 2.0 - 10/30/2019

Fabricate Cloud 2.1 - 11/12/2019

Studio Firmware 3.0.14 - 11/15/2019

Fabricate Cloud 2.2 - 12/04/2019

Fabricate Cloud 2.3 - 01/06/2020

Studio Firmware 3.2.14 - 02/18/2020

Fabricate Cloud 2.5 - 02/20/2020

Fabricate Cloud 2.6 - 03/10/2020

Fabricate Cloud 2.10 - 08/07/2020

Fabricate Cloud 2.11 - 10/20/2020

Studio Firmware 4.0.15 - 12/23/2020

Fabricate Cloud 2.12 - 01/13/2021

Fabricate Cloud 2.13 - 03/11/2021

Studio Firmware 4.1.13 - 04/02/2021

Studio Firmware 4.1.15 - 04/20/2021

Fabricate Cloud 2.14 - 04/08/2021

Studio Firmware 4.2.5 - 05/17/2021

Studio Firmware 4.2.5.2 - 06/25/2021

Fabricate Cloud 2.15 - 08/03/2021

Studio Firmware 4.2.8 - 09/02/2021

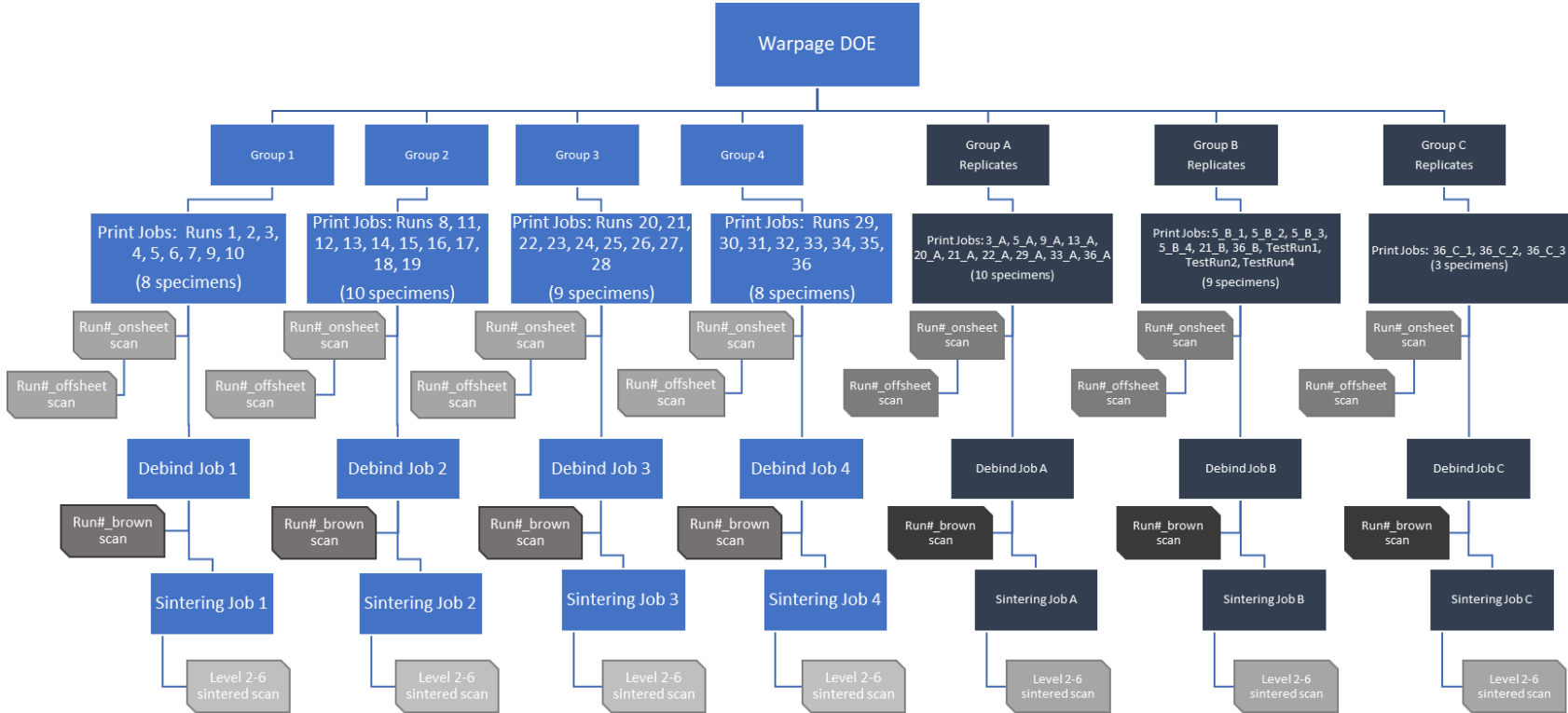
Fabricate Cloud 2.16 - 11/04/2021

Fabricate Cloud 2.17 - 12/14/2021

Studio Material File 4.4.11 - 1/21/2022

Fabricate Cloud 2.18 - 03/03/2022

**APPENDIX C: WARPAGE DOE GROUPING**



**APPENDIX D: WARPAGE DOE DATA**

Table 8. Warpage DOE Factors and Responses

ID#	Height	Width	Length	Print bed orientation	Top and bottom layer count	Infill line distance	Raft Top layers	Interface layers	Interface density	Cooling fan speed	Furnace position	Parts hold time (hours)	Print Time	On-sheet warpage	Off-sheet warpage (mm)	Brown warpage	Sintered Warpage	Cracked? (1 no, 0 yes)
	mm	mm	mm		Layers	mm				%		hours		mm	mm	mm	mm	
1	4.5	30	100	X	8	1.8	27	1	100	80	Right	1	6h53m	0.251	0.197	0.927	0.443	1
2	2.25	30	150	Y	4	3.8	9	1	100	0	Right	12	4h37m	0.631	0.392	0.353	1.426	1
3	3.375	25	125	X	6	2.8	18	2	83.335	40	Left	6.5	5h18	0.353	0.304	0.406	0.779	0
4	2.25	30	100	Y	4	1.8	27	1	100	80	Left	12	5h18m	0.168	0.118	0.503	0.928	1
5	4.5	20	100	X	4	3.8	27	3	100	0	Right	12	4h39m	0.385	0.327	1.272	0.424	0
6	3.375	25	125	Y	6	2.8	18	2	83.335	40	Right	6.5	5h15	0.230	0.130	0.600	0.570	1
7	4.5	20	100	Y	8	1.8	9	1	66.67	0	Right	12	4h13m	0.232	0.249	0.291	0.393	1
8	2.25	30	150	X	8	1.8	27	3	66.67	0	Right	12	7h28m	0.479	0.350	0.468	1.596	1
9	4.5	20	100	X	8	1.8	27	3	66.67	80	Left	1	5h20m	0.257	0.166	0.576	0.366	0
10	2.25	20	100	X	4	1.8	9	1	66.67	0	Left	1	3h7m	0.703	0.525	0.454	0.596	1
11	2.25	20	150	Y	8	1.8	9	3	100	80	Right	1	4h13m	0.296	0.140	0.969	1.324	1
12	4.5	30	150	Y	8	3.8	27	3	100	80	Right	12	8h42m	0.240	0.174	1.283	0.697	1
13	2.25	30	150	Y	8	1.8	9	1	66.67	80	Left	1	5h17m	0.220	-0.318	0.873	2.009	1
14	3.375	25	125	Y	6	2.8	18	2	83.335	40	Left	6.5	5h15m	0.296	0.185	0.514	0.776	1
15	2.25	30	100	Y	8	3.8	27	1	66.67	0	Right	1	5h20m	0.233	0.216	0.290	0.741	1
16	2.25	20	150	X	4	3.8	27	1	66.67	80	Right	1	5h8m	0.495	0.300	1.380	1.656	1
17	4.5	20	150	X	4	1.8	9	3	100	80	Left	12	5h39m	0.281	0.247	1.297	0.523	1
18	4.5	30	150	Y	4	1.8	27	3	66.67	0	Left	1	9h30m	0.251	0.221	0.592	0.295	1
19	4.5	30	150	X	8	3.8	9	1	100	0	Left	1	6h25m	0.412	0.399	0.481	0.597	1
20	3.375	25	125	X	6	2.8	18	2	83.335	40	Right	6.5	5h18m	0.350	0.274	0.677	0.881	0
21	4.5	20	100	Y	4	3.8	9	1	100	80	Left	1	3h31m	0.156	0.193	0.414	0.576	0

Table 8 Continued

22	2.25	20	100	Y	4	1.8	27	3	66.67	80	Right	12	4h11m	0.201	0.122	0.236	0.722	0
23	2.25	20	100	X	8	3.8	9	1	100	80	Right	12	3h13m	0.373	0.258	0.726	1.212	1
24	4.5	30	100	Y	8	1.8	9	3	100	0	Left	12	5h37m	0.297	0.216	0.530	0.282	1
25	2.25	20	150	Y	4	3.8	9	3	66.67	0	Left	12	3h44m	0.362	0.182	0.430	1.466	1
26	2.25	30	100	X	4	1.8	9	3	100	0	Right	1	4h2m	0.398	0.239	0.398	0.800	1
27	4.5	30	150	X	4	1.8	9	1	66.67	80	Right	12	7h16m	0.450	0.324	0.930	0.607	1
28	4.5	30	100	X	4	3.8	27	1	66.67	0	Left	12	5h47m	0.747	0.690	0.827	0.856	1
29	4.5	20	150	X	8	3.8	9	3	66.67	0	Right	1	5h2m	0.627	0.285	0.434	0.736	0
30	2.25	30	150	X	4	3.8	27	3	100	80	Left	1	6h54m	0.513	0.337	1.097	1.839	1
31	2.25	20	100	Y	8	3.8	27	3	100	0	Left	1	4h16m	0.423	0.332	0.612	0.898	1
32	2.25	30	100	X	8	3.8	9	3	66.67	80	Left	12	4h1m	0.357	0.268	0.377	0.973	1
33	2.25	20	150	X	8	1.8	27	1	100	0	Left	12	5h38m	0.486	0.303	0.742	2.579	1
34	4.5	20	150	Y	8	3.8	27	1	66.67	80	Left	12	6h25m	0.216	0.174	0.567	0.790	1
35	4.5	30	100	Y	4	3.8	9	3	66.67	80	Right	1	4h29m	0.155	0.138	0.488	0.567	1
36	4.5	20	150	Y	4	1.8	27	1	100	0	Right	1	6h56m	0.376	0.283	0.310	0.418	1

**APPENDIX E: WARPAGE DOE ANOVA TABLES**

Table 9. ANOVA table for On-sheet Warpage

Analysis of Variance: On-sheet Warpage

Source	DF	Adj SS	Adj MS	F-Value	P-Value
Model	14	0.76091	0.054351	26.58	0.000
Linear	7	0.54988	0.078554	38.41	0.000
Height (mm)	1	0.03156	0.031563	15.43	0.001
Length (mm)	1	0.03119	0.031188	15.25	0.001
Print Bed Orientation	1	0.23912	0.239121	116.93	0.000
Top and Bottom Layer Count	1	0.02382	0.023817	11.65	0.003
Infill Line Distance	1	0.02995	0.029951	14.65	0.001
Interface Layers	1	0.01229	0.012285	6.01	0.023
Cooling Fan Speed (%)	1	0.18196	0.181955	88.98	0.000
2-Way Interactions	5	0.14525	0.029050	14.21	0.000
Height (mm)*Width (mm)	1	0.01174	0.011743	5.74	0.026
Height (mm)*Interface Density	1	0.01877	0.018770	9.18	0.006
Height (mm)*Parts Hold Time (hours)	1	0.01077	0.010768	5.27	0.032
Width (mm)*Infill Line Distance	1	0.01012	0.010118	4.95	0.037
Width (mm)*Parts Hold Time (hours)	1	0.09385	0.093853	45.89	0.000
3-Way Interactions	1	0.05404	0.054038	26.42	0.000
Height (mm)*Width (mm)*Length (mm)	1	0.05404	0.054038	26.42	0.000
Curvature	1	0.01174	0.011743	5.74	0.026
Error	21	0.04294	0.002045		
Total	35	0.80386			



Table 10. ANOVA Table for Off-sheet Warpage

Analysis of Variance: Off-sheet Warpage

Source	DF	Adj SS	Adj MS	F-Value	P-Value
Model	9	0.644479	0.071609	12.71	0.000
Linear	4	0.468799	0.117200	20.80	0.000
Print Bed Orientation	1	0.194481	0.194481	34.52	0.000
Top and Bottom Layer Count	1	0.047201	0.047201	8.38	0.008
Infill Line Distance	1	0.051440	0.051440	9.13	0.006
Cooling Fan Speed (%)	1	0.175676	0.175676	31.18	0.000
2-Way Interactions	4	0.172849	0.043212	7.67	0.000
Height (mm)*Width (mm)	1	0.030938	0.030938	5.49	0.027
Height (mm)*Interface Layers	1	0.025935	0.025935	4.60	0.041
Width (mm)*Infill Line Distance	1	0.048906	0.048906	8.68	0.007
Width (mm)*Parts Hold Time (hours)	1	0.067070	0.067070	11.90	0.002
Curvature	1	0.002831	0.002831	0.50	0.485
Error	26	0.146487	0.005634		
Total	35	0.790966			

Table 11. ANOVA for Brown Warpage

Analysis of Variance: Brown Warpage

Source	DF	Adj SS	Adj MS	F-Value	P-Value
Model	10	2.92315	0.29232	13.26	0.000
Linear	5	1.62493	0.32499	14.74	0.000
Length (mm)	1	0.33723	0.33723	15.30	0.001
Print Bed Orientation	1	0.36281	0.36281	16.46	0.000
Raft Top Layers	1	0.15638	0.15638	7.09	0.013
Interface Density	1	0.22798	0.22798	10.34	0.004

Table 11 Continued

Cooling Fan Speed (%)	1	0.54054	0.54054	24.52	0.000
2-Way Interactions	4	1.25444	0.31361	14.23	0.000
Height (mm)*Width (mm)	1	0.13611	0.13611	6.18	0.020
Height (mm)*Length (mm)	1	0.14405	0.14405	6.54	0.017
Height (mm)*Interface Layers	1	0.18896	0.18896	8.57	0.007
Height (mm)*Parts Hold Time (hours)	1	0.78532	0.78532	35.63	0.000
Curvature	1	0.04378	0.04378	1.99	0.171
Error	25	0.55102	0.02204		
Total	35	3.47418			

Table 12. ANOVA for Sintered Warpage

Analysis of Variance: Sintered Warpage

Source	DF	Adj SS	Adj MS	F-Value	P-Value
Model	4	7.86463	1.96616	32.48	0.000
Linear	2	6.53944	3.26972	54.02	0.000
Height (mm)	1	4.64744	4.64744	76.78	0.000
Length (mm)	1	1.89200	1.89200	31.26	0.000
2-Way Interactions	1	1.22814	1.22814	20.29	0.000
Height (mm)*Length (mm)	1	1.22814	1.22814	20.29	0.000
Curvature	1	0.09706	0.09706	1.60	0.215
Error	31	1.87649	0.06053		
Total	35	9.74112			

**APPENDIX F: FACTOR LEVELS & RESULTS DATA FOR LABMD STUDY**

Table 13. Factor levels and response quantities for laBMD study

T#	Passes	Power	Speed	Laser direction	Resolution	As-Sintered State						
						Avg Depth	Avg Depth / pass	StDev Depth	Roughness (S <sub>a</sub> )	Avg Angle	Angle Diff	Width bottom
	#	%	%		dpi	μm	μm	μm	μm	deg	deg	μm
1	3	75	50	Perp.	600	229	76	7	7.0	53.6	0.8	978
2	3	25	50	Perp.	1200	102	34	1	23.0	30.3	1.5	887
3	1	25	100	Perp.	1200	4	4	0	7.2	2.0	0.1	760
4	1	75	100	Perp.	600	31	31	2	11.8	11.5	1.8	855
5	1	75	50	Perp.	1200	88	88	4	13.5	28.6	0.3	1052
6	1	25	50	Perp.	600	17	17	0	8.6	7.0	0.9	877
7	3	25	100	Perp.	600	8	3	0	7.6	3.4	-0.1	729
8	3	75	100	Perp.	1200	115	38	6	12.2	33.3	2.5	997
9	1	25	100	Paral.	1200	15	15	3	3.7	9.3	2.8	1070
10	3	75	100	Paral.	1200	147	49	3	50.8	62.1	4.8	1085
11	3	25	50	Paral.	1200	85	28	7	24.7	55.1	7.0	1070
12	3	75	50	Paral.	600	183	61	2	17.6	65.5	-6.1	1059
13	1	25	50	Paral.	600	17	17	1	3.8	9.6	0.4	1078
14	1	75	50	Paral.	1200	122	122	2	15.9	47.6	10.7	1032
15	3	25	100	Paral.	600	9	3	1	6.3	9.6	-2.1	1097
16	1	75	100	Paral.	600	13	13	2	5.8	12.7	1.0	1031
17	3	75	50	Perp.	1200	81	27	5	73.6	50.7	6.0	1254
18	3	75	100	Perp.	600	114	38	0	15.5	34.8	1.9	926
19	3	25	100	Perp.	1200	12	4	1	10.7	6.4	-0.6	984
20	3	25	50	Perp.	600	56	19	4	16.5	17.1	2.5	795
21	1	25	50	Perp.	1200	36	36	1	6.0	9.4	2.6	798
22	1	25	100	Perp.	600	3	3	0	11.2	1.2	0.1	732
23	1	75	50	Perp.	600	67	67	2	6.0	19.9	2.1	941
24	1	75	100	Perp.	1200	63	63	2	6.2	17.7	0.6	831
25	1	75	100	Paral.	1200	64	64	4	8.1	27.1	8.6	1029
26	1	75	50	Paral.	600	56	56	1	12.5	24.8	5.2	1011
27	3	25	50	Paral.	600	52	17	1	7.4	38.4	1.3	1080
28	3	75	100	Paral.	600	81	27	2	15.7	47.3	13.1	1073
29	3	25	100	Paral.	1200	14	5	2	9.0	12.8	-0.1	1086
30	3	75	50	Paral.	1200	253	84	7	79.0	68.2	8.4	1077
31	1	25	100	Paral.	600	4	4	0	3.2	2.9	0.4	1107
32	1	25	50	Paral.	1200	22	22	1	9.9	16.4	0.8	1042

## APPENDIX G: WARPAGE EXPERIMENT INFORMATION

Table 14. Table of factors in warpage DOE

Factor	Name
A	Height (mm)
B	Width (mm)
C	Length (mm)
D	Print Bed Orientation
E	Top and Bottom Layer Count
F	Infill Line Distance
G	Raft Top Layers
H	Interface Layers
J	Interface Density
K	Cooling Fan Speed (%)
L	Furnace Position
M	Parts Hold Time (hours)

### Design Summary

Factors: 12 Base Design: 12, 32 Resolution: IV  
 Runs: 36 Replicates: 1 Fraction: 1/128  
 Blocks: 1 Center pts 4  
 (total):

Design Generators: F = ACE, G = ACD, H = ABD, J = ABE, K = CDE, L = ABCDE, M = ADE

### Alias Structure (up to order 3)

I

A + BDH + BEJ + BKL + CDG + CEF + CKM + DEM + DFK + EGK + FGM + FHL + GJL + HJM  
 B + ADH + AEJ + AKL + CFJ + CGH + CLM + DFL + DJM + EGL + EHM + FHK + GJK  
 C + ADG + AEF + AKM + BFJ + BGH + BLM + DEK + DFM + DJL + EGM + EHL + FGK + HJK  
 D + ABH + ACG + AEM + AFK + BFL + BJM + CEK + CFM + CJL + EFG + EHJ + GKM + HKL  
 E + ABJ + ACF + ADM + AGK + BGL + BHM + CDK + CGM + CHL + DFG + DHJ + FKM + JKL  
 F + ACE + ADK + AGM + AHL + BCJ + BDL + BHK + CDM + CGK + DEG + EKM + GHJ + JLM  
 G + ACD + AEK + AFM + AJL + BCH + BEL + BJK + CEM + CFK + DEF + DKM + FHJ + HLM  
 H + ABD + AFL + AJM + BCG + BEM + BFK + CEL + CJK + DEJ + DKL + FGJ + GLM  
 J + ABE + AGL + AHM + BCF + BDM + BGK + CDL + CHK + DEH + EKL + FGH + FLM  
 K + ABL + ACM + ADF + AEG + BFH + BGJ + CDE + CFG + CHJ + DGM + DHL + EFM + EKL  
 L + ABK + AFH + AGJ + BCM + BDF + BEG + CDJ + CEH + DHK + EJK + FJM + GHM

M + ACK + ADE + AFG + AHJ + BCL + BDJ + BEH + CDF + CEG + DGK + EFK + FJL + GHL  
AB + DH + EJ + KL  
AC + DG + EF + KM  
AD + BH + CG + EM + FK  
AE + BJ + CF + DM + GK  
AF + CE + DK + GM + HL  
AG + CD + EK + FM + JL  
AH + BD + FL + JM  
AJ + BE + GL + HM  
AK + BL + CM + DF + EG  
AL + BK + FH + GJ  
AM + CK + DE + FG + HJ  
BC + FJ + GH + LM  
BF + CJ + DL + HK  
BG + CH + EL + JK  
BM + CL + DJ + EH  
ABC + AFJ + AGH + ALM + BDG + BEF + BKM + CDH + CEJ + CKL + DEL + DJK + EHK + FGL + FHM + GJM +  
HJL  
ABF + ACJ + ADL + AHK + BCE + BDK + BGM + BHL + CGL + CHM + DFH + DGJ + EFJ + EGH + ELM + FKL +  
JKM  
ABG + ACH + AEL + AJK + BCD + BEK + BFM + BJL + CFL + CJM + DFJ + DGH + DLM + EFH + EGJ + GKL +  
HKM  
ABM + ACL + ADJ + AEH + BCK + BDE + BFG + BHJ + CFH + CGJ + DGL + DHM + EFL + EJM + FJK + GHK +  
KLM

## **BIOGRAPHY OF THE AUTHOR**

Alexander Watson was born in Trenton, New Jersey on April 19, 1998. He was raised in Brimfield, Massachusetts and graduated from Tantasqua High School in 2016. He attended The University of Maine and graduated in 2020 with a Bachelor's degree in Mechanical Engineering. He continued his studies at the University of Maine, entering the Mechanical Engineering graduate program in 2020. Alexander is a candidate for the Master of Science degree in Mechanical Engineering from the University of Maine in May 2022.